ABSTRACT

RADIO DIAGNOSTICS OF PARTICLES AND PLASMA IN THE SOLAR CORONA

by
Sherry Chhabra

Radio diagnostics, in addition to their capabilities in exploring intense, impulsive bursts, also provide a high sensitivity to much weaker events, which may not show any substantial signature in other wavelengths.

The initial case study examines a complex event consisting of multiple radio sources/bursts associated with a fast coronal mass ejection (CME) and an M 2.1 class solar flare (SOL2015-09-20). 'First-light' data from the Owens Valley Radio Observatory–Long Wavelength Array is put in context with observations from Large Angle and Spectrometric Coronagraph onboard the Solar and Heliospheric Observatory, along with the WAVES radio spectrograph onboard WIND, the Expanded Owens Valley Solar Array, and the Air Force Radio Solar Telescope Network. One burst source exhibiting an outward motion is focused upon indicating movement associated with the core of the CME and is classified as type IVm burst. The source height, smoothness of the emission in frequency and time, along with a lower density in the region, indicate the likelihood of gyrosynchrotron as the underlying mechanism over plasma emission. Spectral fitting techniques are used to estimate the physical conditions during the outward movement of the source.

The second study investigates whether energy bursts from small breaks in stressed magnetic fields (nanoflares) can accelerate particles like full-sized flares, and if so, how efficiently? Since nanoflares may produce numerous 'mildly energetic' particles, at those energies, the emission in X-ray will be dominated by the thermal component. Type III radio bursts generated by propagating energetic electrons are best suited for the purpose. A model is created to simulate type III emission that may

be produced by thousands of nanoflares occurring per second and the novel time–lag technique used to detect the motion of particles. The technique indeed detects the signature of type IIIs despite the numerous overlapping bursts and added noise that is expected in a radio instrument. Based on the findings of the model and associated testing, data from the Very Large Array, Low Frequency Array, and Long Wavelength Array are currently being looked at for signatures of such bursts in the corona. A similar test is performed on data from the FIELDS instrument onboard Parker Solar Probe to look for signatures of particle acceleration in the solar wind from small-scale reconnection events.

RADIO DIAGNOSTICS OF PARTICLES AND PLASMA IN THE SOLAR CORONA

by
Sherry Chhabra

A Dissertation
Submitted to the Faculty of
New Jersey Institute of Technology and
Rutgers, The State University of New Jersey – Newark
in Partial Fulfillment of the Requirements for the Degree of
Doctor of Philosophy in Applied Physics

Department of Physics

May 2021

APPROVAL PAGE

RADIO DIAGNOSTICS OF PARTICLES AND PLASMA IN THE SOLAR CORONA

Sherry Chhabra

Dr. Dale E. Gary, Dissertation Advisor — Date
Distinguished Professor of Physics, NJIT

Dr. James A. Klimchuk, Dissertation Co–Advisor — Date
Research Astrophysicist, NASA–Goddard Space Flight Center

Dr. Andrew J. Gerrard, Committee Member — Date
Professor of Physics, NJIT

Dr. Bin Chen, Committee Member — Date
Associate Professor of Physics, NJIT

Dr. Lindsay Glesener, Committee Member — Date
Assistant Professor of Physics, University of Minnesota

Dr. Zhen Wu, Committee Member — Date
Professor of Physics, Rutgers-Newark

BIOGRAPHICAL SKETCH

Author: Sherry Chhabra

Degree: Doctor of Philosophy

Date: May 2021

Undergraduate and Graduate Education:

- Doctor of Philosophy in Applied Physics,
  New Jersey Institute of Technology, Newark, NJ,
  and Rutgers University, Newark, NJ, 2021
- Master of Science in Physics,
  Fergusson College, University of Pune, Pune, India, 2014
- Bachelor of Science, Major: Physics, Minor: Mathematics and Statistics,
  Fergusson College, University of Pune, Pune, India, 2012

Major: Applied Physics

Publications:

S. Chhabra, J. A. Klimchuk, D. E. Gary. Signatures of Type III Radio Bursts in the Solar Wind from Small-scale Reconnection Events. *In preparation*, 2021.

S. Chhabra, J. A. Klimchuk, D. E. Gary. Signature of Type III Radio Bursts in Nanoflares: Modeling. *Submitted to The Astrophysical Journal*, 2021.

S. Chhabra, D. E. Gary, G. Hallinan, M. M. Anderson, B. Chen, L. J. Greenhill, D. C. Price. Imaging Spectroscopy of CME–Associated Solar Radio Bursts using OVRO–LWA. *The Astrophysical Journal*, 906(2):132, January 2021.

Selected Presentations:

S. Chhabra, “Do nanoflares accelerate particles in the same manner as full-sized flares?,” *Oral presentation (virtual)*, Internal Scientist Funding Model (ISFM) showcase, NASA Headquarters, 2021.

S. Chhabra, “Signatures of Type III Radio Bursts from Small–scale Reconnection Events,” *Invited Seminar (virtual)*, National Solar Observatory, Boulder, CO, 2021.

S. Chhabra, “Radio Diagnostics of Impulsive Events on the Sun,” *Invited Seminar (virtual)*, Udaipur Solar Observatory (USO) Seminar, PRL, India, 2020.

S. Chhabra, “Tuning in to the Solar Radio,” *Invited Talk (virtual)*, Science at Low Frequencies VII, 2020.

S. Chhabra, “Signatures of Type III Radio Bursts from Small–scale Reconnection Events,” *Invited Seminar (virtual)*, Naval Research Laboratory, Washington DC, 2020.

S. Chhabra, “Imaging–Spectroscopy of CME–Associated Radio Bursts using OVRO–LWA Final Results,” *Oral Presentation (virtual)*, MAS–APS Meeting, 2020.

S. Chhabra, “Study of Type III Radio Bursts in Nanoflares,” *Invited talk*, 19$^{\text{th}}$ Annual International Astrophysics Conference, Santa Fe, NM, 2020.

S. Chhabra, “Imaging–Spectroscopy of CME–Associated Radio Bursts using OVRO–LWA: Final Results,” *Oral Presentation*, AGU Fall Meeting, San Francisco, CA, 2019.

S. Chhabra “Study of Type III Radio Bursts in Nanoflares,” *Oral presentation*, LOOPS Meeting, St. Andrews, UK, 2019.

S. Chhabra “Study of Type III Radio Bursts in Nanoflares,” *Oral presentation*, AGU Fall Meeting, Washington DC, 2018.

S. Chhabra “Imaging–Spectroscopy of CME–Associated Radio Bursts using OVRO–LWA: Preliminary Results,” *Oral presentation*, Solar Physics Division Meeting, Portland, OR, 2017.

S. Chhabra “Imaging–Spectroscopy of CME–Associated Radio Bursts using OVRO–LWA: Preliminary Results,” *Oral presentation*, AGU Fall Meeting, San Francisco, CA, 2016.

S. Chhabra “Imaging–Spectroscopy of CME–Associated Radio Bursts using OVRO–LWA: Preliminary Results,” *Oral presentation*, Science at Low Frequencies III, Pasadena, CA, 2016.

To my sister, Prerna, who always knew exactly what I needed even when I did not.

To my brother, Jatin, who stood by me through it all.

To my parents, Prem Lata and Harvinder Kumar, two of the strongest people I know. The source of my resilience and spirit.

To all Womankind. We are each others' greatest support.

इतः पूर्वं मूलदृढीकरणम् । इतः परं निश्चितो विकास ऊर्दध्वम् ।।

It is here that I have taken root. From here on, I only move upward.

ACKNOWLEDGMENT

This long yet magnificent journey would not have been successful without the invaluable support of several wonderful people in my life. Words are not enough to express my gratitude to each one of you, yet I shall endeavor to do my best.

I have been most fortunate to have not one but two incredible advisors, Dr. Dale Gary and Dr. Jim Klimchuk. Dale, you have always made yourself available to look into my codes or my drafts irrespective of the time of the day or the day of the week. And with each conversation, you have helped me mature as a researcher. Thank you for grounding me and pushing me to challenge myself. For that and many other things, I am sincerely grateful. Jim, thank you for being my loudest cheerleader and always believing in me. Your door (and now the Teams caller) has always been open for serious research-oriented discussions and fun-filled banter. I promise to keep striving, and then maybe one day, I will be able to pronounce 'Lamborghini' correctly. On a more serious note, I could not have asked for better mentors to guide me through this time. I only hope to develop the same acumen as you someday. Above all, I really appreciate how patient you both have been with me. It has indeed been an honor and a privilege.

A special thanks to Dr. Andrew Gerrard, Dr. Bin Chen, Dr. Lindsay Glesener, and Dr. Zhen Wu for agreeing to serve on my dissertation committee. Your advice and encouragement have been invaluable.

I must acknowledge the support by the Department of Physics in the form of a teaching assistantship for the first two years of my Ph.D. The next three years of my research were supported in part by the NSF grants AST–1615807, AGS–1654382, and AST–19010354 and by NASA grants 80NSSC18K1128 and 80NSSC17K0660, the Internal Scientist Funding Model (competitive work package program) at Goddard Space Flight Center; and the FIELDS experiment on Parker Solar Probe. I am very grateful to the following organizations for their financial support: the Solar Heliospheric and Interplanetary Environment (SHINE) workshop steering committee for the travel support at SHINE 2018 and 2019 workshops; the LOOPS meeting steering committee for the financial support to attend the LOOPS 2019 meeting; and the Graduate Student Association of New Jersey Institute of Technology for the travel award to attend the American Geophysical Union Fall Meeting in 2019.

My aspiration to become an astrophysicist has been a long endeavor, and every step of the way was paved by exceptional teachers. I would especially like to mention Dr. Usha Srinivasan, who helped me break the barriers of my comfort zone; Dr. Raka Dabhade, who made sure I found my footing; and Dr. Durgesh Tripathi, who showed me my shortcomings and empowered me to defeat them. Thank you for instilling in me love for the subject and a strong foundation that has led me this far.

I want to express my sincere appreciation to the members of the Center for Solar-Terrestrial Research and the Solar Radio Group at NJIT, Shaheda Shaik, Yi Chai, Natsuha Kuroda, Yingjie Luo, Yuqian Wei, Meiqi Wang, and Drs. Bin Chen, Sijie Yu, Gregory Fleishman, Gelu Nita, Andrew Gerrard, and Hyomin Kim who were ever-so welcoming and always supportive. Thank you for creating a workplace teeming with stimulating discussions. Special thanks to Yingjie Luo and Drs. Bin Chen and Sijie Yu for spending their valuable time and helping me get acquainted with processing techniques for VLA data.

A shoutout to Cheryl James for always being on top of things and helping me out with the countless issues for which my panicked self always came running to you. And for all the magic you do behind the scenes to help us keep our science going, you are awesome. To Felicia Margolies, for always taking the time out of your busy schedule to answer my questions and making sure all the grant application procedures run smoothly. I want to express my admiration for Christine Oertel, Leslie Williams, Cindy Montalvo-Harden, and Donald James for all their hard work. Your prompt solutions to my questions and concerns made my Ph.D. life much easier.

My transition to Goddard could not have been possible without the endless support of Callie Booth, Kathleen Starling, Amy Shimonkevitz, and Helainy Pena. Thank you very much for everything that you do. Amy, thank you for your cheerful presence; I will miss you dearly. A special thanks to Jeff Bradford and Ricky Arias for all your help with my unending IT problems.

The unflinching love and support of my friends and family have been my biggest strength in bringing me this far. I count my blessings when I think of these people that I am lucky to have. I am indebted to my parents, Prem Lata and Harvinder Kumar, who showered me with love, supported me through all my decisions, and with each step they took in life, showed me what it means to persevere. To my sister Prerna, for everything that you do. You have made me what I am today. To my brother-in-law Ashish for all the banter and fights, for being my friend, and for always looking out for me. To my adorable nephews Shaan and Eva, who light up our lives each day and who have unfailingly made sure I wake up every morning and keep working. To my brother Jatin for being my pillar and for his spider-sense that always knew when I needed him. To my sister-in-law Soohyun, who treats me like her own child, for all the love and encouragement. To my partner, Siva Kumar, my family away from my family, for being the calm to my storm. To Satvik Sachdev for teaching me the power of will. To my partner in crime, Silpa Das and Parthibha Bhatta, who endured all our shenanigans. To Shanoo Garg, and Apoorv Narang for always being with me through thick and thin, I could not have done this without you. To Prateek Dhall for lending his editing prowess every time I demand it. To Annapurna Valluri, who helped me with the translations of my dedication with patience and kindness.

I am grateful for the friends that I made during my time at NJIT, Chris Bolton, the best office buddy; Mykola Shumovskyi, for all his questions and Yixuan Sun, for his camaraderie and fun-filled gatherings; Shaheda Shaik and Jayachandra Konduru, for all the yum food, the love, the counsel, for bringing Tara into our lives and for looking after us like our elder siblings; Riddhi Chavda and Harshita Gedela, without whom, the past one year would have been unbearable, you are the best. My transition to Goddard came at a price, and I would like to thank Ethan Walters and Derric Alexander for being fantastic people to live with in an otherwise desolate place such as Greenbelt. I was lucky to find company among amazing people like Emily Mason, Samuel Schonfeld, Aleida Higginson, Joel Dahlin, Kalman Knizhnik, Samantha Wallace, and Micah Weberg, in whose spirited presence many a lunch was spent playing exciting board games or in immersive discussions. You have been by my side, constantly inspiring and motiving me and rooting for my success. The little time we have had together only makes me wish I met you all sooner, and I look forward to many more years together.

Last but not least, I would like to thank Ms. Clarisa Gonzalez-Lenahan and Dr. Sotirios Ziavras for their meticulous review of this dissertation in streamlining the formatting. I would also like to thank David Tress at the Office of Graduate Studies for being a fountain of information and for helping me navigate all the paperwork with great ease.

TABLE OF CONTENTS

Chapter **Page**

Table of Contents
(Continued)

LIST OF TABLES

LIST OF FIGURES

Figure **Page**

List of Figures (Continued)

Figure **Page**

List of Figures
(Continued)

Figure **Page**

List of Figures
(Continued)

Figure **Page**

List of Figures
(Continued)

Figure **Page**

List of Figures
(Continued)

CHAPTER 1

INTRODUCTION

The nearest star to us, the Sun, along with making life possible on our planet, also serves as a great laboratory to explore some of the most fundamental processes observed in the universe. Solar emission is observed at all frequencies in the electromagnetic spectrum. Most of the harmful radiation from the Sun, i.e., ultraviolet (UV), extreme-ultraviolet (EUV), and x-rays, is absorbed by the Earth's atmosphere, while the visible, infrared (IR), and some radio waves make it to the surface. The measure of the energy output of the Sun as a function of wavelength is known as solar spectral irradiance. On a macro scale, the irradiance evolves with the 11-year solar magnetic cycle. Additionally, it also exhibits variation on a timescale of hours to days based on the magnetic activity on the Sun. Transient impulsive events such as a large solar flare or a coronal mass ejection (CME) can drive enormous amounts of energy into the interplanetary medium and toward Earth.

Spectral irradiance from EUV and x-rays plays a vital role in driving our space weather. In the current age, with the deep dependence of society on modern technology, such energetic events directed towards the Earth can prove to be extremely harmful. Energetic particles from the Sun can damage satellite electronics and prove fatal for the astronauts; x-rays from solar flares can damage radio communication systems, and CMEs can cause geomagnetic storms, GPS failure, and knock out the power grids. Therefore, gaining a better understanding of the physics of such phenomena in order to predict them and to employ precautionary measures has never been more critical.

1.1 Solar Coronal Heating Problem

The corona is the tenuous outermost layer of the solar atmosphere. In visible light, It is about six orders of magnitude fainter than the surface (photosphere), and therefore, only visible during a total solar eclipse or through a coronagraph. For thousands of years, total solar eclipses have been observed by humans; by the mid 19th century, we started making photographic records of the corona and prominences. In the years that followed, spectroscopic observations of the corona were made possible, by which helium was discovered by Jules Janssen in 1868. However, it was not until the early 1940s that forbidden lines for highly ionized iron (e.g., Fe X) were identified in the coronal spectra [84, 59]. Based on the new findings, Alfvén [1] concluded that the solar corona must have extremely hot temperatures [see [144] for a historical review]. The effective temperature of the forbidden line Fe X is ≈ 1 MK, so the temperature of the corona must be a few million degrees, three orders of magnitude higher than the ≈ 5800 K at the photosphere (see Figure 1.1 for the density and temperature profiles as a function of height above the photosphere). How is the corona heated to a few million degrees, how is high temperature maintained and how is the energy dissipated? That is the coronal heating problem.

A majority of energy losses from the corona are in the form of radiation (by EUV and x-rays) and conductive losses. To account for these losses, an energy flux input of $\approx 10^7$ ergs cm^{-2} s^{-1} is required for the active region corona and that of $\approx 3 \times 10^5$ ergs cm^{-2} s^{-1} for the quiet Sun [203]. In the last few decades, many theories have been proposed to explain the sustained energy source, two of which are predominant. Both theories are driven by the random convective motions in the photosphere that displace the footpoints of the coronal loops. If the motions are slower than the characteristic Alfvén travel time, the field is stressed quasi-statically, meaning that there is a slow build-up of stress. The dissipation of such stresses is known as **direct current (DC) heating**. Conversely, disturbances faster than the

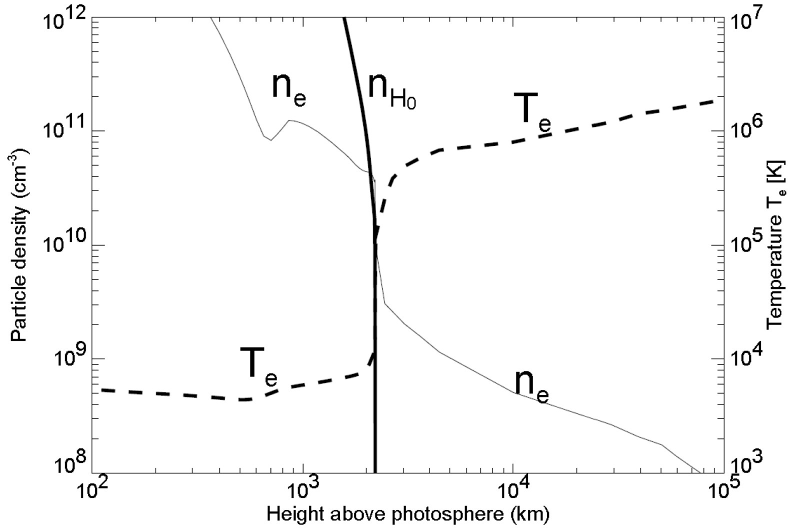

Figure 1.1 Temperature (dashed line) and density (solid line) profile as a function of height above the photosphere. Chromospheric model based on FAL-C [63], and the transition region and lower corona model based on [67].
Source: [7]

Alfvénic travel time will propagate as waves along the field; accordingly, the energy dissipation is referred to as **alternate current (AC) heating**. The Alfvén travel time is defined as the time it takes for an Alfvén (or magneto acoustic) wave to travel along the loop to the other footpoint and back while moving at the Alfvén velocity, $v_A = B/\sqrt{4\pi\rho_o}$, where B, is the magnetic field strength, and ρ_o is the background mass-density.

AC Heating The photospheric convective motions generate waves that propagate upward into the chromosphere and the corona. It was initially suggested that acoustic waves might be transporting energy into the corona [164]. Subsequent modeling, however, showed that while acoustic waves might be heating the chromosphere, they would form shocks at low heights and become highly damped before they reach the corona. Alfvén waves, on the other hand, are incompressible and may transfer their energy in the corona through turbulent dissipation or phase mixing [2, 139, 138, 92]. In the last decade or so, high-resolution observations of the solar atmosphere have shown that MHD waves are ubiquitous in the solar atmosphere [see [45] and references therein] and that they may carry enough energy to heat the quiet Sun and solar wind [46, 88]. However, evidence of energy transfer sufficient enough to heat the corona is still lacking.

DC Heating Parker [140, 141] hypothesized that the same photospheric motions as mentioned above also twist and entangle the magnetic fields. This is a slow process that builds up the non-potential magnetic energy, which is then released suddenly in the form of an impulsive burst. This process of release of magnetic energy to thermal and kinetic energy is called magnetic reconnection. Parker referred to such bursts as nanoflares and claimed that a ubiquitous presence of nanoflares can collectively heat the corona [see also [97, 98] and references within]. For over a few decades now, the definition of nanoflares has been adapted to represent a small-scale impulsive release of energy irrespective of the underlying mechanism. In the Parker picture, one can write the Poynting flux through the surface as:

$$F = -\frac{1}{4\pi} B_v(\boldsymbol{B_h}.\boldsymbol{v_h}) \tag{1.1}$$

where B_h and B_v are the horizontal and vertical components of the field and v_h is the velocity of the footpoint motions. The velocity of the footpoint motions is measured to be $v_h \sim 10^5$ cm/s, and values for B_v can be obtained from high-resolution magnetograms. The magnitude of the flux thus calculated, assuming $B_h = B_v$, is sufficient to heat the quiet Sun and the active regions. A more significant question is how the energy is converted. A promising idea is that a nanoflare occurs when the angle between the braiding field lines reaches a critical value (critical shear angle); however, an investigation to understand other conditions that are responsible for the onset of reconnection is still ongoing [for details, see [106]].

Both mechanisms may play a role in heating the corona, although the dominance of one mechanism over the other in different regions on the Sun remains unclear. Irrespective of the underlying mechanism, heating in the corona is thought to be impulsive [98], meaning that the time taken for energy release is much smaller than the cooling time of the loop. Recent efforts to better understand coronal heating have concentrated on its properties viz. magnitude, frequency, scaling with the strength and length of magnetic strands, etc., without implying a specific underlying mechanism. For the active corona, several observational studies have examined active region cores, while others have employed hydrodynamic models of coronal loops to investigate the slopes of emission measures (EM) in regards to the heating properties [201, 177, 48, 21, 28]. Forward modeled active regions have also been generated, to which a prescription of heating is applied, yielding EUV images and emission measures, which are then compared to the observations [128, 10, 162].

1.2 Impulsive Phenomena on the Sun

All energetic events on the Sun are a result of some disturbance destabilizing the magnetic field on varying spatial scales. Some examples are nanoflares, spicules, jets, prominences, solar flares, and CMEs. In this section, we discuss a few of the large-scale impulsive events.

Solar Flares Solar flares are large explosive events on the Sun seen as sudden brightenings with intense radiation observed at almost all wavelengths in the electromagnetic spectrum, releasing up to 10^{32} ergs of energy, although only the strongest flares show strong emission in white light. The very first record of a solar flare was reported from white light observations made by Carrington [31] in 1859, during his daily monitoring of the sunspots. Magnetic reconnection is widely accepted as the driver of a solar flare. Upon reconfiguration of magnetic fields, the stored magnetic energy is dissipated, resulting in the acceleration of energetic particles and thermal energy exuded along the field lines [145].

There are three phases recognized in the evolution of a flare [13]. In the *preflare phase*, some rise in activity is observed at soft X-ray (SXR) and EUV wavelengths as the plasma heats, followed by a sudden energy release and acceleration of energized particles (electrons and ions) known as the *impulsive phase*. Bright, hard X-ray (HXR) footpoints are seen at lower altitudes as the energized plasma propagates downward into the chromosphere. Accelerated electrons escaping in an open field produce type III bursts (Section 1.4). This is generally accompanied by bright emission at radio frequencies that can come from high-energy particles trapped in the field. The hot plasma appears as loop top sources in SXR. Most of the flare energy is released during this impulsive phase lasting a few minutes. The gradual decline in the SXR radiation marks the *decay phase* of the flare, where the coronal plasma slowly cools down to preflare temperatures. Spike bursts and continuum emission at metric frequencies may be observed at this time. Based on their peak

X-ray flux, as observed by the Geostationary Operational Environmental Satellites (GOES), the flares are classified as A, B, C, M, and X, with A-class flares having a peak flux of $< 10^{-7}$ W/m^2. The flux increases by an order of magnitude with each class ending at X-class with 10^{-4} W/m^2. The subclasses within each class scale from 1-9, depicting the multiplicative factor for the peak flux, so an X6 flare has a peak flux of 6×10^{-4} W/m^2.

The CSHKP model or the **"standard" flare model** [30, 170, 91, 104] shown in Figure 1.2 is generally used to explain the flare dynamics. Reconnection takes place high up, in the current sheet (top panel, Figure 1.2) and releases an enormous amount of energy, accelerating particles and creating bulk flows in the upward and downward direction. The lower loops respond to the downflows in multiple ways. The highly energetic particles (mostly electrons) hit the loops below the current sheet producing HXR emission at the loop-tops; those that reach the chromosphere "collide" with the dense plasma to create HXR footpoints. Thermal conduction from the corona rapidly increases the temperature and density in the upper chromosphere. As a result, the material expands into the corona filling the post-flare (reconnected) loops via chromospheric evaporation. On the other hand, the upflows aid the rise of the flux rope that ejects outward in the form of a CME.

Coronal Mass Ejection A Coronal Mass Ejection is an eruption in the solar atmosphere that transports plasma and magnetic fields across the interplanetary medium. The first CME was observed in 1971 [176] using the coronagraph onboard Orbiting Solar Observatory (OSO-7). Originally, CMEs were defined as white light features of coronal structures exhibiting outward motion, as seen in coronagraphs. However, further observations revealed that CMEs also show signatures at X-ray, EUV, and radio wavelengths [99, 80, 49, 82]. Typically, a CME can have velocities (projected radial velocity of the CME-front) ranging between $50 - 2000$ km/s, with

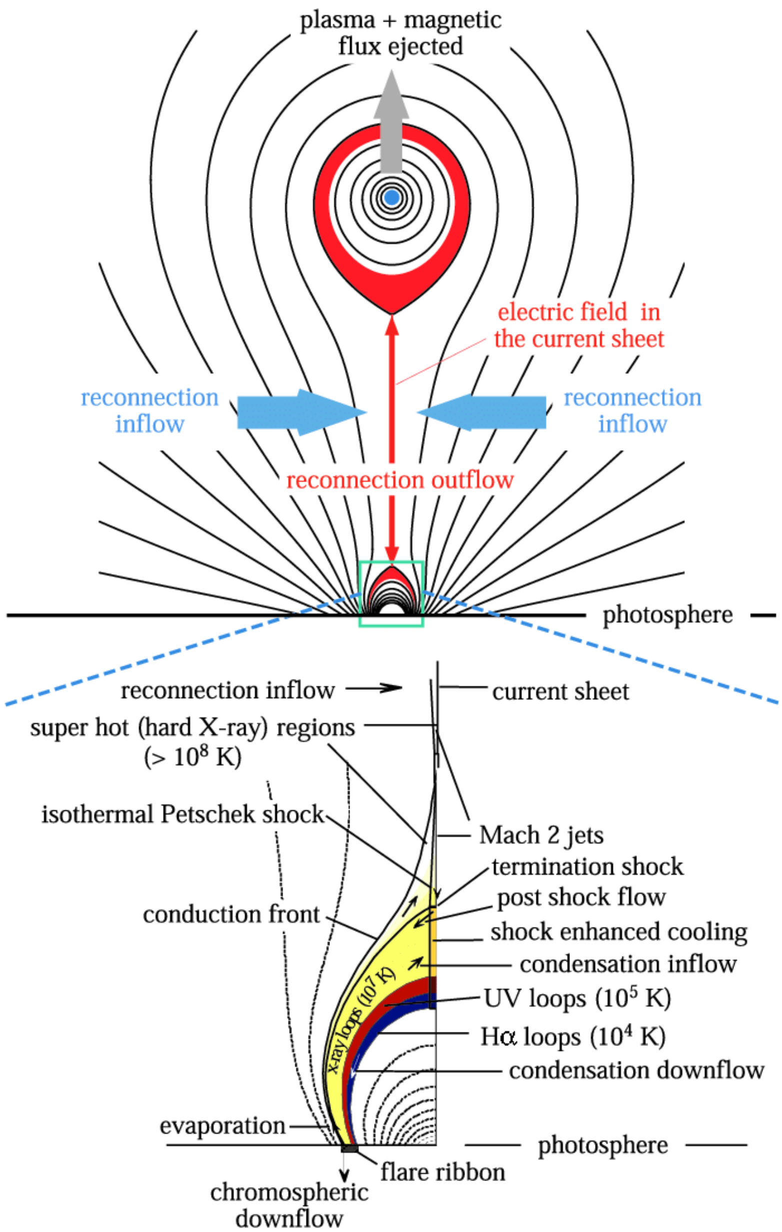

Figure 1.2 Top: Standard flare/CME model showing the current sheet with post-flare loops underneath and erupting flux rope above. Bottom: Enlarged view of the post-flare loops.

Source: [110, 64]

an average of 300 km/s during the solar minimum and 500 km/s during solar maxima [206] carrying an average mass of 10^{12} kg [79].

CMEs often accompany flares; however, many large flares (GOES class C, M, or X) have been observed to show no association with CMEs [189, 205]. Although, just like flares, they are also thought to be the manifestation of magnetic reconnection as demonstrated in the *standard flare model*. A typical CME has a three-part structure [93] that includes a bright front (also known as the leading edge), a dark cavity, and a bright, dense core. Shocks may develop in front of the fast-moving leading edge that can accelerate electrons to produce type II bursts or herringbone structures (see Section 1.4) [134]; while the core of the CME can produce gyrosynchrotron emission at metric frequencies [113, 179, 29].

1.3 Solar Radio Emission

Radio emission from the Sun can be produced via multiple mechanisms that involve converting the energy of moving electrons of either thermal or non-thermal nature into electromagnetic radiation. The two characteristic radio frequencies, plasma frequency, ν_p and the gyro frequency, ν_B, have an intrinsic sensitivity to plasma parameters, viz. ambient density, n_e, and the field strength, B, thus opening up great diagnostic opportunities to probe the magnetic field and the plasma in the corona and the chromosphere. Radio emission allows us to explore not only strong, impulsive bursts, but it also has the potential to reveal structures in the quiet Sun that may not show any substantial signature at other wavelengths.

Following from the radiative transfer equation [52], for a homogeneous source, the *intensity*, I at frequency ν is given by the Planck function under the Rayleigh-Jeans limit ($h\nu \gg kT$):

$$I_\nu = \frac{2kT_b\nu^2}{c^2} \quad [\text{J m}^{-2}\ \text{Hz}^{-1}\ \text{sr}^{-1}] \tag{1.2}$$

where k is the Boltzmann constant, and T_b is the *brightness temperature.* The brightness temperature, T_b is not always equivalent to the physical temperature of the source and can be thought of as the temperature of an equivalent blackbody, to emit the same brightness as that of the source. The expression for the same is given by the radiative transfer equation:

$$T_b = T_o \exp^{-\tau_\nu} + T_{source}(1 - e^{-\tau_\nu}) \quad [\mathrm{K}] \tag{1.3}$$

where the first term on the r.h.s. is the emission from an "external" source, τ_ν is the *optical depth*, and $T_{\text{source}} = T_e$ i.e., the electron temperature in case of thermal emission. For a non-thermal source, $T_{\text{source}} = T_{\text{eff}} = \langle E \rangle / k$ i.e., the *effective temperature or kinetic temperature* of the source with emitting particles of mean energy $\langle E \rangle$. In the *optically thick regime* ($\tau_\nu \gg 1$) Equation (1.3) is reduced to

$$T_b = T_{source} \quad [\mathrm{K}] \tag{1.4}$$

and in the *optically thin regime* ($\tau_\nu \ll 1$) it is given as:

$$T_b = T_o(1 - \tau_\nu) + T_{source}\tau_\nu \quad [\mathrm{K}] \tag{1.5}$$

The flux density S_ν is then expressed as the integral of the intensity over the solid angle $d\Omega$

$$S_\nu = \int \frac{2k_B T_b \nu^2}{c^2} d\Omega \quad [\mathrm{W\ m^{-2}\ Hz^{-1}}] \tag{1.6}$$

The solid angle $d\Omega$ is given by the angle subtended by the source, or for an extended source with an angular size that is bigger than the field of view of the instrument, $d\Omega$ is equal to the beam size.

The resulting radiation can be incoherent or coherent based on the underlying mechanism.

1.3.1 Incoherent Emission

Incoherent emission comes from individual electrons that exhibit no phase association. The total intensity of the emission is proportional to the number of radiating electrons. The brightness temperature of incoherent emission is always less than or equal to the effective temperature of the source, $T_{\rm eff}$, i.e., the physical temperature for a thermal source and the kinetic temperature for a non-thermal source as mentioned above. The shape of the T_b spectrum can be quite useful in estimating the plasma properties. At radio wavelengths, the two most important categories of incoherent emission observed from the Sun are: Bremsstrahlung or free-free emission and gyromagnetic emission [see [135] for a detailed review].

1.3.1.1 Bremsstrahlung or Free-Free Emission. The German word for "braking radiation", bremsstrahlung, refers to emission produced by collisions between charged particles (Coulomb collisions). In the highly ionized solar corona, it is also referred to as free-free emission due to the collisions between free particles. A slight deflection of electrons (small-angle approximation) from the Coulomb field of the ambient ions produces emission at radio frequencies, while a head-on collision between the two may cause an electron to lose most of its energy as it is reflected, generating emission at x-ray frequencies. Bremsstrahlung dominates the quiet Sun emission at radio wavelengths [74, 52] and contributes significantly to emission from non-flaring active regions. For a simple two-layer model of the emission [52, 160], where the optical depth for solar atmosphere is expressed as:

$$\tau = \int \kappa \; dl \tag{1.7}$$

where

$$\kappa \approx \frac{1}{3c}\left(\frac{2}{\pi}\right)^{1/2}\frac{\nu_p^2}{\nu^2}\sum_i Z_i^2 n_i \frac{4\pi e^4}{m_e^{1/2}(k_B T)^{3/2}}\frac{\pi}{\sqrt{3}}\, G(T,\nu) \tag{1.8}$$

is the absorption coefficient, l is the path length, ν_p is the plasma frequency, Z_i and n_i are the ion charge and number density, m_e is the electron mass, and G is the gaunt factor [52]. At low frequencies, the corona is optically thick to free-free emission and slowly becomes optically thin as the frequency increases. Following from Equation (1.3), the radiative transfer equation is then given as:

$$T_b = T_{chr}(e^{-\tau_{cor}}) + T_{cor}(1 - e^{-\tau_{cor}}) \quad [\mathrm{K}] \tag{1.9}$$

where, T_{chr} is the electron temperature of the optically thick chromosphere, and T_{cor} is the electron temperature of the corona. For the optically thin corona, $\tau_{\mathrm{cor}} \ll 1$, the above equation predicts an inverse dependence of T_b on ν^2. Figure 1.3a shows the universal spectra [70] for free-free emission. For a homogeneous source, the shape of the spectra does not change with a change in density n or temperature T; rather, it just shifts in the directions shown by the arrows in Figure 1.3a. However, in the case of an inhomogeneous source, the shape of the spectra may change contingent on the variations along the line of sight [72]. Understanding the source spectrum allows us to measure the temperature as a function of frequency (and therefore height) in the optically thick regime. Alternatively, [159] have used the spectral gradient at submillimeter wavelengths to get a diagnostic on optical depth. For a few decades now, the index of the F10.7 cm (flux density at 2.8 GHz) has been used as a proxy for EUV emission given the same dependence of optically thin bremsstrahlung flux and EUV differential emission measures (DEMs) on the density of the plasma [39, 40, 65, 172, 163]. White White et al. [196] showed another example of using EUV

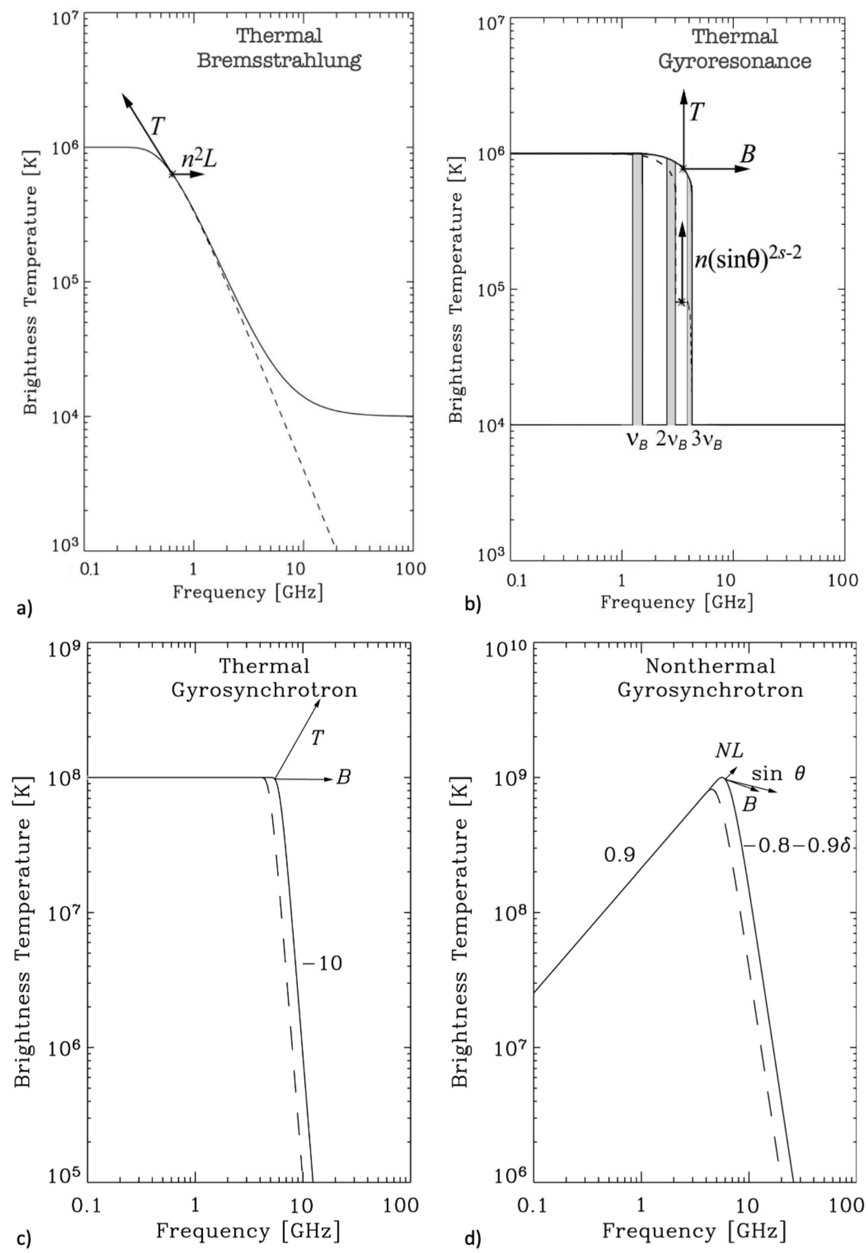

Figure 1.3 "Universal Spectra" shown in a) for thermal free-free brightness temperature. The solid line show contribution from a corona at 1 MK and the chromosphere at 10^4 K. The dashed line show the contribution from corona only; b) for thermal gyroresonance emission from a homogeneous source c) for thermal gyrosynchrotron emission from a homogeneous source and d) for gyrosynchrotron emission from a non-thermal source. The solid lines in panels b, c, and d represent the *x*-mode spectra and the dashed lines show the *o*-mode spectra.

Source: [72]

observations in combination with radio data to constrain the elemental abundance of iron in the corona.

1.3.1.2 Gyroemission.

Gyromagnetic emission is produced by free particles that are accelerated in the presence of a magnetic field B. The Lorentz force alters the direction/velocity of the electron, consequently providing it centripetal acceleration. This causes the electron to gyrate around the field, with a frequency ν_B that is directly proportional to the field strength B and is expressed as:

$$\nu_B = \frac{eB}{2\pi m_e c} \approx 2.8 \times 10^6 B \ \ [\mathrm{Hz}] \tag{1.10}$$

Different energy regimes invoke slightly different forms of gyromagnetic emissions. At low energies (thermal distribution), the electrons exhibit mild beaming, emitting at frequencies $s\nu_B$, for small values of s where $s = 1, 2, 3...$ is the harmonic number. The emission is referred to as *gyroresonance* emission. Gyroresonance is the dominant mechanism in the lower corona, over sunspots where the magnetic field is stronger ($> 100\ G$). The opacity τ_ν for gyroresonance depends on multiple parameters: density, n_e, temperature T, and field B along the line of sight and angle θ between B and the line of sight. The characteristic spectrum from gyroresonance is shown in Figure 1.3b. The emission becomes optically thick in the x-mode at higher harmonics compared to o-mode. Given the availability of multi-frequency observations, one can identify the harmonics from the spectrum and estimate the magnetic field in the region [see for example [70, 178]]. Variation in the parameters above will shift the spectrum as marked by the arrows in Figure 1.3b. A detailed review of the gyroresonance emission and observations can be found in Nindos [136] and Gary & Keller [72] gives a comprehensive overview of the gyroresonance diagnostics.

At higher energies (< 1 MeV), the mildly relativistic electrons gyrating around the field emit *gyrosynchrotron* radiation at microwave frequencies with s = 10–100. The electrons can have either thermal or non-thermal energy distributions. Gyrosynchrotron is the dominant emission in flares. Occasionally, it is also observed in association with CMEs and smaller transient brightenings. Dulk [52] gave the empirical expressions for $T_{\rm eff}$, τ, $\nu_{\rm peak}$ etc., for an isotropic power-law electron distribution.

$$T_{eff} \approx 2.2 \times 10^9 10^{-0.31\delta} (\sin\theta)^{-0.36-0.06\delta} \left(\frac{\nu}{\nu_B}\right)^{0.50+0.085\delta} \tag{1.11}$$

$$\frac{\kappa_\nu B}{n_e} \approx 1.4 \times 10^{-9} 10^{-0.22\delta} (\sin\theta)^{-0.09-0.72\delta} \left(\frac{\nu}{\nu_B}\right)^{-1.30+0.98\delta} \tag{1.12}$$

$$\nu_{peak} \approx 2.72 \times 10^3 10^{0.27\delta} (\sin\theta)^{0.41+0.03\delta} (n_e L)^{0.32-0.03\delta} \tag{1.13}$$

where δ is the electron power-law index, and $\nu_{\rm peak}$ is the peak frequency for the emission. The equations are more reliable for $\delta \lesssim 6$, and small θ values [55]. The characteristic spectrum for both thermal and non-thermal energy distributions is shown in Figure 1.3 (panels c and d). The emission is optically thick at lower frequencies and peaks where $\tau \sim 1$ and falls at higher frequencies. Equation (1.11) is relevant in the optically thick regime and reflects on the variations in the effective energy E of the electrons [72] although Razin suppression [150] may change the shape of the slope at lower frequencies. While Equation (1.13) is relevant for optical depth unity exhibiting how the peak frequency will shift based on the column density $n_e L$, Equation (1.12) is applicable to the optically thin part of the spectrum and is influenced by the energy distribution of the electrons, though see Fleishman & Melnikov [62] for effects of anisotropic pitch-angle distribution on the polarization and the slope of the spectrum at higher frequencies. Although approximations given by Equations (1.11–1.13) are useful for rough estimates of gyrosynchrotron emission, the far more exact and more widely applicable numerical fast codes developed by Fleishman & Kuznetsov [61] have replaced them for estimating plasma parameters from gyrosynchrotron spectral fitting. Multi-frequency observations of gyrosynchrotron emission can prove instrumental in understanding the evolution of magnetic field morphology during a flare [68].

1.3.2 Coherent Emission

Electrons that are accelerated in phase with each other can produce photons that are also in phase. Such emission that is generated by the collective behavior of particles is referred to as coherent emission. The brightness temperature, T_b in this case, can be much greater than the thermal temperature T_e of the source. The two classes of coherent emission relevant to solar radio emission are plasma emission and electron cyclotron maser emission (ECME).

1.3.2.1 Plasma Emission. The theory of plasma emission was initially developed by Ginzburg & Zhelezniakov [75] to explain the observed properties of solar radio bursts reported by Payne-Scott [142] and Wild & McCready [198]. The general concept of their proposed theory remains the same, with certain upgrades that were made over the years [208, 209, 123, 156, 126, and references within]. There are three stages of the theory: generation of Langmuir waves/plasma waves, scattering or coalescence of Langmuir waves to produce fundamental emission, and coalescence of Langmuir waves to produce harmonic emission.

Impulsive bursts on the Sun can inject accelerated beams ($\sim 0.1 - 0.5c$) of electrons along the field lines. As the beam propagates through the field, the faster electrons outrun the slower ones, creating a two-stream instability (bump-on-tail

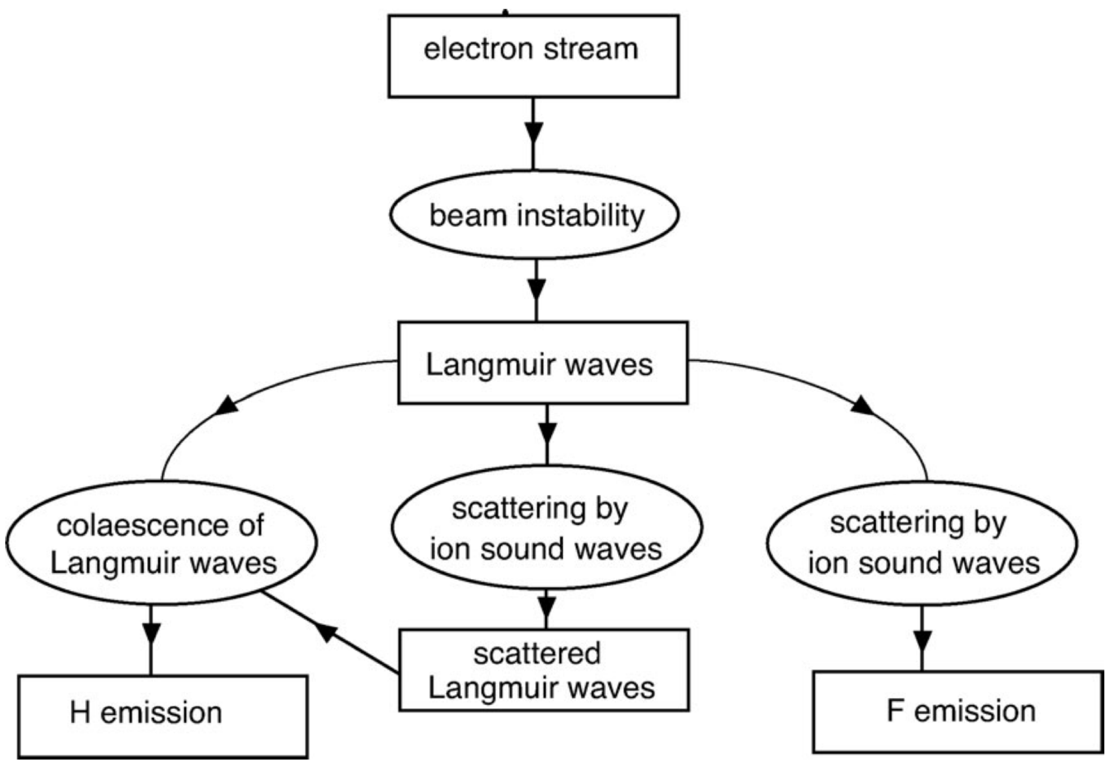

Figure 1.4 Flow chart of the different stages in the production of fundamental (F) and harmonic (H) plasma emission.
Source: [125]

instability) which can be described as a positive slope in the tail (or high-energy portion) of the electron energy distribution. The beam instability generates the Langmuir waves, which are longitudinal electrostatic waves and can only be detected in-situ. The conversion of energy in Langmuir waves (L) to transverse (T) waves that can escape as radiation requires complex non-linear interactions between Langmuir waves and ions acoustic waves (S). Figure 1.4 shows a flow chart of all the interactions involved in the generation of plasma emission. The interaction between L and S produces electromagnetic emission at the fundamental plasma frequency, ν_p:

$$\nu_p = \sqrt{\frac{n_e e^2}{\pi m_e}} \approx 8980\sqrt{n_e} \quad \text{[Hz]} \tag{1.14}$$

A coalescence of L with a back-scattered Langmuir wave L' generates emission at the second harmonic, $2\nu_p$. The fundamental frequency ν_p lies below the cut-off frequency for x-mode. This implies that the fundamental emission should be 100% polarized in o-mode. Type I noise storms and a fraction of all type III bursts exhibit high polarization in o-mode; however, a type III that is 100% polarized in o-mode has not been observed. A plausible explanation is that propagation effects through an inhomogeneous (fibrous) corona can cause depolarization, although it requires the density gradients to be really steep at the edges of the fibers [see [193, 125] for details].

1.3.2.2 Electron-Cyclotron Maser Emission (ECME). ECME is commonly observed from Jupiter (decametric radiation (DAM)) [23] and in Earth's outer atmosphere as auroral kilometer radiation (AKR) [87]. Solar ECME has also been observed in the form of spike bursts [52], although it is not as common. An example of ECME as the driving mechanism for a moving type IV burst can be found in

Morosan et al. [131]. The radiation is emitted near the electron-cyclotron frequency ν_B (Doppler shifted) for small harmonics expressed as:

$$\nu = s\nu_b + \frac{k_{||}v_{||}}{2\pi} \tag{1.15}$$

where $k_{||}$ and $v_{||}$ are the parallel wave number and the parallel component of velocity of the electrons respectively. As an energetic (mildly-relativistic) beam of electrons is injected into the ambient plasma, if the density n_e is low enough such that $\nu_p < \nu_B$, cyclotron emission is favored over plasma emission. A loss-cone instability [204] is believed to be the predominant mechanism that triggers ECME. In a magnetic bottle geometry with a converging field on both ends, as the electrons move from low B to high B, in order to conserve the magnetic moment μ, the parallel component of the electron velocity $v_{||} \to 0$ as $B \to B_{\max}$. The electrons are trapped in the magnetic bottle and mirror between the two ends for a $\theta > \theta_m$. Here θ is the initial pitch angle of the moving electrons and θ_m is given as:

$$\sin^2(\theta_m) = \frac{B_0}{B_{max}} \tag{1.16}$$

The mirroring electrons then resonate to produce ECME at frequency ν (from Equation (1.15)). Electrons with $\theta \leq \theta_m$ precipitate into the atmosphere or escape into the loss-cone. The emission is dominantly polarized in x-mode.

1.4 Solar Radio Bursts

Solar radio bursts are produced by interactions between energetic particles and the ambient plasma, and can be observed over a wide range of frequencies and in a variety of forms. The first signatures of these "enhancements" above the solar background emission were observed in the late 1940s at single frequencies and were referred to as "outbursts" by Allen [3]. While Payne-Scott [142] divided them into two categories:

bursts that exhibit circular polarization and bursts that do not, it was only in the 1950s that they were characterized according to their unique features, as seen in the dynamic spectra [198]. Three classes of radio bursts were identified first: types I, II, and III, based on how the frequency of the burst changes with time (also known as the frequency drift rate). Two other spectral classes, type IV and V, were added in the late 1950s [16, 200]. Each of these types may be classified into further subtypes depending on their complexity, fine structure, etc. Bursts of types II, III, and IV are usually associated with flares and CMEs and therefore are of particular interest. Figure 1.5 shows a schematic diagram illustrating spectral features of each type. A concise description of the characteristics and associated phenomena for each burst type is given in Table 1.1.

1.4.1 Type I

Bursts of type I can be observed as singular spikes or in chains, although they are most commonly observed as noise storms superimposed over continuum emission [76, 60]. Daigne [44] showed that these bursts were highly localized, and their position coincided with that of the underlying continuum. Individual bursts are short-lived and may last less than a second up to a few seconds, while the storms can go on for days at a time.

They are typically observed at lower frequencies ($\sim$ 50–500 MHz) [118] characterized by their narrow bandwidth ($\Delta\nu/\nu \sim 0.02$) [18] (shown in cyan in Figure 1.5) and were initially thought to exhibit no drift in frequencies. Although recently, Yu et al. [207] presented evidence of frequency drifts in individual type Is using high-resolution observations from the Very Large Array (VLA). Fundamental plasma emission is the plausible underlying mechanism given the high circular polarization ($\lesssim$ 100%) seen in the bursts [125]; however, there is no clear consensus on what causes the initial particle acceleration. While type I storms do not show any association

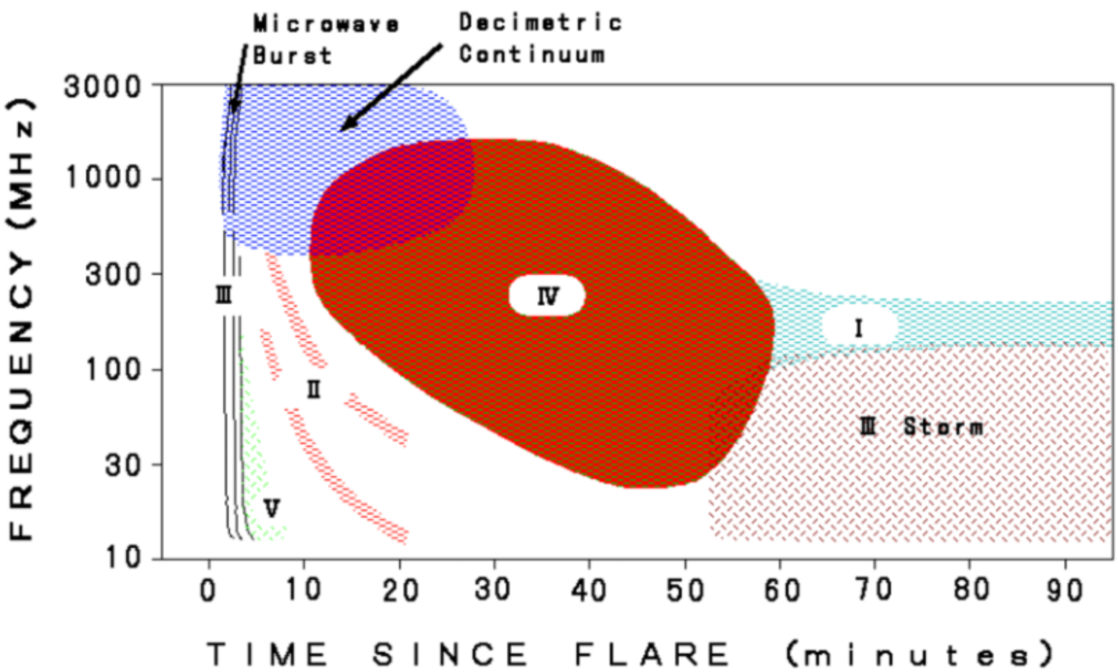

Figure 1.5 Schematic diagram showing the classification of Solar Radio Bursts. *Source:* `https://sunbase.nict.go.jp/solar/denpa/hiras/types.html`, accessed on 02/23/2021.

with flaring activity, their presence has been linked to active regions. Several studies suggest that reconnection (both, between closed field lines and interchange reconnection) may be accelerating particles to produce noise storms that accompany type Is [see, for example, [47, 114]].

1.4.2 Type II

Type II radio bursts are identified by their slow drifts (~ 1 MHz s^{-1}) in the dynamic spectrum from high to low frequency. The emission is usually observed at the fundamental plasma frequency with second harmonic structures seen in many cases with little to no circular polarization [198]. Different features are commonly seen in the spectra of type IIs, e.g., "split-band" feature where the fundamental or harmonic structure may split itself into two parallel lanes [121, 188], and "herring-bone" structure [25] showing spikes along the spine of the bursts moving in both directions (from low to high and high to low frequencies).

Plasma emission excited from shock-accelerated electrons is the most prevalent hypothesis for the generation of type II bursts [134, 180, 112, 78]; however, there have been reports where the underlying mechanism was found to be synchrotron emission [11]. Type IIs are observed in association with flares and CMEs, while CME-driven shocks are responsible for deca-hectometric (DH) type IIs; it remains unclear what creates the shocks for metric type IIs. There are two proposed sources: CME-driven shocks [26, 38, 83] and flare blast-waves [107, 77].

1.4.3 Type III

Type III radio bursts are best characterized by their high frequency drift rate, marked by solid black lines in Figure 1.5. Attributed to plasma emission, traditional type IIIs are generated from beams of accelerated electrons moving at semi-relativistic velocities ($\sim 0.3 - 0.5c$) along open field lines. Traditional interplanetary type III bursts may last for a few minutes up to tens of minutes, while coronal type IIIs observed at high frequencies (> 500 MHz) may last a few milliseconds up to a few seconds [32, 33]. Type III storms lasting hours or days can consist of thousands of bursts per hour. When trapped in closed magnetic structures, they eventually turn toward the Sun, resulting in inverted U or J-shaped bursts in the dynamic spectra. Like bursts of type II, type IIIs also exhibit weak circular polarization [120] ($5-50\%$) [56]. However, it is not yet clear what causes the reduction in the degree of polarization and why there have been no instances of type IIIs observed with 100% circular polarization in the fundamental component [though see, [192, 124, 125]].

A clear association has been established between Type IIIs and hard x-ray (HXR) flares. However, several studies have shown that not all flares are accompanied by type IIIs [95, 6, 195, 154, 151, 24, and references within]. Additionally, the direct dependence of the type III frequency on the local plasma density allows tracing the burst locations in frequency and time, making them a great diagnostic tool for investigating plasma properties and understanding other processes like particle acceleration and magnetic reconnection that are observed in impulsive events on the Sun as well as in astrophysical plasmas across the universe [33]. An extensive review of the recent observations of type III bursts can be found in Reid [151].

1.4.4 Type IV

Identified by Boischot [16], spectral type IV burst radiation is characterized by radio continua over a broad range of frequencies often associated with flares. The onset may be triggered by the radiation of energetic electrons trapped within magnetic structures and plasmoids. Type IV bursts are recorded in almost all frequency ranges, starting from the microwaves as type IV bursts and the decimetric range as type IVdm [12].

Weiss [190] characterized these bursts at metric wavelengths into moving (type IVm) and stationary type IV bursts. Stationary type IVs are observed over long-durations (hours-days), displaying a variety of spectral structure superposed on broad, continuous spectra with little or no source movement. They can constitute multiple source locations, each with relatively small source diameter and strong polarization (usually in o mode) [52]. The primary emission mechanism for these bursts is thought to be gyrosynchrotron emission at high frequencies, and plasma emission at low frequencies [52, 69, 29]. Moving type IV bursts are relatively short-lived (tens of minutes to a few hours), with ill-defined spectral features, rapid outward movement through the corona (of the order of hundreds to thousands km s^{-1}), and sometimes a polarization in x-mode. While type IV bursts have been investigated extensively over the past few decades, the underlying mechanism remains unclear. A more detailed review of recent results can be found in Section 2.1.

1.4.5 Type V

Bursts of type V are short-lived diffuse continuum emission frequently preceded by type IIIs or group of type IIIs lasting just a few minutes (< 5 min) [200]. They are observed at low frequencies with an upper limit of ∼200 MHz and exhibit little to no circular polarization [53], usually with the sense opposite to that of the accompanying type IIIs [202]. The source sizes of type V bursts have been observed to be larger than those of type IIIs, with some displacement seen between their source heights [157, 53]. Wild [199] suggested that these bursts are caused by synchrotron radiation from relativistic electrons. The theory was soon rejected by Weiss & Stewart [191], who proposed plasma radiation as the emission mechanism suggesting that the coherent plasma waves are excited by electrons trapped in coronal loops (see also, [157, 158]). On the other hand, Winglee & Dulk [202] claimed that electron-cyclotron instability from a loss-cone distribution can better explain the observed properties of type V bursts [see also [171]].

Table 1.1 Characteristics of Principal Identified Radio Bursts

Incoherent radio bursts	**Emission Mechanism**	**Source**
Microwave and millimeter bursts	free-free emission	Thermal plasma
Type IV burst continua	Gyrosynchrotron emission	
Millimeter		*Ultra-relativistic electrons*
Microwave and dm-dam		*Relativistic electrons*
Coherent radio bursts		
Dm-dam type IV bursts	plasma emission	Trapped energetic electrons
Type II bursts	ν_p;$2\nu_p$	Shocks
Type III and V bursts	ν_p;$2\nu_p$	Upward propagating electron beams
Reverse slope bursts	ν_p;$2\nu_p$	Downward propagating electron beams
TypeJ and U bursts	ν_p;$2\nu_p$	Beams along close loops
Dm-m pulsations	$\nu = s\nu_B$	Loss-cone instability *trapped electron*
Dm spikes		Loss-cone instability
Dm-m type I storms	plasma emission	trapped and escaping
Dam-Km type III storms		accelerated electrons

ν_p = plasma frequency; ν_B = gyro frequency *Source:* [72].

1.5 Motivation and Outline

The work presented in this thesis covers two different research studies. Radio diagnostics are at the heart of both projects. As mentioned above, in addition to variations in the solar magnetic activity due to the 11-year solar cycle, transient large-scale energetic events from the Sun play a vital role in driving the day-to-day space weather and the ionization state of Earth's upper atmosphere. While these phenomena are observed at a range of wavelengths, radio observations have the capability of providing valuable context, by probing energetic particles and plasma in the solar corona where X-rays or EUV may have limitations. Additionally, new multi-frequency high-resolution observations from radio interferometers allow us to investigate the magnetic topology at reconnection sites, something that has not been done before [33, 68]. Taking advantage of this new era in solar radio astronomy, we conduct our research.

We use one such instrument to conduct our first study that aims at investigating radio emission from large-scale energetic events on the Sun, in order to understand better the underlying physical mechanisms that trigger these bursts. In Chapter 2 we explore a flare-CME event using radio observations from the Owens Valley Radio Observatory-Long Wavelength Array (OVRO-LWA) that exhibits complex radio phenomena. This work also explored the limitations of LWA for solar observations, serving as the basis for an upgrade being performed on the array currently.

Another excellent example of the advantages of radio observations is that of investigating fundamental processes such as particle acceleration and magnetic reconnection at small-scales. While HXR emission is a primary tool to investigate acceleration from energetic particles, the current instruments limit the detection of numerous mildly-energetic particles that may be produced by nanoflares [89, 94, and references therein]. The emission is believed to be dominated by the thermal component at those energies. Radio emission does not suffer from such limitations.

While both full-sized flares and nanoflares are claimed to be triggered by reconnection, their magnetic configuration is different from one another. The magnetic field geometry of a full-sized flare involves a weak component of the guide field. On the contrary, a strong guide field may be operating in a nanoflare geometry. A leading theory on particle acceleration from reconnection events predicts that the presence of a strong guide field may not be efficient in accelerating particles [51, 43]. Which brings us to the goal of our second study: Do nanoflares accelerate particles like full-sized flares? If so, how efficiently?

The first step to answer this question lies in modeling radio emission from type III bursts produced by particles accelerated from nanoflares. Since nanoflares are ubiquitous in the corona, we expect hundreds of overlapping bursts that are difficult to detect by the naked eye. Chapter 3 presents the modeling of emission from such bursts and testing whether such emission can be detected in the data using the novel time-lag technique [183]. In Chapter 4, we move to the second step. We analyze radio observations from the FIELDS experiment onboard the Parker Solar Probe (PSP) to search for signatures of type III bursts from small-scale reconnection events. Chapter 5 summarizes the important results from the studies presented and discusses the current endeavors and future scope of the work.

CHAPTER 2

IMAGING SPECTROSCOPY OF CME–ASSOCIATED SOLAR RADIO BURSTS

2.1 Introduction and Motivation

Since their discovery in the 1950s [198], solar radio bursts have been the subject of intense investigation. As discussed in Chapter 1, radio diagnostics hold great importance for characterizing the space environment at the Sun, near Earth, and elsewhere in the solar system. Therefore the study of these phenomena, both spatially and spectrally, contributes significantly to our understanding of the properties of the ambient medium, the instabilities that may cause them, and subsequently, the underlying fundamental processes of electron acceleration and magnetic reconnection involved in impulsive phenomena such as flares and coronal mass ejections (CMEs).

At metric wavelengths, solar type II, type III, and type IV radio bursts are often associated with impulsive events [161, 194, 78]. A detailed description of the burst characteristics and their underlying emission mechanisms is presented in Section 1.4. Type III bursts are transient bursts known for their high rates of frequency drift, believed to be associated with electron beams traveling through plasma with a density gradient. Group type IIIs and complex type-III-like fast-drift bursts that occur with coronal mass ejections (CMEs) have been claimed to originate variously from shock-accelerated electrons, unspecified "shock-associated" acceleration, or acceleration directly from the flare site [27, 105, 54, 155, 81]. This uncertainty may be resolved with recently available high spatial, spectral, and temporal resolution imaging of type III bursts, which provide key information about reconnection sites and contribute to our understanding of particle acceleration [32, 33, 133].

Metric-decametric bursts of type IV present themselves as broadband continuum emission in the dynamic spectrum, sometimes accompanied by fine structures like Zebra patterns, fiber bursts or broadband quasi-periodic pulsations [168]. Observations of moving type IV bursts associated with CMEs are rare–only 5% of CMEs exhibit type IVm bursts according to Gergely [73]. To our knowledge only 4 studies have so far reported moving type IV bursts in solar cycle 24 [179, 8, 131, 182]. Although immense progress has been made in understanding these bursts over the decades, the underlying mechanisms responsible for their production remain uncertain. Bastian et al. [11] and Maia et al. [113] could clinch the case for gyrosynchrotron emission in their events because smooth continuum emission could be seen throughout the associated CME loops, although it should be noted that some areas of gyrosynchrotron emission in the interior of the CMEs were far brighter. Only this brighter interior emission, coincident with the core of the CME, could be seen in the moving type IV events reported by Tun & Vourlidas [179] and Bain et al. [8], but both argued for a gyrosynchrotron interpretation due to the smoothness of the emission in frequency and time. However, a recent study by Morosan et al. [131] found that a coherent emission mechanism (either plasma or electron cyclotron maser emission) was responsible for the moving type IV burst in their event, while a stationary component during an earlier time in the burst was found to be consistent with gyrosynchrotron emission [29]. Therefore, it seems clear that some type IV and IVm continuum may be due to either gyrosynchrotron emission or a coherent mechanism or some combination [69, 131, 182]. Given these alternatives, some effort is required to investigate the relative likelihood of gyrosynchrotron emission as the cause of a given source. The recent advances in radio imaging-spectroscopy can provide the spatial information required for investigating the emission mechanism while also supplying the spectral diagnostics that can be exploited when gyrosynchrotron emission is favored. In any case, the rare observations of type IVm associated with CMEs are a powerful tool to investigate the densities and magnetic field strength in these energetic events.

In recent years, the new instruments that have come online that, while not solar-dedicated, nevertheless can be used for occasional imaging spectroscopy of the Sun at high temporal, spectral, and spatial resolution. Two in particular have helped to renew interest in metric and decametric studies of the radio Sun, the Low Frequency Array [181, LOFAR] and the Murchison Widefield Array [175, MWA]. LOFAR operates in two frequency ranges, 10–90 MHz and 110–250 MHz, while the Murchison Widefield Array (MWA) observes between 80–300 MHz. Both provide imaging spectroscopy of the radio Sun at high temporal resolution on an occasional basis. Several studies have been published in recent years that take advantage of these novel instruments to investigate both active and quiet Sun [116, 153, 166, 165, 211, 119, 129, 148].

In this chapter we report the first analysis of solar data from the OVRO-LWA, located near Big Pine, CA. At the time of observation, the array consisted of 288 dual-polarization dipole antennas which are optimized to minimize side-lobes; 256 residing in a 200 m diameter core, and the remaining 32 extending to maximum baselines of ≈ 1.6 km [4, 58], allowing it to spatially resolve the Sun in the frequency range 27–85 MHz with high spectral resolution. The spatial resolution is about $8.5 arcmin$ at 80 MHz. The total bandwidth of the array covers this frequency range with 22 subbands, each comprising 109 24-kHz-wide channels at an operational cadence of either 9 or 13 s, although a 1-s snapshot mode is also available. The array uses the 512-input LEDA correlator [101], which allows imaging the whole visible hemisphere at all times. Upon completion of an upgrade now underway, it will consist of 352 elements spanning a maximum baseline of $\approx$2.6 km, with a correspondingly improved spatial resolution of $5 arcmin$ at 80 MHz. The upgrade includes a dedicated solar mode with full-spectrum imaging at 0.1-s cadence and measurement of the flux density dynamic spectrum at 1-ms time resolution.

These "first-light" solar data were recorded during commissioning in 2015 to explore the capabilities of the array for solar radio observations, both at quiet times and during energetic events. We present our investigation of a complex event consisting of multiple bursts and sources, which occurred in association with a CME and a GOES soft X-ray (SXR) class M2.1 flare. In Section 2.2 we present the observations obtained from OVRO-LWA and the supplementary observations taken from other instruments. In Section 2.3 we investigate the classification of each of the major burst sources and analyze the various features to identify the emission mechanism. We find that one of the sources, a moving type IV (IVm) is due to gyrosynchrotron emission and use spectral fitting to estimate the evolving physical parameters corresponding to the core of the CME. In Section 2.4 we discuss our results and conclude with a discussion of what solar research will be possible with the instrument upgrade now underway.

2.2 Observations

A GOES SXR class M2.1 flare and associated CME were observed on 2015 September 20 (SOL2015-09-20) in NOAA active region 12415, located at heliographic coordinates S19W52, near the south-west limb. The flare onset was at 17:32 UT (Figure 2.1) and the SXR peak was reached at 18:03 UT, accompanied by a rather complex radio event recorded by OVRO-LWA also reaching peak emission around the same time as the SXR flux. The SXR flux returned to GOES-class C1 (background) level several hours later, around 21:00 UT. The first signature of the white light CME (WL-CME) was detected at 18:12 UT in the field of view of the C2 coronagraph of the Large Angle and Spectrometric COronagraph [22, LASCO] instrument onboard the Solar and Heliospheric Observatory [50, SOHO].

The event recorded by OVRO-LWA coincided with the commissioning observations for expansion of the array to the current maximum baseline of $\approx$1.6 km.

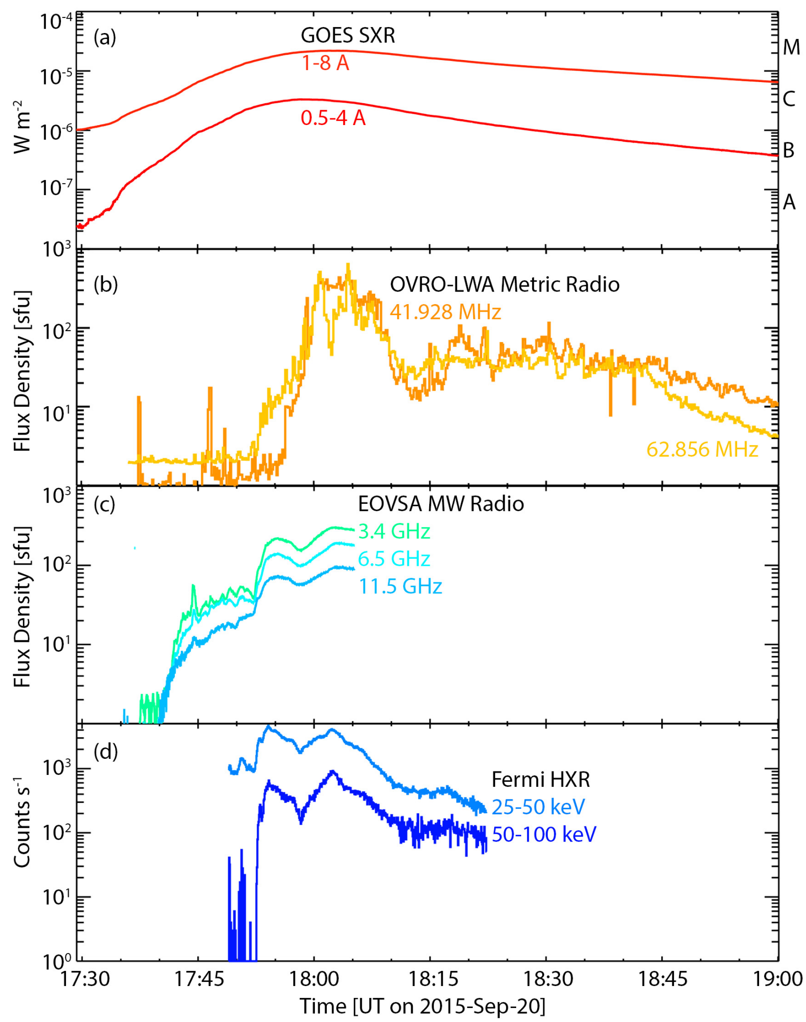

Figure 2.1 Radio and X-ray light curves showing the temporal development of the M2.1 solar flare on 2015 September 20. a) GOES SXR. b) OVRO-LWA metric flux density at two representative frequencies. c) EOVSA flux density at three representative frequencies. d) Fermi/GBM HXR count rate accumulated over two nonthermal energy ranges.

Source: [34].

This early stage of operations had three major effects on the data collected: 1) the observed bandwidth was reduced to a little less than 40% of the total available; 2)the baseline frequencies were offset by 150 kHz, and 3) adequate understanding of the circular polarization calibration was not yet available, hence we do not attempt to use circular polarization information for the event. The first effect reduced the bandwidth to two available windows between 41–55 MHz and 61–69 MHz as opposed to the full bandwidth capability of 27–85 MHz and the second resulted in an offset in the position of all sources present in the sky, which we corrected. The third problem limits us to consideration of total intensity only. None of the above-mentioned drawbacks had any impact on the spectral and temporal resolution of the instrument during the event.

Observations from the LASCO C2 instrument covering 2.2–6 $R_\odot$ (distance from the solar disk center) were used to get context of the radio source with respect to the WL-CME, and also to provide electron density diagnostics. We also use data from the WAVES [19] radio spectrograph onboard the WIND spacecraft, where spectra from both RAD1 and RAD2 receivers was obtained. The frequency ranges between 20–1040 kHz and 1.075–13.825 MHz are covered by RAD1 and RAD2 respectively; the Expanded Owens Valley Solar Array [71, EOVSA] for microwave radio spectra that covers 1–18 GHz; and the US Air Force Radio Solar Telescope Network (RSTN) spanning between 25–180 MHz for meter-wave spectra to analyze the event and provide context among multiple wavelengths.

2.2.1 Data Collection and Processing for OVRO-LWA

The flare-CME event was analyzed over a period of 120 min with images of 9-s cadence. Images during this period were inspected to identify distinct sources, understand their spatial configuration and describe their temporal behavior. Additional spectral analysis was done for certain times when the complexity of the burst was

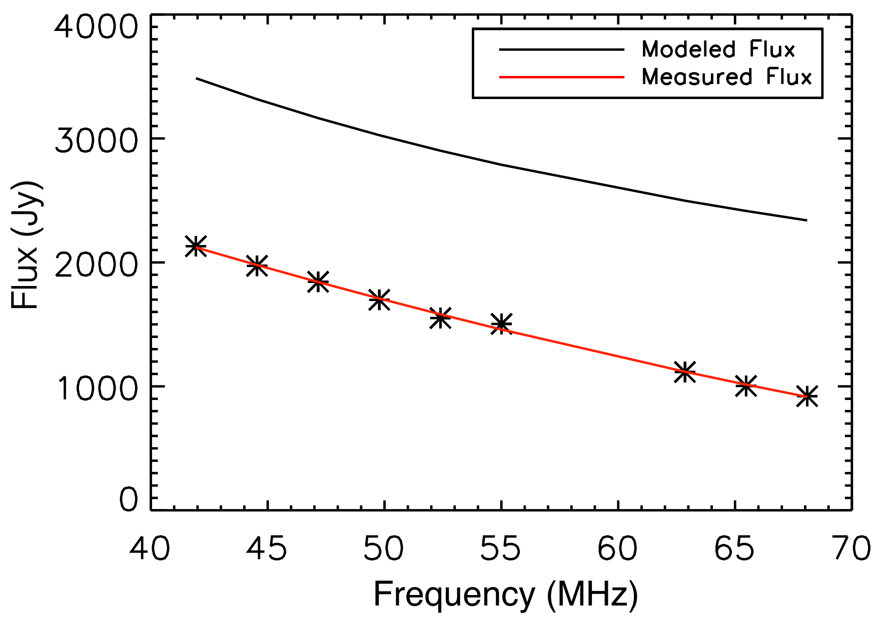

Figure 2.2 Measured and modeled flux density of radio galaxy Virgo A. The well-established flux density model for low frequencies is taken from Vinyaikin et al. [187] (solid line). The flux for Virgo A (asterisks) was measured at our 9-s cadence, averaged over a few minutes and fit to a quadratic polynomial shown by the red line.

Source: [34].

at minimum, to provide information on the emission mechanism of the burst. Since OVRO-LWA observes the whole sky at all times, to obtain the images for our analysis of the solar radio bursts, we first convert the data from the native output of the correlator to the Measurement Set (MS) format [122] using an in-house tool called "dada2ms". The data are further processed in the following 4 steps:

1. *Flagging and calibration*: Once the Measurement Sets are corrected for the aforementioned frequency offset, adopting the strategy outlined in Anderson et al. [5], all identified bad antennas, channels and baselines are flagged and the data are calibrated using bright sources in the sky, e.g., Cyg A and Cas A. To minimize the presence of side-lobes, the bright sources are later removed from the all-sky maps (using a process known as "peeling") [127, 57].

2. *Shifting the phase center* of the sky maps to the nominal position of the center of the Sun from the originally Zenith-centered calibrated maps.

3. *Cleaning* the sky maps and creating multi-frequency synthesis (MFS) FITS images using WSClean [137] for each subband. The available bandwidth during the time of the event consists of 9 subbands, each having 109 channels, 24 kHz wide, which are merged together to create 9 band-averaged MFS images at each time. All frequencies mentioned hereafter are the central frequencies of these subbands.

4. *Flux calibration and correction for position offsets* caused by the ionosphere and instrumental effects: The radio galaxy Virgo A happened to be within 15 degrees of the Sun. It is a strong source with a well-established flux density model for low frequencies [187] and a precisely known position. We use this source to calibrate solar flux density and position.

Figure 2.2 shows the measured, uncorrected flux density for Virgo A averaged over a few minutes, represented by asterisks fitted to a second-degree polynomial, along with the model flux density spectrum a factor of $\approx$2 higher. We use the model flux density and the polynomial fit to the measured flux of Virgo A, to obtain a flux factor as a function of frequency, which is then used to "bootstrap" the measured solar flux density to the corrected values. Flux correction for residual primary beam effects is also performed in this step.

Large scale fluctuations in the ionosphere can cause a refractive offset in position, which needs to be further corrected in order to measure the source centroid position with accuracy. Ionospheric refraction is greater at lower frequencies and falls quadratically with increasing frequency. It can be measured and corrected by referring to a nearby point source with a known position. As noted earlier, Virgo A is $\approx 15^\circ$ from the Sun and so, is well-placed for use in correcting for refraction offsets. The precisely known position of this source allows us to determine the offset in its observed position with respect to its true position as a function of frequency. We find a fairly small shift of $10''$–$30''$ in right ascension (RA) increasing from the lowest to highest frequencies, and a larger shift of $320''$–$160''$ in declination (DEC), which we correct. Temporal variations in the position of Virgo A were found to be within $\pm 10''$ and have been ignored. The measured offsets are indeed found to follow the expected quadratic pattern, which gives us confidence that the refraction due to the ionosphere has been successfully corrected.

Representative images of the Sun are shown in Figure 2.3 at 62.85 MHz for three different times during the event after the calibration, synthesis imaging, and offset correction process is complete. The solar grid is superimposed for scale along with a reference image from the Atmospheric Imaging Assembly (AIA) 171 Å channel onboard the Solar Dynamic Observatory [109, 15, SDO]. Each LWA image includes three contours representing 2%, 50% and 90% of the total brightness temperature T_b demonstrating the wide dynamic range of the instrument.

2.2.2 Event Overview

As shown in Figure 2.1, the time profiles at a wide range of wavelengths and energies are similar. The microwave flux density from EOVSA, which is due to gyrosynchrotron emission, was strongest at lower microwave frequencies (3.4 GHz) and shows nearly the same but weaker time profiles at higher frequencies. The

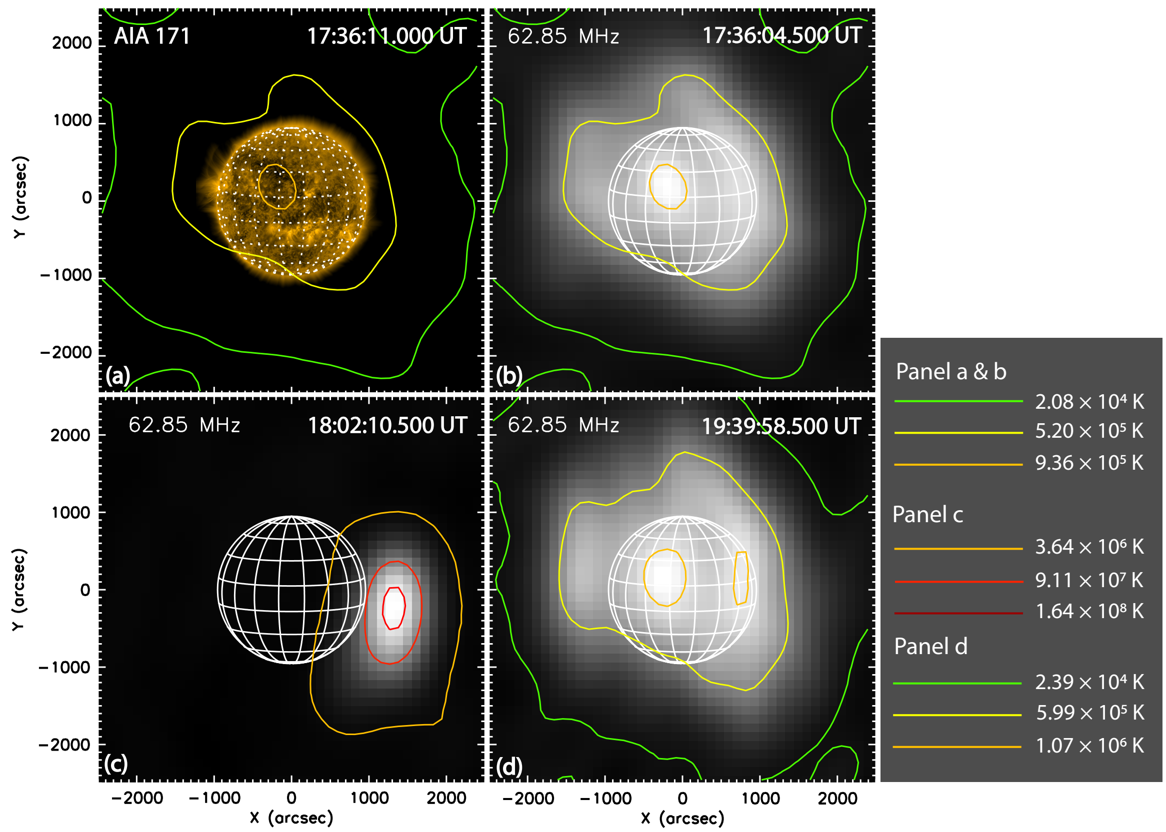

Figure 2.3 Processed images of the Sun at different times during the event to show the dynamic range of the instrument. a) AIA 171Å image overlaid with quiet-Sun contours from panel b for comparison. b) A representative quiet Sun image (gray scale) from a time before the event, with contour levels indicated in terms of T_b in the box on the right. These represent 2%, 50% and 90% of the maximum brightness temperature. c) Same as b, for a time near the peak of the burst. Now the 2%, 50% and 90% contours represent much higher T_b values. d) The quiet Sun after the event, similar to the pre-event image in panel b, although the west limb T_b is slightly elevated.

Source: [34].

dynamic spectrum from EOVSA is shown in Figure 2.4 up to 18:05 UT, when observations ended, compared with the OVRO-LWA dynamic spectrum over the same time period. The overall pattern of flux density variations in Figure 2.1b,c suggests three distinct episodes: i) a period of weak but growing emission in microwaves from 17:40–17:52 UT accompanied by sporadic type III bursts in LWA, ii) a moderate, smoothly varying peak in microwave from 17:52–17:58 UT characterized by increasing continuum emission in LWA, and iii) a second, slightly stronger, smoothly varying peak in microwaves from 17:58 UT onward, accompanied by a strong increase in emission in LWA. The emission mechanism in these widely separated frequency ranges is different, with the EOVSA emission being a smooth continuum due to incoherent gyrosynchrotron emission from flare-accelerated electrons [52] spiraling in a low-lying coronal magnetic field while the OVRO-LWA emission during this time is dominated by spiky, coherent plasma emission from instabilities associated with a population of continuously accelerated electrons much higher in the corona. Any similarity in flux density profiles is likely a reflection of the overall pattern of energy release in the event. The two episodes of enhanced activity in microwaves, peaking at 17:55 UT and again at 18:03 UT, are also seen in HXR emission by the Gamma-ray Burst Monitor aboard Fermi (Fermi/GBM; Figure 2.1d), but the microwave times are delayed 1–2 minutes relative to the peak times of nonthermal HXR emission, suggesting relatively strong trapping of the microwave-emitting electrons. Note that gyrosynchrotron microwave spectra typically peak between 5–10 GHz [86] while the peak microwave frequency for this event seems to extend below the lowest observed frequency in EOVSA (2.9 GHz) at the time. This suggests a relatively low magnetic field strength in the source, and hence a greater height for the emission, than is typical for microwave bursts.

We extract dynamic spectra from the WIND/WAVES and RSTN radio instruments, which cover frequencies both above and below the observing range of OVRO-LWA, for contextual understanding of the observed radio bursts. RAD1 and

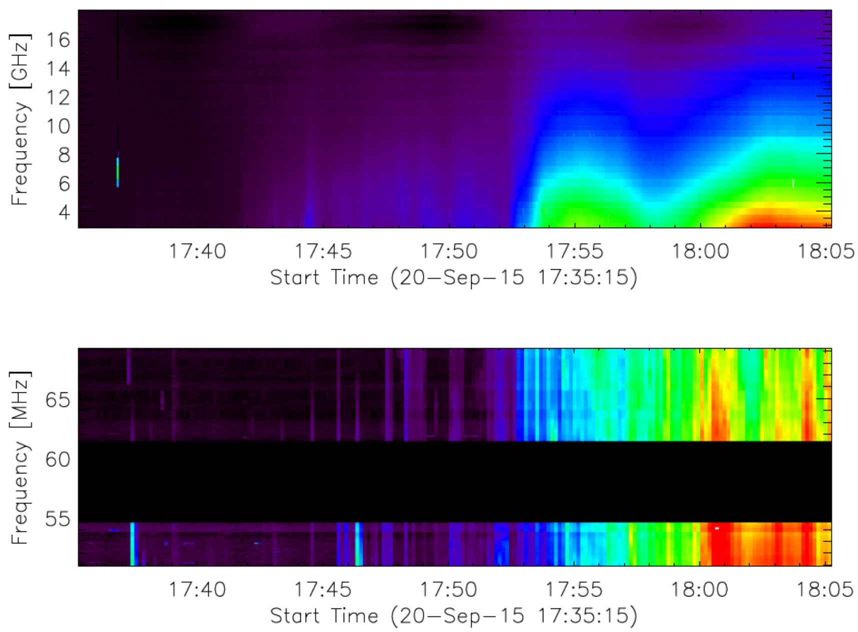

Figure 2.4 LWA (bottom) dynamic spectrum in context with the corresponding dynamic spectrum from EOVSA (top) obtained at some 2-orders-of-magnitude higher frequency in microwaves.

Source: [34].

RAD2 receiver bands from WAVES onboard the WIND spacecraft cover the frequency range between 20–1040 kHz and 1.075–13.825 MHz with 256 channels each and a bandwidth of 3 kHz and 20 kHz respectively. The RSTN spectrograph covers 25–180 MHz, overlapping with the OVRO-LWA range. Figure 2.5 shows a composite dynamic spectrum with the lower frequencies from WIND/WAVES RAD1 and RAD2, and the higher frequencies from RSTN. The available bands in OVRO-LWA, with their far higher signal to noise ratio, are inserted to replace the RSTN spectrum in those bands. The three vertical black lines mark times to be discussed in Subsection 2.3.3. The peak of radio emission occurs at a similar time as the soft X-ray peak at 18:03 UT and is associated with a dense group of type IIIs. Continuous emission is seen in the decay phase consistent with a type IV burst. There is also a signature of a type II burst at lower frequencies, seen in RSTN and extending into RAD2 frequencies (whose leading edge is marked by dashed-line in Figure 2.5). We searched for an OVRO-LWA counterpart by extrapolating the type II emission to higher frequencies and earlier times, but did not find any clear signature despite OVRO-LWA's high sensitivity. This suggests that the type-II-burst-emitting shock had not formed until later and at greater heights.

LASCO-C2 images with a 12-min cadence were obtained between 18:12–19:12 UT and processed to enhance the CME features using monthly background subtraction, median filtering, occulter masking and Normalized Radial Graded Filtering [130]. The upper row of panels in Figure 2.6 show LASCO-C2 images at four times during the event. In the first image at 18:00 UT, the CME had not yet reached above the C2 occulter at 2.2 $R_\odot$. Its first appearance was at 18:12 UT (see contours in the left column of Figure 2.9). A height-time plot of the CME leading edge and core is shown in Figure 2.7, which indicates a relatively constant velocity (1240 km s^{-1}) that extrapolates back to 1 $R_\odot$ around 17:57 UT. This suggests an association with the first of microwave and HXR peaks around 17:55 UT. No data were available for

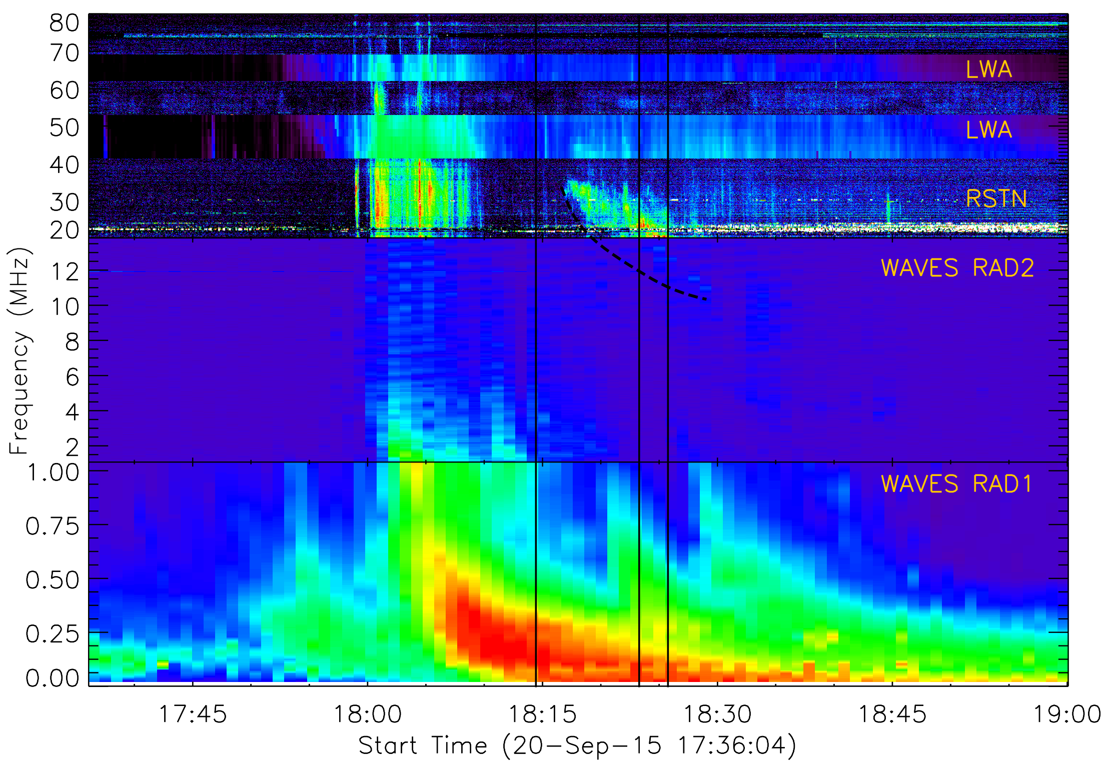

Figure 2.5 Composite dynamic spectrum from WIND/WAVES RAD1, RAD2, RSTN with an overlay from OVRO-LWA.

Source: [34].

this observation window from COR1 and COR2 coronagraphs onboard the STEREO satellites. The closest in time STEREO-A COR2 image was at 19:26 UT, and because the Earth–spacecraft angle was 170.6 degrees, its view was almost directly behind and provides little additional information about the plane of the CME.

2.3 Burst Identification and Analysis

2.3.1 Burst Identification

OVRO-LWA images of the Sun are created at each time in the nine available frequency-subbands to create a movie between 17:36-19:36 UT, beginning with the onset of the flare and ending with the decay phase (See movie in Figure 2.6). Upon carefully examining the complex event as seen by OVRO-LWA and LASCO-C2 (C2 hereafter) WL data, we identify distinct times and source-regions of interest (TOIs and SRs hereafter) based upon important changes in burst position and/or apparent motion. We use the term source-region (SR) and source interchangeably hereafter. Figure 2.6 gives an overview of the event with WL images as recorded by C2 in the top panels, and corresponding OVRO-LWA maps in the bottom panels. OVRO-LWA brightness temperature contours at 62.86 MHz (one of the higher frequencies available) are overlaid on the C2 maps. SRs 1, 2 and 3 are identified with white arrows at those times when each becomes dominant at 62.86 MHz. The identified SRs represent three different burst sources spatially distributed within the erupting region with possibly different underlying mechanisms. The order of appearance and dominance of burst emission in the SRs varies with frequency and time in a complicated manner due to their different spectral and temporal behavior. However, source 2, which is well aligned with the axis of the CME, shows an outward motion at least during some of the time, as described further below.

A concise description of the dominant sources during the TOIs is noted in Table 2.1. There are signatures of numerous distinct bursts in SR 1, lasting less than our 9-s

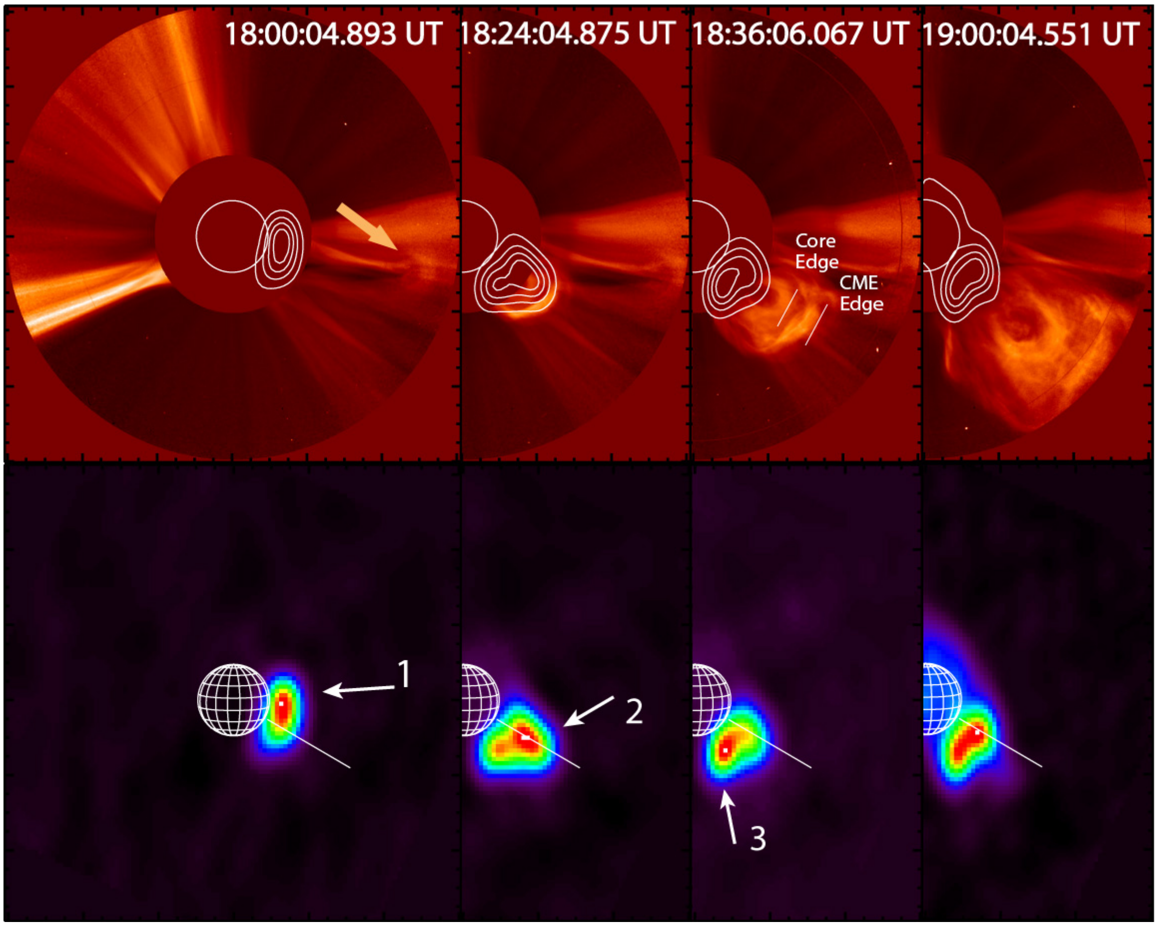

Figure 2.6 *Top row:* Evolution of the flare-CME event in WL recorded by LASCO-C2 at four selected times constrained by LASCO's 12-min cadence. The yellow arrow in the left panel points to a pre-existing CME discussed in the text. OVRO-LWA 20%, 40%, 60% and 80% brightness temperature contours are overlaid for reference. The third panel shows example locations of the leading edge of the CME and the core used for height-time analysis. *Bottom row:* OVRO-LWA maps at 62.86 MHz, at the corresponding times for comparison. White arrows mark three source-regions of interest (SRs) described in the text. The white lines mark the slit along which height-time measurements are made for Figure 2.7.

Source: [34].

cadence, observed first in lower frequencies and later over the whole band, immediately after the onset of the flare at 17:32 UT and continuing for about 15 minutes (associated with a slowly increasing, but weak level of activity in microwaves visible in Figure 2.4). Fairly continuous broadband emission, but fluctuating in brightness, comes mainly from SR 2 until a few minutes before the peak of the emission at ≈18:03 UT. Relatively stationary pulsations from SR 1 become dominant at lower frequencies during this peak time, while at higher frequencies emission from both SR 1 and 2 are comparable. Around 18:18 UT, SR 3 first appears. From 18:18–18:23 UT sources 1 and 3 fluctuate but SR 2 exhibits steady emission smoothly varying both in frequency and time and a distinct outward movement across the whole band, reaching as high as 3 $R_\odot$.

2.3.2 Burst Analysis

SR 1: The examination of the movie alongside the dynamic spectrum suggests that emission in SR 1 is likely associated with type III radio bursts. Several distinct type IIIs are observed in the dynamic spectrum between the onset and the peak time of the flare, and a dense group of type III bursts identified from the dynamic spectrum appeared from both SR 1 and 2 during the peak. The SR 1 burst location spatially aligns with the position angle of a previous, slow and narrow CME, first observed with C2 at 15:48 UT. The remnant structure of this previous CME is shown by the yellow arrow in Figure 2.6. The material from this previous CME has moved out to $\approx 5.38\ R_\odot$ by the time we observe type III activity in the region. One possible explanation for the existence of type III bursts at this location is that there may be some interaction between this pre-existing magnetic structure remnant from the earlier CME and the initial stages of the M2.1 flare. Alternatively, Reiner et al. [155] have shown that a class of hectometric type III bursts observed over an extended duration and temporally associated with decimetric and metric radio emission may

Table 2.1 Overview of the Event with Respect to the Identified Source Regions (SRs) at Different Times, and the Respective Features Observed

Time of interest (UT)	Dominating SR (Low $\nu < 55$ MHz)	Dominating SR. (High ν)	Dominant Features Observed
17:39–17:47	1	1	Sporadic short-duration bursts[a]
17:49–17:54	2	2	Continuous Emission
18:00–18:09	1	1,2	Stationary pulsations
18:18–18:23	1,2,3	2,3	Outward movement in 2

[a]Mainly type III bursts

Source: [34]

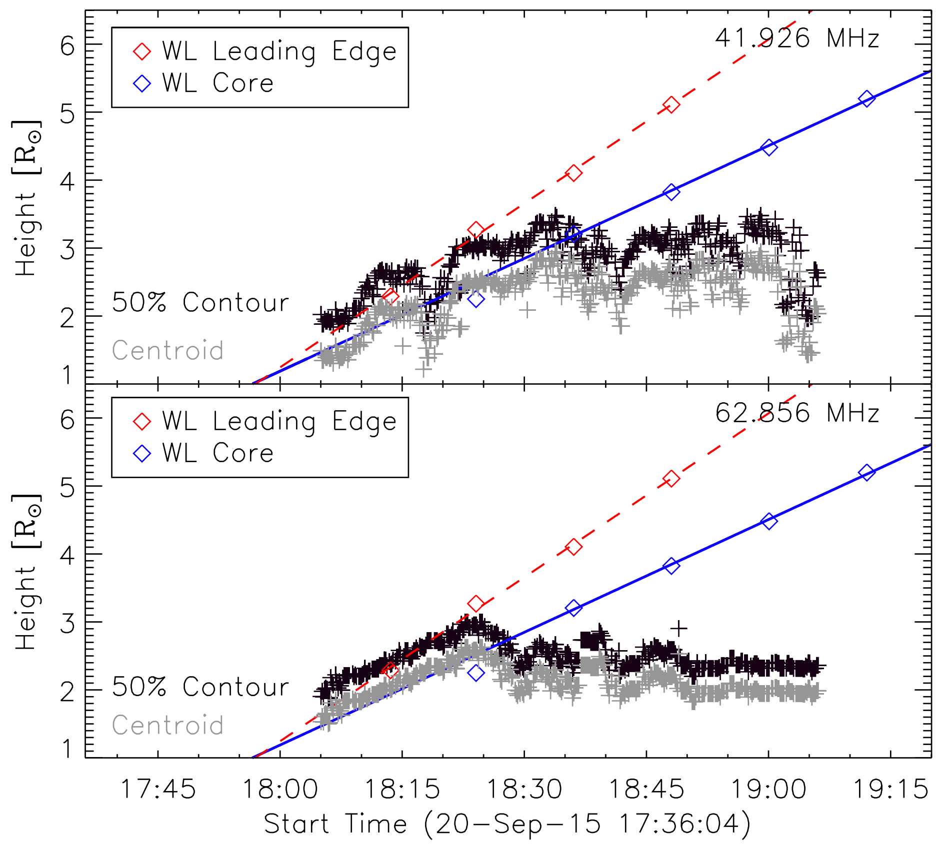

Figure 2.7 Composite height-time plot of the radio source SR 2 at two frequencies, 41.92 MHz (top) and 62.86 MHz (bottom) with WL CME leading edge (red) and Core (blue), overlaid. The black symbols mark the position of 50% contour of the radio source, and gray points show the source centroid estimated by subtracting the beam half-width.

Source: [34]

be produced by electron beams ejected primarily from the flare site itself. Such bursts are classified as complex type III bursts due to their complex intensity profiles.

SR 2: *Height-Time Analysis*: As mentioned above, it is in SR 2 that we observe a steady outward movement of the source. This motion is investigated in detail by performing a manual height-time analysis of the radio source at all the available frequencies to estimate the velocity of the source and then compare it with the speeds of the CME leading edge and the core. For the purpose of height-time analysis of the radio source, we chose a direction aligned with the observed outward motion (shown by the white lines in the bottom row of Figure 2.6), which is only slightly non-aligned with the direction of CME motion. To measure the outward motion of the radio source, we do not use the peak or centroid locations, both of which were affected by the intermittent brightenings of overlapping source SR 1, but rather we use the position of the apparently more stable 50% contours of SR 2 (the intersection of this contour with the axis line) at each time as a measure of this outward motion. The 50% contour height is shown by the black symbols in Figure 2.7 at two different frequencies. To obtain a rough proxy for the source centroid position, which cannot be directly measured due to the above-mentioned confusion with SR 1 and 3, we subtract the synthesized beam (point-spread-function) half-width at each frequency, under the assumption that the source is unresolved. In cases where the source is resolved, this proxy will slightly overestimate the height of the centroid, but it is sufficient for our purposes here. This proxy for the centroid position is plotted in Figure 2.7 as gray symbols. Heights of the outward moving leading edge and core of the WL CME are also measured in a similar manner (one example is shown in the third panel of the upper row of Figure 2.6). The positions are recorded where the outer edge of the core (blue diamonds in Figure 2.7) and the leading edge (red diamonds) intersect the axis at each time. The same points are plotted in both upper and lower panels of Figure 2.7. The blue core points are fit with a constant velocity (775 km s^{-1}).

The first point (at 18:24 UT) was excluded while performing this fit, since the height of the core at that time is uncertain due to its proximity to the occulter. The fit is extrapolated backward to highlight that the CME core velocity matches the gray radio centroid points quite well.

A smooth outward motion is evident at higher OVRO-LWA frequencies in Figure 2.7, while the lower frequencies show rather erratic changes, due to greater source confusion, although also having an outward-moving trend. Although an apparent motion is clear from the height-time plots, visible outward motion in the movie is most apparent only for a short of period of time between 18:18–18:23 UT when only SR 2 was visible and undisturbed by the other sources. Based on the outward motion of the source, along with its clear match to the WL CME core position and speed, we classify the SR 2 as a type IVm (moving type IV) source.

SR 3: SR 3 aligns well with the southern flank position of the CME, and the source becomes dominant during the decay phase of the radio event, while the source centroid over all observed frequencies appears to be spatially coincident. Plausible mechanisms may include stationary type IV plasma emission from particles accelerated in this southern flank region. However, due to the lack of stereoscopic observations and polarization information from the OVRO-LWA, any additional conjecture regarding the morphology and underlying mechanism is not justified.

2.3.3 Moving Type IV Emission Mechanism

Following from Section 2.1, a number of studies [11, 113, 179, 8] have shown that continuum emission associated with CMEs can be due to gyrosynchrotron radiation. While Maia et al. [113] and Bastian et al. [11] were able to rule out plasma emission owing to the well defined radio–CME loop morphology that was spatially coincident over multiple frequencies, we lack that advantage since our source is not spatially resolved. Therefore, we must rely on other arguments similar to those by

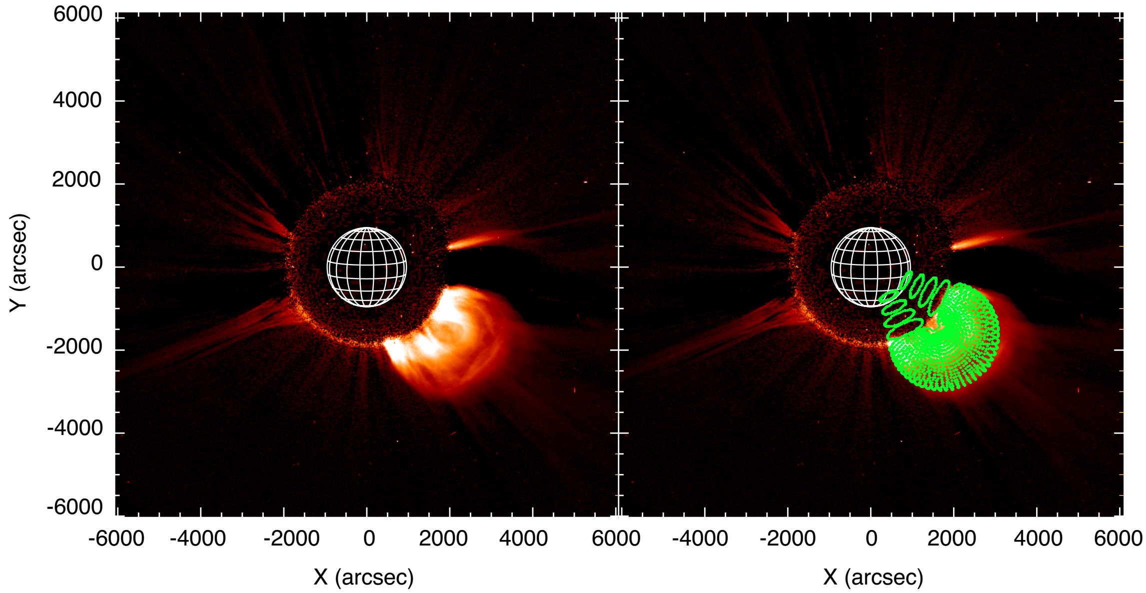

Figure 2.8 *Left*: Reference image of the C2 WL CME at 18:36 UT used to create a CME model by the GCS reconstruction method. *Right*: Wire-frame CME in green. *Source:* [34]

Tun & Vourlidas [179] and Bain et al. [8]. The fact that the emission we observe varies smoothly over frequency and time for the duration of the visible outward motion, together with the rather large height of SR 2 ($> 2.5R_\odot$ at 65 MHz), suggests gyrosynchrotron emission for our event as well. To investigate further whether plasma emission can be ruled out, we examine the density using constraints from the LASCO-C2 observations. It is noted that the limited resolution along with the source confusion restricts us to only average over the inhomogeneous structure. Any physical parameters derived further are only used as representative values and apply to the source only in an averaged–sense.

We start by performing a graduated cylindrical shell (GCS) reconstruction of the CME [174]. The model assumes a self-similar expansion of the CME, integrated with a flux-rope morphology. We note here that due to the lack of simultaneous stereoscopic observations we get only one viewpoint from LASCO, so we lack a firm measure of the plane-of-the-sky angle of the CME, on which the density depends. However, fitting a single point of view can still offer a useful constraint on the density. The free parameters in the model such as CME height, tilt-angle of the source-region neutral line, angular width and aspect ratio are used to create a wire-frame model for the CME, shown in Figure 2.8. For plane-of-the-sky angle, we take the initial values of the heliographic coordinates for the source region from SDO/AIA measurements, which are then adjusted to match the observations. Such adjustments are sometimes necessary given the fact that CME deflections are commonly observed due to several influencing factors like background coronal magnetic topology, streamers, and fast solar wind from coronal holes [111, 42]. The model is then used to generate a synthetic brightness image of the CME using a ray-tracing renderer, based on Thompson scattering equations. This process is performed for C2 images recorded at 18:24 UT and 18:36 UT, and the density estimates for the leading edge of the CME are then adjusted to give synthetic brightness that matches with the observed brightness.

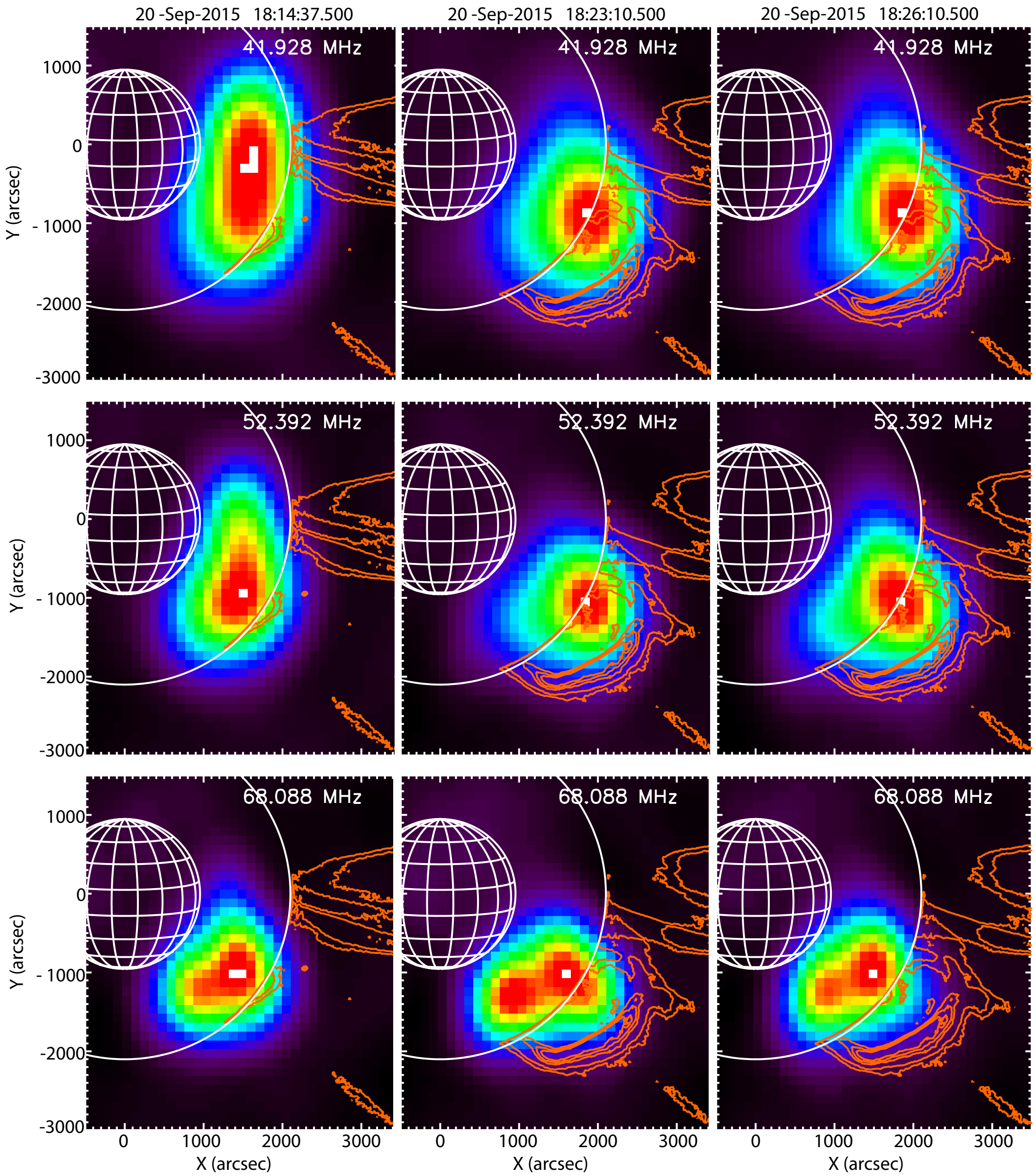

Figure 2.9 Overview of the outward moving radio source in SR 2 as seen by OVRO-LWA. WL CME contours from C2 are overlaid in orange to show the relative movement of the source with respect to the CME. Time is increasing as we move from left to right and frequency increases as we move from top to bottom. The C2 contours in column 2 and 3 are the same (taken at 18:24 UT), the only frame closest in time with respect to the OVRO-LWA images. C2 contours in column 1 are taken at 18:12 UT. The white solid circle marks the C2 occulter at 2.2 $R_{\odot}$.

Source: [34]

Although the leading edge is a convenient place to use for scaling the GCS model, the scaled model is interpreted as applying to the entire CME including its core (represented by the inner fold of the croissant-shape) where the moving radio source is located.

We exploit the fact that the core and the leading edge of the CME are comparable in brightness (within a factor of 2) to get a proxy for density in the core. Using this process we obtain the value of density for the leading edge of the CME at 18:24 UT to be $N_e \approx 2.2 \times 10^6\,\mathrm{cm}^{-3}$ corresponding to a plasma frequency ν_p of 13.32 MHz. The density obtained at 18:36 UT is $\approx 6.2 \times 10^5\,\mathrm{cm}^{-3}$ corresponding to $\nu_p = 7.07$ MHz. We use these estimates when discussing our spectral fitting results below.

Spectral Fitting: Fast gyrosynchrotron codes [61] are used to calculate the gyrosynchrotron emission based on a homogeneous source, which serves as the basis for performing spectral fitting at three different times (shown by vertical black lines in Figure 2.5) during the observed outward movement of the source, to estimate its evolving physical conditions. We chose times when there is a clear dominance of the source emission in SR 2 such that it can be clearly separated from bursts in SR 1 and 3 at most of the available frequencies. Figure 2.9 shows an overview of the outward moving source at three different frequencies and the chosen times, with the WL CME contours from C2 overlaid (orange) for reference. The white solid line marks the C2 occulter. Note that the C2 contours in columns 2 and 3 in the figure are the same (taken at 18:24 UT), since that is the frame closest in time to the OVRO-LWA images. C2 contours in column 1 are taken at 18:12 UT. The 50% contours of the source are then used as a measure of the convolved source size. We further deconvolve the source using the synthesized beam, to obtain an estimate of the source area [197]. As mentioned above, we average over an inhomogeneous source while estimating the physical conditions in the region. Consequently, we also assume

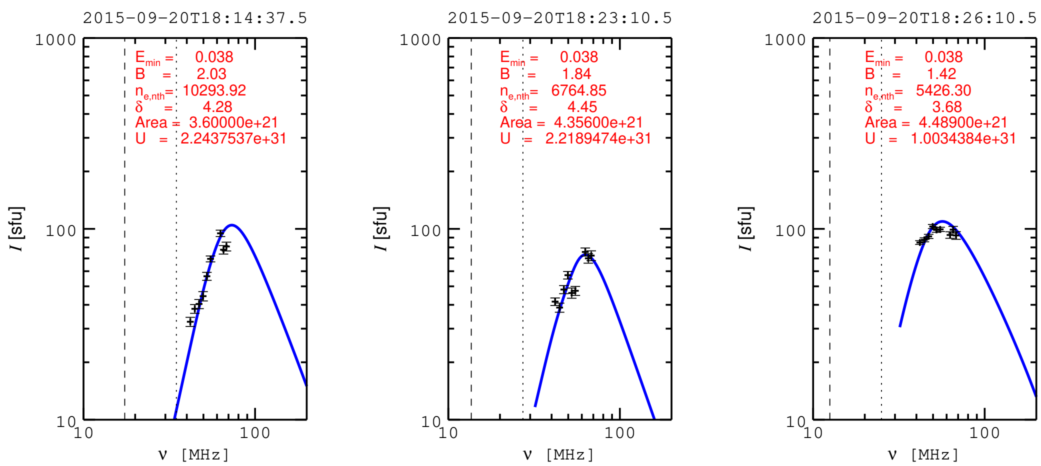

Figure 2.10 Spectral fits for the moving source in SR 2 at three times during the observed outward motion. From the ambient density used in the fits, the dashed and dotted vertical lines show the corresponding plasma frequency, ν_p and its second harmonic, $2\nu_p$ respectively at each time, relative to the observed emission.

Source: [34]

an isotropic electron distribution for the spectral fits. An extrapolation of the density estimates made using the GCS reconstruction and the source area are fed into the codes and the free parameters viz., $E_{\min}$, the minimum energy of the electrons in MeV, B, the magnetic field strength in G, $n_{e,\mathrm{nth}}$, the non-thermal electron density in cm^{-3}, and δ the power-law index are adjusted to match the observed spectra. Spectral fits for these times are given in Figure 2.10, with text in each panel giving the fit parameters, $E_{\min}$, B, $n_{e,\mathrm{nth}}$, δ, source area and U, where U is the magnetic energy density in erg cm^{-3}. The dashed and dotted vertical lines show the plasma frequency, ν_p and its second harmonic, $2\nu_p$ respectively at each time. These are slightly higher than, but close to the values we determined from the GCS fitting of the CME brightness. The spectral peaks are well above these plasma-frequency limits, further supporting the interpretation that the emission is due to the gyrosynchrotron mechanism. The results of the fits suggest that both accelerated electron density and magnetic field strength decline as the source expands outward, while the power-law index of the electrons hardens.

2.4 Discussions

This study presents first-light observations recorded by the OVRO-LWA of a flare and CME associated with a rather complex event at metric wavelengths. The observations were made during the first 24 h of commissioning observations for the expansion of the array, which compromised the frequency coverage and polarization capability, but nevertheless provided sufficient imaging spectroscopy to allow new insights into the rarely observed moving type IV (type IVm) phenomenon. A detailed analysis of the event is performed to characterize the multiple burst types observed and isolate the times when the emission was dominated by the moving source. We examined the relationship of the radio emission to a WL CME observed with the LASCO-C2 instrument, with context radio data from RAD1 and RAD2 receivers on board the

WIND spacecraft, RSTN and EOVSA. We identify three different source-regions of interest in the complex radio event.

1. SR 1 appears to align well with a region associated with a previous CME, observed at 15:48 UT. The type IIIs observed in this region during the peak phase of the flare may have resulted from turbulent interaction between the flare and some pre-existing magnetic structure from the earlier CME.

2. The broadband continuum emission in SR2 is classified as a moving type IVm burst. There exists a clear agreement between the outward movement of the source centroid in SR 2 and the corresponding movement of the WL CME core that can be seen on comparing the OVRO-LWA and LASCO height-time plots. The velocity of the CME leading edge from CME catalogues (maintained by the Coordinated Data Analysis Workshops (CDAW) Data Center) is given to be 1240 km/s. The position of the radio source from the height-time plots of OVRO-LWA suggests a lower velocity of $\approx$775 km s^{-1}, appropriate to the expected lower speed of the CME core. We further perform a GCS reconstruction of the CME to constrain its density in the volume. The corresponding plasma frequency is somewhat lower than the frequency of the observed emission, but given the uncertainties due to such issues as density inhomogeneity, angle of the CME to the plane of the sky, and line-of-sight depth, we cannot completely rule out the possibility of plasma emission as the underlying mechanism based on density alone. However, the smooth variation of SR2 in frequency and time strongly argue for gyrosynchrotron emission as the preferred mechanism. Under this assumption, we fit gyrosynchrotron spectra to the observations to obtain estimates of the physical parameters in the burst as the source evolves. The EOVSA dynamic spectrum suggests a reservoir of microwave-emitting electrons at an unusually large height early in the event, which could potentially serve as a source of particles escaping into the CME core region.

   There have only been a few studies that attempted to estimate the physical parameters of the plasma from type IV bursts using imaging-spectroscopy, most of them reporting observations at higher frequencies [11, 113, 179, 8, 129]. See the summary compiled by Mondal et al. [129], their table 3. The estimates for the magnetic field vary widely, with several reporting $B \approx 10$ G at similar heights compared to our lower value of order 1–2 G. Only the Bastian et al. [11] measurements are this low. This variability may be real, and simply reflect different conditions in different events. Additionally, Bastian et al. [11] and Maia et al. [113] report these values in radio–CME loops while the event observed in the current study and the ones reported by Tun & Vourlidas [179] and Bain et al. [8] are associated with the core of the CME. Conversely, power-law index, δ, is found in a narrow range of 3.5–5 in the previous studies, and our range of 3.7–4.5 is no exception. The nonthermal density, $n_{e,\mathrm{nth}}$ is particularly variable in these studies, ranging from 2×10^2–2×10^6 cm^{-3}, but this depends greatly on the value of $E_{\min}$ used for the estimate. Our values of 5000–10000 cm^{-3} are well in line with these.

3. Although there is a signature of a type II burst at lower frequencies observed in RSTN and WAVES Rad2 during the period of the outward motion, no such feature is visible in the OVRO-LWA spectrum at the earlier time expected by extrapolation to higher frequencies. It is interesting that the frequency range of type II emission seen in the RSTN data, drifting from 35 to 20 MHz over this time, closely matches the 2nd harmonic plasma frequency corresponding to both our CME leading-edge density estimate (26.6 MHz at 18:24 UT) and the thermal density used in our gyrosynchrotron fits (dotted lines in Figure 2.10). If we had had the full frequency-coverage for this event that OVRO-LWA is capable of, we would have been able to image both the gyrosynchrotron and type II emission simultaneously.

4. The continuous but time-variable broadband emission observed during the decay phase of the flare, associated largely with SR 3, shows a spatial alignment with the CME southern flank position. Plasma emission from particles associated with the flank of the CME is a plausible explanation. The CME flank is the location of shocks causing metric type II bursts in some models [37], but again we find no clear type II spectral feature in the OVRO-LWA data. Recent studies have also shown evidence of "herringbones" observed at the CME flanks [132], although the high cadence for this observation does not allow us to see any fine structures that may be present in the dynamic spectrum. Alternatively, this continuum source may be due to shock particles accelerated elsewhere and transported to SR 3.

CHAPTER 3

SIGNATURES OF TYPE III SOLAR RADIO BURSTS FROM NANOFLARES: MODELING

3.1 Introduction and Motivation

Understanding the physics of the heating of the solar corona to several million K, three orders of magnitude higher than the observed surface temperature, is a challenge that has stirred solar research for decades. Section 1.1 discuses the plausible mechanisms that may be responsible for this comprehensive phenomenon. Moving from large-scale transient bursts discussed in Chapter 2, this Chapter discusses small-scale bursts in the corona, and the associated radio emission.

Following from Parker's [141] theory, nanoflares are believed to be ubiquitous in the solar atmosphere. However, a major challenge we face is the lack of direct detection of individual nanoflares, due in part to their small amplitude and in part to the confusion from line-of-sight overlap of the optically-thin structures. Therefore, the existence and properties of nanoflares must be inferred from their collective effects. A variety of different methods have been used [100].

During a nanoflare life-cycle, the EUV emission from the heating phase is much less than that from the slower cooling phase [20]. This property of nanoflares leaves a unique signature in multi-wavelength observations. As the plasma cools, the loop appears first in a hot channel, subsequently showing up in cooler channels which, in turn, reach their peak intensities with some time delay. The powerful technique developed by Viall & Klimchuk [183] can identify cooling patterns in large ensembles of loops by detecting even the minutest variability in light curves. They use high-cadence observations from the Atmospheric Imaging Assembly onboard the Solar Dynamic Observatory [15, 109, SDO/AIA] spacecraft to measure the time-lag between two coronal channels. This is accomplished by computing the cross correlation of the light curves with different amounts of imposed temporal offset and determining which offset maximizes the correlation [see [183, 185]]. The technique not only detects time lags that can be identified by eye in observationally distinct loops, but also works well when there are countless overlapping coronal strands in observations of the diffuse corona, where the time lags are not obvious to the eye. Viall & Klimchuk [184] simulated the composite emission from 10,000 strands heated randomly by nanoflares, as expected in a real solar observation. The light curves exhibit only small fluctuations, yet the time-lag technique correctly identifies the cooling that is known to be present in the simulations.

Full-sized flares are extremely efficient at accelerating particles to high energy. Whether this is also true of nanoflares is unknown [186]. A leading theory of particle acceleration involves collapsing plasmoids [51]. The theory predicts that the efficiency of acceleration depends on the magnetic field geometry - in particular, whether there is a strong guide field component [43]. Because nanoflares and flares have different geometries, determining whether particle acceleration occurs in nanoflares would be an important test of the theory. Instinctively, we turn to hard X-ray (HXR) observations to answer this question. Such observations place a rather low upper limit on the quantity of highly nonthermal electrons. However, large numbers of mildly nonthermal electrons are not ruled out in active regions, because their emission would be dominated by much brighter thermal emission in HXR rendering the nonthermal component undetectable. For quiet Sun, although the temperatures are low enough that no thermal emission is observed to dominate HXR energies, nonetheless, the lack of sensitivity of the current instruments does not place meaningful limits on the mildly energetic particles [90, 89, 94]. Therefore, understanding particle acceleration from nanoflares requires a different approach.

Radio emission on the Sun is not constrained by these limitations. Type III radio bursts (coronal and interplanetary) especially are an important tool for understanding

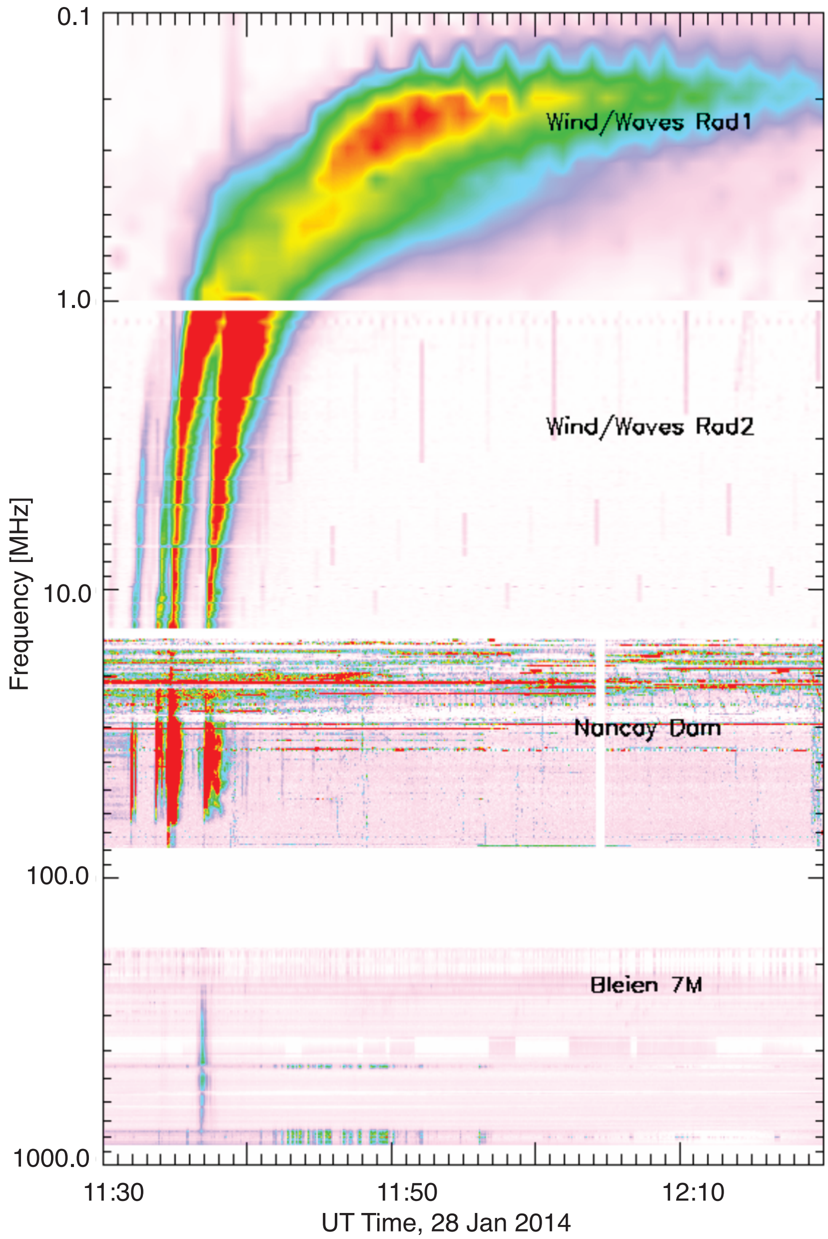

Figure 3.1 Composite dynamic spectrum from the Bleien telescope, the Nancay Decametre Array, WIND/WAVES RAD2, and RAD1 exhibiting traditional interplanetary type III radio bursts observed on January 28th, 2014 ([154], Figure 1). Reprinted with permission from Research in Astronomy and Astrophysics.

Source: [35].

accelerated electron beams given the characteristic frequency drift they show in the radio dynamic spectrum [198, 154, and references therein]. Figure 3.1 shows an example of traditional type III radio bursts as the particles move away from the Sun into interplanetary space. The dynamic spectrum combines data from the Bleien telescope covering the frequency range of 900–200 MHz [14], the Nancay Decametre Array [108] covering the range of 80–15 MHz, and the RAD1 and RAD2 receivers onboard the WIND spacecraft [19] covering 14–0.1 MHz. The frequency axis is inverted (decreasing upward) to give the impression of the electron beam propagating away from the Sun. As the electrons propagate outward along open field lines, they encounter decreasing density, and the emission is first detected at a higher frequency, followed by progressively lower frequencies. The time delay between the two defines the frequency drift rate of the burst. As shown in Section 1.4 'U' or 'J' shaped bursts exhibit frequency drifts in both directions.

While these traditional type IIIs are observed as individual bursts, in groups or sometimes as type III storms with hundreds of bursts occurring over a period of a few hours, the ever-present nanoflares may produce hundreds or thousands of bursts per second, which will not be identifiable as individual burst features in the dynamic spectrum. Rather, they may present themselves as a quasi-continuous 'radio haze.' The collective emission from these small bursts will not be as intense, and small but real fluctuations may be misinterpreted as mere noise. Moreover, the emission from these bursts coming from the closed corona will exhibit frequency drifts in both directions, similar to those seen in the stronger 'U' or 'J' bursts noted above.

In this study, we attempt to identify signatures of type III radio bursts that may be produced by nanoflares using the time-lag technique. Similar to correlating light curves in pairs of EUV channels, we will correlate light curves in pairs of radio frequencies. The radio drift of overlapping type III bursts shows up like the EUV cooling signature from overlapping magnetic strands, although on much shorter timescales. We construct a simple numerical model simulating emission produced by these type III bursts at different frequencies, which are then cross-correlated to measure time-lags for each frequency pair. We add increasing complexity to the model to more closely approximate the real corona, and at each step we evaluate the efficacy of the time-lag technique. Section 3.2 gives the detailed formalism for the loop model along with the methodology used to populate loops with nanoflares and simulate type III emission. We discuss our results in Section 3.3. The Appendix summarizes various additional factors that may affect the cross-correlation results. Subsequent studies are planned that apply these results to observations at these frequencies from the FIELDS experiment on Parker Solar Probe, the Very Large Array (VLA), and the Low-Frequency Array (LOFAR).

3.2 Modeling

3.2.1 Loop Model Formulation

The basic building block of our model is a symmetric loop in static equilibrium. Following Martens [117], we obtain solutions to the one-dimensional energy equation:

$$\frac{d}{ds}\left(\kappa_o T^{5/2}\frac{dT}{ds}\right) + Q - P_o^2 \chi_o T^{-(2+\gamma)} = 0 \tag{3.1}$$

where s is the spatial coordinate along the loop, $\kappa_o(= 1.1 \times 10^{-6}$ erg cm^{-1} s^{-1} K$^{-7/2})$ is the coefficient of thermal conductivity, Q is the volumetric heating rate, P_o is the gas pressure, taken to be constant along the loop due to the large gravitational scale height, and $\chi_o(=10^{12.41})$ & $\gamma(= 0.5)$ are parameters of the optically-thin radiative loss function in c.g.s. units. The heating function is taken to have a power-law dependence on pressure and temperature:

$$Q = HP_o^{\beta}T^{\alpha} \tag{3.2}$$

which is further reduced to

$$Q = H \tag{3.3}$$

assuming $\alpha = \beta = 0$ for a uniformly heated loop, where H is a constant of proportionality.

Although nanoflare heating is inherently impulsive, we believe it is reasonable to assume steady heating and static equilibrium for this initial evaluation of the feasibility of detecting overlapping type III bursts. Furthermore, nanoflares are believed to recur on individual field lines with a range of repetition frequencies [100, and references therein]. High-frequency nanoflares are effectively similar to steady heating, and loops heated by low-frequency nanoflares spend much of their time in a phase that is not greatly different from static equilibrium conditions.

Static equilibrium loops obey well-known scaling laws. With uniform heating, we have [117, equations 28 & 30]:

$$P_o L = T_a^3 \left(\frac{\kappa_o}{\chi_o}\right)^{1/2} \frac{\sqrt{2}}{5} B\left(\frac{6}{5}, \frac{1}{2}\right) \tag{3.4}$$

and

$$Q \approx \frac{1}{2} \kappa_o \frac{T_a^{7/2}}{L} \tag{3.5}$$

where L is the loop half-length, T_a is the temperature at loop apex, and B is the beta function.

Magnetic strands become entangled and braided as they are churned by chaotic photospheric motions. One promising idea is that nanoflares occur when the angle between adjacent misaligned strands reaches a critical value. As discussed in Mandrini et al. [115], this leads to a volumetric heating rate that scales with the loop length according to $Q = cL^{-3}$, where c is a constant. Adopting this dependence in the scaling laws above, and using the IDL routine BETALOOP.PRO developed by Martens [117], we can construct density and temperature profiles for loops with a variety of different lengths. An example density profile (electron density, n, vs. distance, s, along the loop) is shown in Figure 3.2a. As is characteristic of all loops, the gradients are shallow in the corona and steep in the transition region (TR) near the base. The temperature profile has these same properties, being essentially the inverse of the density profile due to the constant pressure.

3.2.2 Type III Logistics

As already noted, a beam of energetic electrons will generate radio emission at the local plasma frequency, $\nu_p \propto n^{1/2}$. This involves complex nonlinear interactions among the ambient ions or ion-acoustic waves and Langmuir waves that are generated by the beam. Detailed simulations of these processes have been performed in the context of the magnetically open corona and solar wind [103, 149, 153]. We do not attempt that here. Rather, we assume that the type III emission from a given location turns on, maintains a constant brightness, and turns off during the time that the beam is passing that spot. How the brightness may depend on parameters such as the density and energy of the beam, the ambient density, or the strength of the magnetic field are largely unknown [though see [169, 173, 102]]. We therefore assume that the emissivity (emission rate per unit volume) is the same for all events and all loop positions. This approach is consistent with our goal of demonstrating the feasibility of the technique in this initial study.

Radio spectral observations usually sample the emission in frequency bins, or channels, of equal size, $\Delta\nu$. We do the same when generating synthetic spectra from our models. Because density varies along the loop, each frequency bin corresponds to a small range of densities, Δn, which in turn corresponds to a finite section of the loop, Δs, as shown schematically in Figure 3.2d. We refer to this as a volume element, under the assumption of constant cross-sectional area [96].

Depending on the beam duration and hence the beam length, volume elements may be partially or fully filled by the beam. Longer elements near the apex tend to be partially filled, while shorter elements in the lower legs tend to be fully filled. We assign an intensity to frequency ν_i that is proportional to either the beam length L_b or the length of the corresponding volume element Δs_i for elements that are longer and shorter than the beam, respectively. Elements are centered on s_i where the local plasma frequency is ν_i. We also take into account the finite time required for the front and back of the beam to traverse the element; the light curve at a given frequency ramps up linearly as the beam enters the element, has a flat section, and ramps down linearly as the beam exits. The frequency bin size $\Delta\nu_i$ is the same for all frequency bins (all i).

Note that for a sufficiently long beam length L_b, such that all volume elements Δs_i along the loop are shorter than L_b, the intensity at all frequencies ν_i will be directly proportional to their respective volume elements Δs_i.

The size of a volume element and its associated intensity vary inversely with the local density gradient, as shown in Appendix A. Gradients are very small near the loop apex and increase steadily down the legs, becoming very large near the footpoints. Consequently, the intensity is a strong function of frequency (Figure 3.2c). Lower frequencies come from high in the loop and are bright, while higher frequencies come from low in the loop and are faint. This is indicated in Figure 3.2b, c. Appendix A shows that for a constant conductive flux, which is a crude approximation to an equilibrium coronal loop, the intensity varies as n^{-4} and therefore as ν^{-8}. The very steep spectrum has important implications, as we discuss below. Keep in mind that this is the spectrum of a single loop. The composite spectrum from many loops with different density profiles is much more uniform.

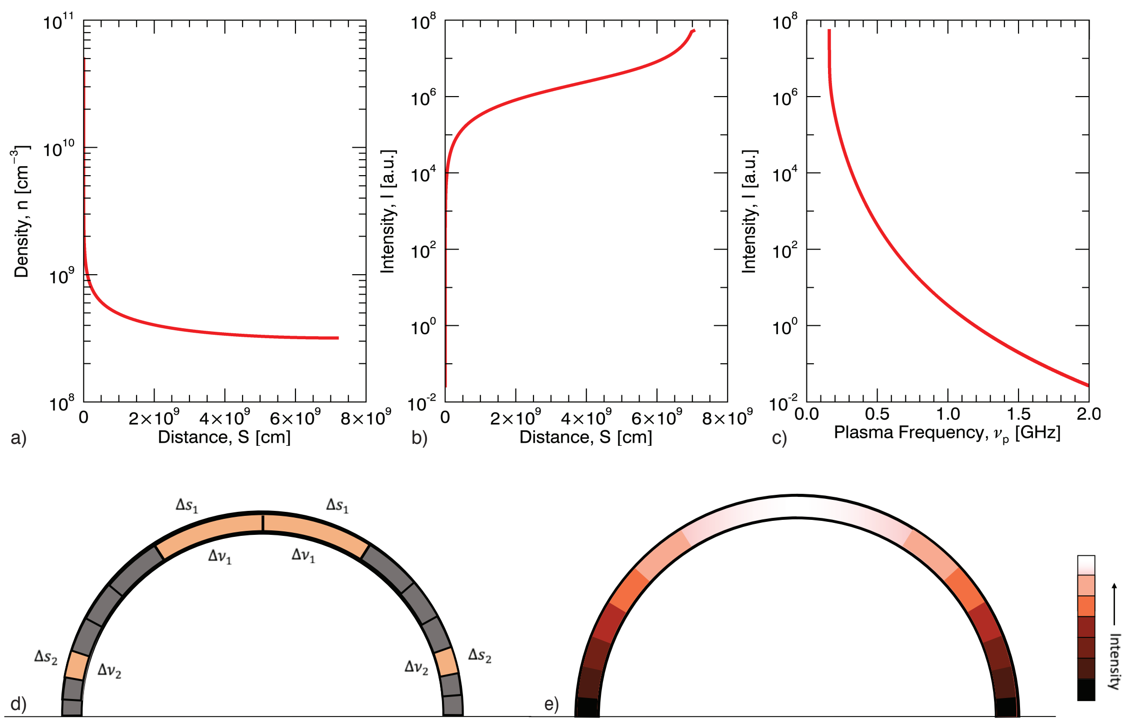

Figure 3.2 a) Density profile for a single loop as a function of distance. b) Relative Intensity, I, in frequency bins of equal size as a function of distance along the loop for a type III burst. c) Relative Intensity as function of local plasma frequency along the loop. d) $\Delta\nu_i$ bins of same width occupy a much larger volume of the loop in the upper corona compared to the TR. e) Intensity variation for a burst vs. location in the loop.

Source: [35].

Referring to Figure 3.2, consider two frequencies ν_1 and ν_2 occurring high and low in the loop, respectively. The frequency bins $\Delta\nu_1$ and $\Delta\nu_2$ centered on ν_1 and ν_2 have the same width, but the corresponding volume elements Δs_1 and Δs_2 are different; $\Delta s_1 > \Delta s_2$ because of the smaller density gradient. The intensity is therefore brighter at ν_1. The shading in Figure 3.2e indicates the total emission coming from each volume element. The differences are due entirely to the variations in volume. Our model assumes that emissivity is uniform along the loop. Similarly, the intensity plotted in Figure 3.2b is not the emission per unit volume at position s, but rather the intensity of the volume element that is centered at s.

We now explore the light curves (intensity versus time) expected when a beam of energetic electrons propagates along the loop. Different frequencies will light up at different times. By cross correlating the light curves with different imposed temporal offsets, we generate a Cross-COrrelation Power Spectrum (CCOPS) [1]. We want to know whether the CCOPS reveals a signature of the beam that might be used to identify type III bursts from nanoflares. We start with very simple scenarios and add increasing complexity to more closely mimic the actual Sun.

3.2.3 Single-Loop Model

Model 1: First consider a single loop with half-length L, as depicted in Figure 3.3. Sample frequencies ν_1, ν_2, and ν_3 correspond to the positions indicated. The loop is symmetric, so each frequency is present in both legs. We now imagine that a nanoflare occurs at three different locations, which we refer to as cases A, B and C. These produce the light curves shown in Figure 3.4, ordered so frequency increases from top to bottom to reflect the relative heights within the loop. The red 'stars' indicate the position and timing of the three different nanoflares.

[1] The term "Power Spectrum" refers to the variation of the amplitude of the cross-correlation coefficient as a function of time-offset and should not be confused with the Fourier transform of the auto-correlation function.

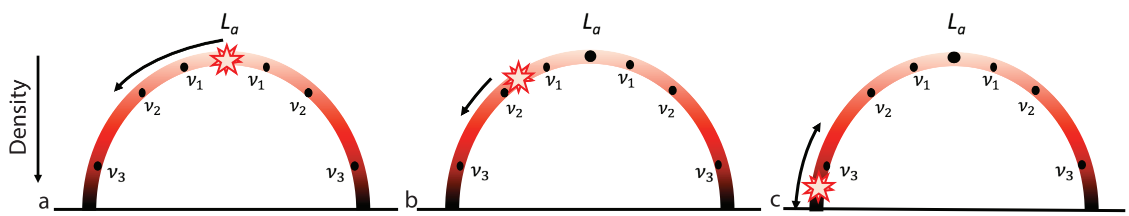

Figure 3.3 Case A: nanoflare at the loop top with particles moving downward to the foot-point; Case B: nanoflare high in the loop leg with particles moving downward only; Case C: nanoflare low in the loop leg with particles moving in both directions. *Source:* [35].

Case A: The nanoflare occurs at the loop apex ensuring all particles only propagate downward (Figure 3.3a). The ejected beam of electrons is assumed to be mildly non-thermal with a fixed energy of 2 keV, hence moving with a constant velocity of 2.65×10^9 cm/s ($\sim 0.1c$). The duration of the beam is chosen to be 20 ms. As the beam propagates along the field, we expect to see emission first at ν_1 followed by ν_2 and then ν_3. The features in the light curves joined by the blue arrows in Figure 3.4 clearly demonstrate this systematic behavior.

Case B: Here we assume that the nanoflare occurs partway down the left leg and that particles propagate downward only. Following from the sketch for case B (Figure 3.3b), it is evident that only ν_2 and ν_3 will show any emission (features joined by the red arrows) since the nanoflare lies below ν_1 and the downward moving particles never pass that location. Emission appears in ν_2 and ν_3 with the same delay as in Case A. We classify this as a positive delay, because the higher frequency occurs after the lower frequency.

Case C: The nanoflare now occurs lower in the loop leg and particles propagate in both directions (Figure 3.3c). Downward propagating particles produce no emission at any of the three frequencies. Upward propagating particles produce emission in ν_3 followed by ν_2 and then ν_1 (green arrows in the figure) as they travel up the leg. These are negative delays because the higher frequency occurs first. As the particles pass the apex and travel down the opposite leg, they produce emission sequentially in ν_1, ν_2, and ν_3, the reverse order. These are positive delays. This reversing of the frequency drift is the same effect observed in U-type bursts mentioned earlier.

The time-lag technique easily identifies the expected delays in these simulations with each nanoflare corresponding to cases A, B, and C. The CCOPS has spikes at the temporal offsets discussed above. However, in addition to finding correlations between two frequencies occurring in the same leg, the technique also finds correlations with longer delays when the burst arrives at the opposite leg. This is illustrated in the

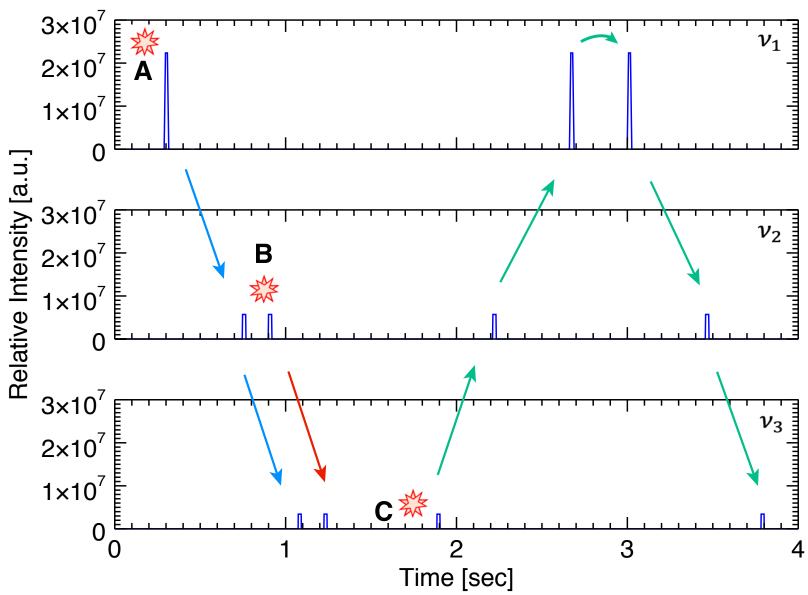

Figure 3.4 Light curves for the three chosen frequencies, showing time offsets as per Cases A, B, and C. The 'red star' marks the relative position along the loop where each nanoflare occurred.

Source: [35].

example CCOPS in Figure 3.5 corresponding to case C from above. We consider frequencies ν_1 and ν_2 that occur at higher altitudes. As indicated in the sketch on the right, there are four combinations of ν_1–ν_2 positions. ν_2 on the left side of the loop pairs with both ν_1 on the left and ν_1 on the right. Both delays are negative, but the first is shorter than the second. ν_1 on the left pairs with ν_2 on the right, producing a long positive delay. Finally, ν_1 on the right pairs with ν_2 on the right, producing a short positive delay. It is clear that the same pattern will hold for nanoflares occurring near the right footpoint, with the beam traveling right to left. In general, we expect the CCOPS to have peaks at four temporal offsets: positive and negative short delays and, positive and negative long delays. This is exactly what we find in our simulation, as shown on the left of Figure 3.5. There will always be peaks at $\pm\Delta t_1$ and $\pm\Delta t_2$ whenever some nanoflares occur at altitudes below the higher frequency, ν_2.

The situation is modified if nanoflares occur only at higher altitudes in the loop. There will be only positive delays, both short and long, if the nanoflares are distributed at locations above the higher frequency, and only positive short delays if they are restricted to the very top of the loop, above the lower frequency.

The above examples concern a single loop. In reality, of course, many loops with different density profiles are observed at the same time, and this adds enormous complexity to the CCOPS. There are estimated to be $\sim$500,000 individual strands (unresolved loops) in a typical AR [98]. The characteristic delay between successive nanoflares in a given strand is $\sim$1000 s [100], implying an occurrence rate of $\sim$500 nanoflares/s across the AR. Even with high spatial resolution observations, the line of sight passes through many loops of differing lengths, heating rates, and density structures. We expect the CCOPS to contain a huge number of peaks, which merge together to produce a smooth spectrum. Meaningful patterns in the envelope may nonetheless persist, as we now discuss. We first consider the effect of multiple loops and then consider the effect of the type III burst occurrence rate.

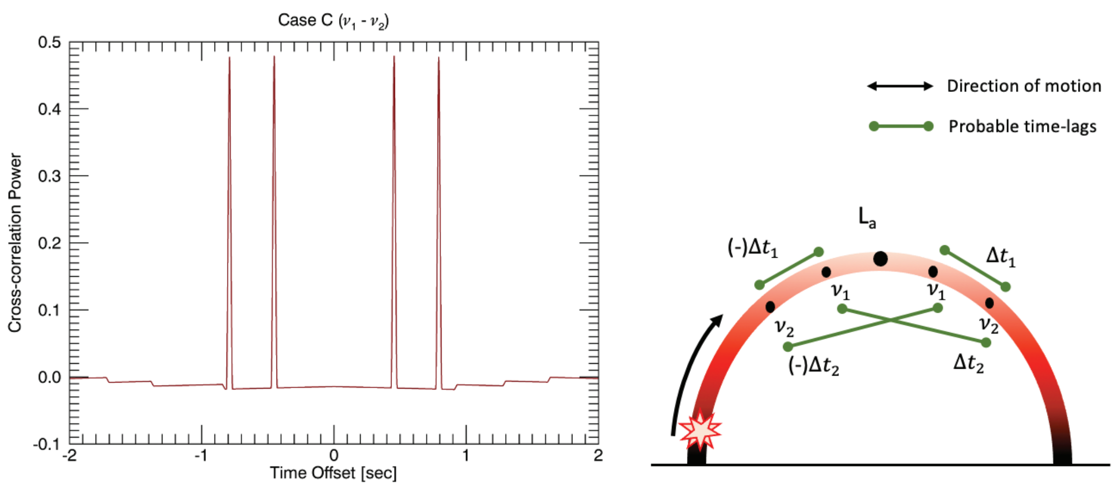

Figure 3.5 Left: CCOPS for $\nu_1 - \nu_2$ from light curves obtained using a generalization of case C. Right side demonstrates the multiple time-lags that peak in the CCOPS. *Source:* [35].

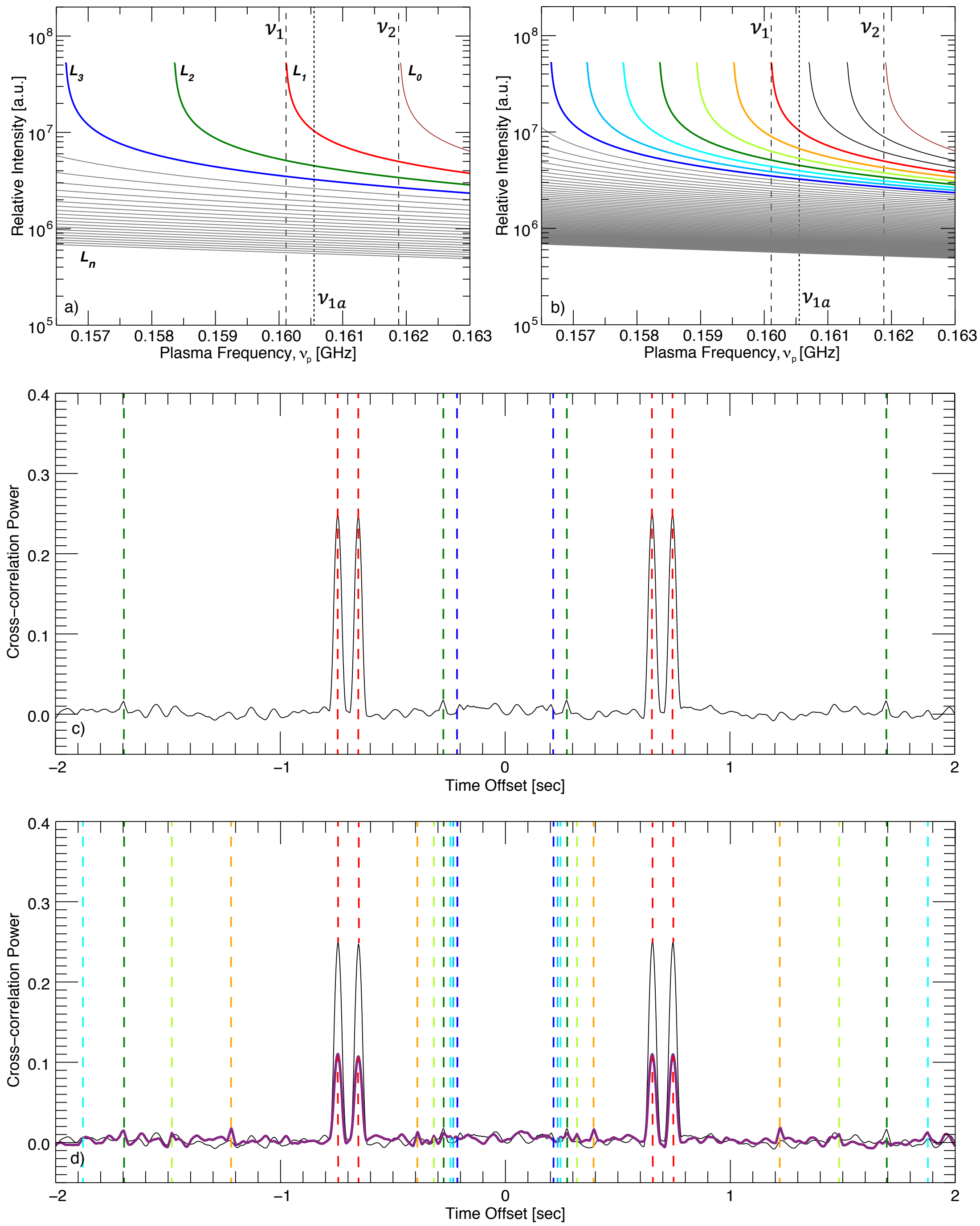

Figure 3.6 a) Low-density ($\eta = 1$) distribution of loops generated for the chosen loop-length range from frequencies ν_1 and ν_2. b) Loop distribution with three times the lowest loop density ($\eta = 3$). c) CCOPS for loop density $\eta = 1$ with color-coded dashed lines overlaid to represent the expected time-offsets for each loop. d) CCOPS for loop density $\eta = 3$, with color coded dashed-lines representing expected time-offsets for the additional loops as well.

Source: [35].

3.2.4 Multiple Loops

Loop half-lengths in an AR typically vary between ~10,000–150,000 km, giving a wide range of density profiles and therefore a broad band of plasma frequencies that can be observed. However, the precipitous fall in intensity as a function of frequency shown in Figure 3.2c has important implications. Systematic time delays between any two frequencies are only expected for the emissions coming from a single loop. Emissions from different loops are physically uncorrelated and therefore have random delays. The rapid drop in intensity for a single loop means that we expect an observable signal from that loop only for frequencies that are closely spaced. If the spacing is too great, at least one of the frequencies will be too weak to produce a meaningful signal. Because we require a reasonable signal in both frequencies, we need concern ourselves only with loops having a rather narrow range of apex densities (uniquely determined by their lengths in our simplified model). All other loops will be faint at these frequencies. This also shows that in order to consider emission from all loops in an active region, multiple different pairs of frequencies will need to be considered.

3.2.4.1 Loop Distribution. Consider the spectra of several loops with equally spaced lengths ΔL shown in Figure 3.6a. Note that the intensity scale is logarithmic. Four of the loops are color coded and labeled L_0 through L_3. The ΔL increment of loop lengths is determined by the following choice of frequencies. Frequency ν_1 occurs just below the apex of L_1 (red), and frequency ν_2 occurs a short distance down the leg, where the intensity is reduced by a factor of 10. The plasma frequency at the apex of L_0 (brown) is slightly larger than ν_2, so neither frequency occurs in that loop. The longest loop shown (labeled L_n at the bottom) is approximately 100 times fainter than L_1 at frequency ν_1. We assume that all loops longer than this are so faint that they can be safely ignored in our simulations.

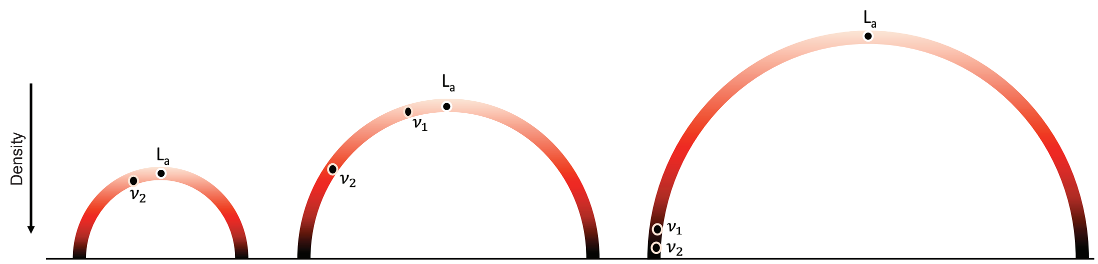

Figure 3.7 Relative position of frequencies along loops of varied lengths. As the loop become shorter from right to left, the density at the loop-top increases such that only one of the frequencies, ν_2 exists along the shortest loop. For a loop even shorter, the density will increase further such that neither of the frequencies exist along the loop anymore.

Source: [35].

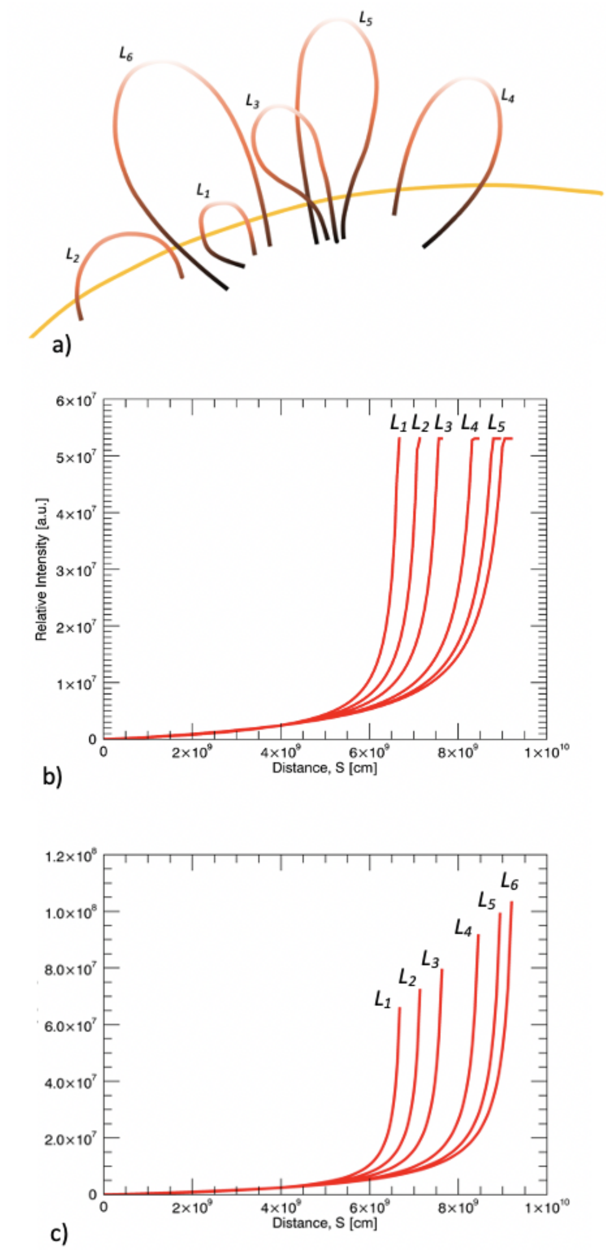

Figure 3.8 a) Cartoon showing multiple loops in an AR with different orientations and lengths. (b-c) Corresponding plots for Relative Intensity as a function of distance along the loop, I vs s for two cases, with short beam length b) and long beam length c).

Source: [35].

Figure 3.7 is a schematic representation of the loops. The middle loop is similar to L_1, with both frequencies being relatively bright. The long loop would correspond to one of the unlabeled grey loops in Figure 3.6a, where both frequencies are relatively faint. Finally, the short loop represents a loop falling between L_1 and L_0, for which ν_2 is bright, but ν_1 does not occur in the loop.

Loops having a given range of lengths can occur at multiple locations within an active region, and they need not have similar orientations. This is indicated schematically in Figure 3.8a to emphasize that the loops need not be nested as in a single, simple arcade.

The intensity as a function of distance along the loop for individual loops is shown in Figure 3.8b & c for two extremes of relative beam length. Figure 3.8b shows flattening of the intensity near the loop top for the case where the chosen beam length is shorter than the volume elements, $\Delta s_i > L_b$ as mentioned in Subsection 3.2.2, so the intensity near the loop apex is proportional to L_b. Figure 3.8c shows the same plot for a beam length that is longer than the volume elements everywhere along the loop i.e. $\Delta s_i < L_b$ with the intensities proportional to Δs_i even near the loop apex.

The corona has a continuous distribution of loop lengths, but we imagine that only a fraction of loops experience nanoflares. We consider three different population densities of such loops. The loop length spacing is $\Delta L/\eta$, where ΔL is the spacing in Figure 3.6a.

Model 2.1 (Low Loop Population Density): We first examine the case $\eta = 1$, corresponding to a low population density (Figure 3.6a). There are 23 loops in the chosen range of loop lengths. Assuming 500 nanoflares/s in an entire active region, we estimate 30 nanoflares/s over this range. All nanoflares are assumed to produce electron beams lasting 20 ms. This is shorter than the typical travel time between the two frequencies.

The nanoflares occur at random times and random locations within the loops. Electron beams are assumed to propagate in both directions. We run the simulation for 1200 s, during which time 36,000 nanoflares are initiated. Figure 3.6c shows the CCOPS for the frequency pair $\nu_1 - \nu_2$, where we have used all except the first and last 10 s of the light curves. The dashed vertical lines indicate the expected time-lags for loops L_1, L_2, and L_3, color-coded to match the spectra in Figure 3.6a. There are clear peaks at the expected locations, especially for L_1 (red). It is not surprising that this loop dominates, as it produces the brightest emission at both frequencies, but especially ν_1, which comes from near the apex. The CCOPS peaks are much weaker for L_2 (green) and L_3 (blue), with L_2 being somewhat stronger because it is somewhat brighter.

All loops except L_0 will produce four peaks in the CCOPS, since at least some nanoflares occur below the location of ν_2 in each case. Notice that the short delay, $\pm\Delta t_1$, is smaller for L_2-L_n than for L_1. Similarly, the long delay, $\pm\Delta t_2$, is bigger. This is easily understood based on the sketches in Figure 3.7, where the intermediate loop represents L_1 and the long loop represents L_2 and L_3. The conjugate frequency positions in the right legs are not shown.

There is a low level of "noise" in the CCOPS. This is not due to true noise in the light curves, which will be discussed later. Rather, it is due to ν_1 from one nanoflare in one loop correlating with ν_2 from a different nanoflare in a different loop. There is no temporal relationship among the nanoflares, and so the power associated with these "false" correlations is spread roughly evenly over the range of offsets. Note that the power can be both positive and negative, as expected based on the definition of the cross correlation (see Appendix B).

Model 2.2 (Moderate Loop Population Density): Now consider the situation where the loop population density is three times greater: $\eta = 3$. This is shown in Figure 3.6b and d. There are 69 loops in total, spanning the same range of lengths

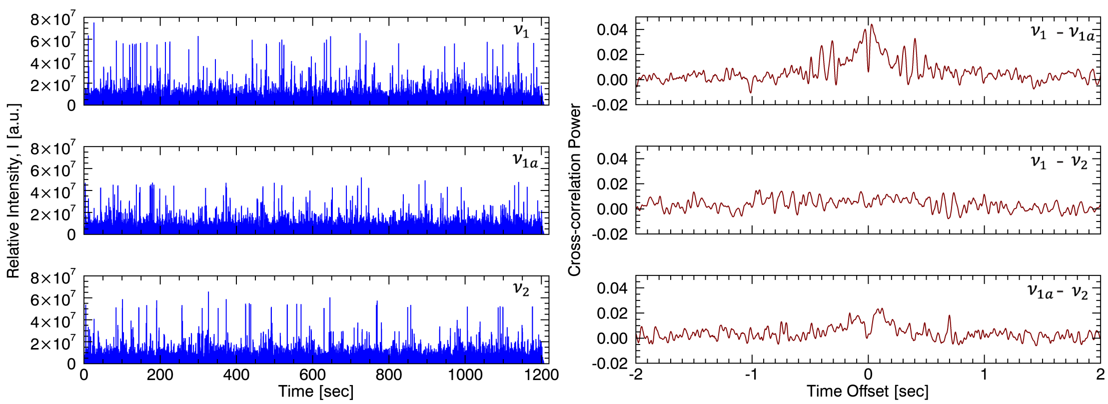

Figure 3.9 Left: Light curves for the three chosen frequencies, ν_1, ν_{1a}, ν_2 for high-density loop distribution with 30 nanoflares occurring per second all generating type III bursts. Right: Corresponding CCOPS for each pair.

Source: [35].

as before. New peaks appear in the CCOPS that were not present previously. We expect three times as many, though most are not visible. The amplitudes of the peaks that are common to both simulations are reduced (lower cross-correlation power), as discussed in Appendix B.

Notice that the spectra for the two loops between L_0 and L_1 in Figure 3.6b do not have meaningful peaks in the CCOPS because they only emit at frequency ν_2. That emission is quite strong, however, and exacerbates the problem with false peaks. This is a primary reason why the amplitudes of the true peaks are reduced compared to the first simulation.

Model 2.3 (High Loop Population Density): Our final example has a much higher population density that approximates a truly continuous distribution of loop lengths: $\eta = 50$, resulting in 1150 loops. This is essentially equivalent to every field line experiencing nanoflares. We include a third frequency for the analysis, ν_{1a}, that lies between ν_1 & ν_2, marked by the dotted line in Figure 3.6a,b. For this simulation we expect a forest of peaks in the CCOPS. Light curves for the three frequencies are shown in Figure 3.9, left panel. The associated CCOPS for each pair are shown in the right panel. We note that the power of the cross-correlation has reduced drastically. Even so, a signature is visible above the 3σ level for at least the pair ν_1–ν_{1a}. There is a noticeable dip at 'zero' lag that increases towards both positive and negative time offsets, peaks at a certain lag, and then decreases again. This 'M' shaped pattern is the result of a nest of peaks from multiple loops with very similar time-lags. The peaks for longer delays corresponding to $\pm\, \Delta t_2$ from Figure 3.5 are visible for a few of the brightest loops only.

A similar pattern is also visible in the CCOPS for the other two pairs of frequencies, but it is important to note here that the signal-to-noise ratio (SNR) of the power is quite low.

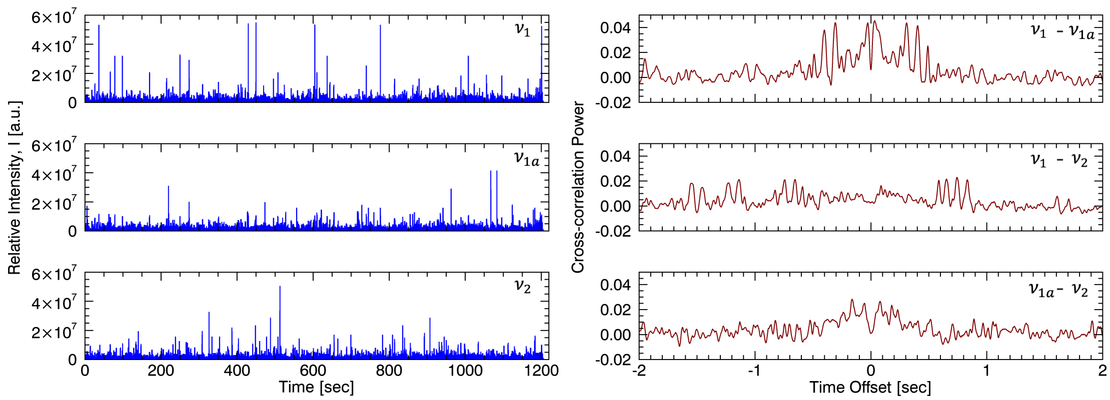

Figure 3.10 Left: Light curves for the three chosen frequencies, ν_1, ν_{1a}, ν_2 for the high loop density distribution with 30 nanoflares occurring per second but only a tenth of them generating type III bursts (3 bursts/s). Right: Corresponding CCOPS for each pair.

Source: [35].

The distinctive dip in power at zero lag can be understood on the basis of Figure 3.7. Small lags are produced in loops where both frequencies are close to the footpoint. The intensity is greatly reduced at these locations, so the cross correlation power is weak.

3.2.4.2 Burst-Frequency. The three simulations above assume that nanoflares occur at a rate of 30 per second across the range of loop lengths considered, and that every nanoflare produces a type III burst. It is certainly possible that only a fraction of nanoflares accelerate energetic electrons, and so the rate of type III bursts could be much less. We therefore repeat $Model$ 2.3 above (high loop population density), but with a ten times smaller type III burst rate: 3 $bursts/sec$. The light curves for all three frequencies are shown on the left in Figure 3.10, and the CCOPS for three frequency pairs are shown on the right. Note that the CCOPS here are not very different from the ones shown in Figure 3.9. An 'M' shaped pattern and dip at zero lag are still present.

The results from a still-further decrease in the burst frequency to one in every hundred nanoflares (0.3 $bursts/sec$) is shown in Figure 3.11.

Figure 3.12 a) shows CCOPS from Figure 3.11 and b) shows CCOPS from Figure 3.9 corresponding to 30 $bursts/sec$ and 0.3 $bursts/sec$ respectively with the expected time-lags overlaid. The orange dot-dashed lines clearly show how the M-shaped pattern arises from a clustering of expected peaks at the shorter time-lags Δt_1. The longer time-lags Δt_2 are marked by the green dot-dashed lines. For a high burst frequency (panel a), the longer lags have waned due to the sheer number of bursts, however many of the individual peaks are prominent at the expected positions for the low burst frequency (panel b).

An observation to make is that as we reduce the burst frequency to one-tenth and then further to one-hundredth of the chosen nanoflare rate, there is an increase

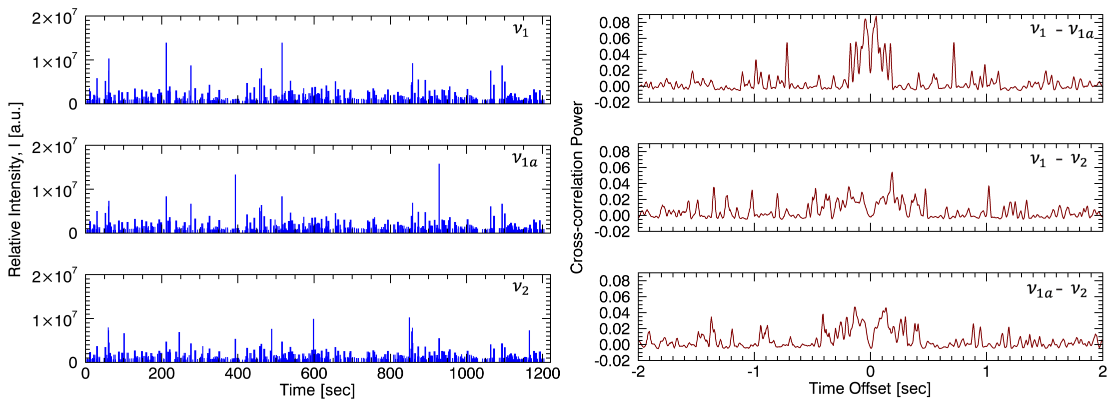

Figure 3.11 Left: Light curves for the three chosen frequencies, ν_1, ν_{1a}, ν_2 for high-density loop distribution with 30 nanoflares occurring per second but only a hundredth of them generating type III bursts (0.3 $bursts/sec$). Right: Corresponding CCOPS for each pair.

Source: [35].

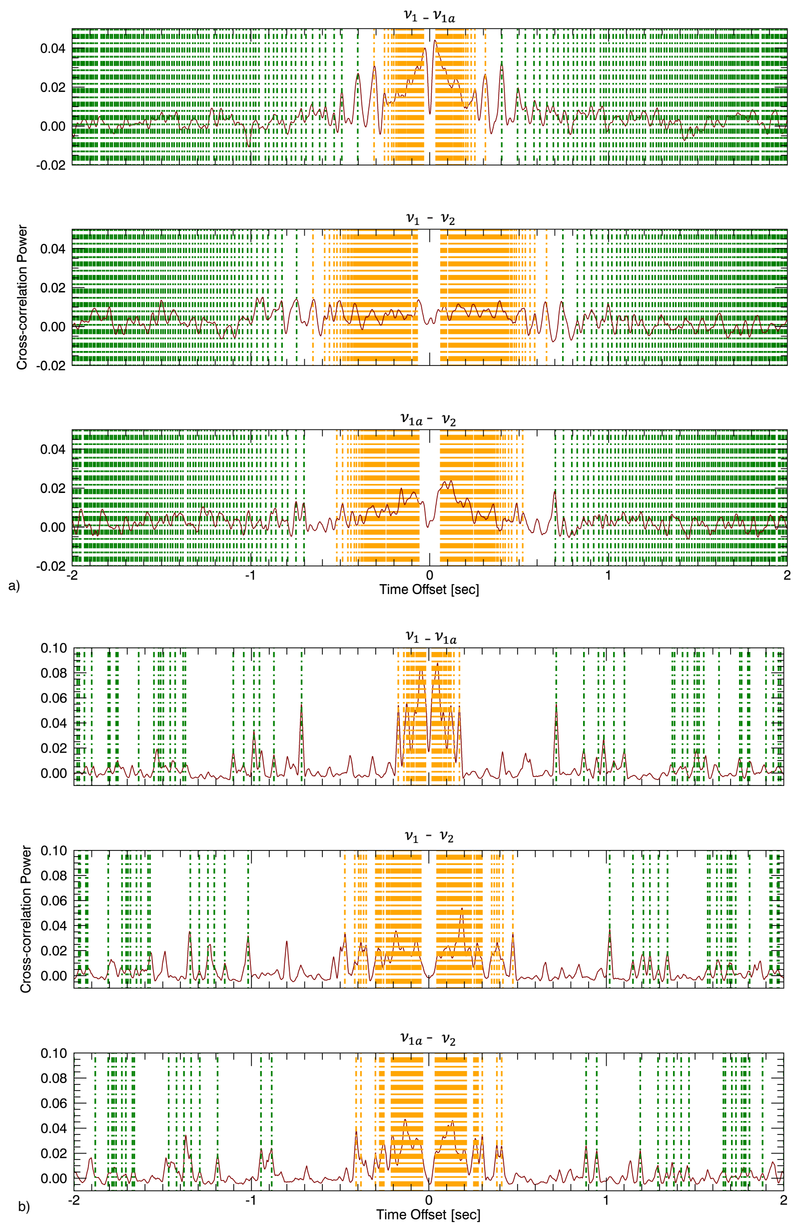

Figure 3.12 a) CCOPS for 30 bursts/s with expected time-lags overlaid. b) CCOPS for 0.3 bursts/s with expected time-lags overlaid. The orange dashed lines mark the expect time-lags Δt_1 and the green dashed lines mark the expected time-lags Δt_2 *Source:* [35].

in power of the cross-correlation peaks. Note that we expect fewer 'false' correlations within the range of offsets shown. The average interval between bursts is 3 seconds in the lowest frequency simulation, which is outside the range of -2 to +2 s in the figure. The overall level of "noise" is therefore reduced. Nonetheless, some of the distinctive narrow peaks in the CCOPS are false peaks associated with pairs of closely spaced events that occur near the apex of two different loops and are therefore relatively bright at both frequencies.

3.2.4.3 Duration of the Bursts. Traditional type III bursts in the inner heliosphere may last for a few tens of minutes [154], however for type IIIs occurring in the closed corona, the observed durations are much shorter [33]. The burst duration depends on both the lifetime of the acceleration process and the decay time of the Langmuir waves generated in the volume. We present our model as though the beam is an emitting object, but it is understood that the duration of emission from a given point in space includes the decay of the Langmuir waves that are generated by the high energy electrons, i.e., our 'beam' is a column of emission that is longer than the electron beam. The duration of the burst at each frequency ν_i then depends on the time it takes for the beam to propagate through the Δs_i volume element associated with the central frequency ν_i. For all multi-loop models discussed above, the duration of the beam was chosen to be 20 ms. Most of the expected time lags between the frequency pairs are longer than this duration.

We now evaluate how well the technique performs when the beam duration is comparable to or longer than the expected time lags. Figure 3.13 shows the CCOPS for *Model* 2.3 (comparable to Figure 3.9) except with beam durations of 200 ms and 1 s. As the duration increases, the peaks in the CCOPS broaden and begin to merge. The dip at zero lag fills in, and the 'M'-shaped pattern disappears, though a hint remains for frequency pair $\nu_{1a} - \nu_2$ at a duration of 200 ms. The individual peaks and

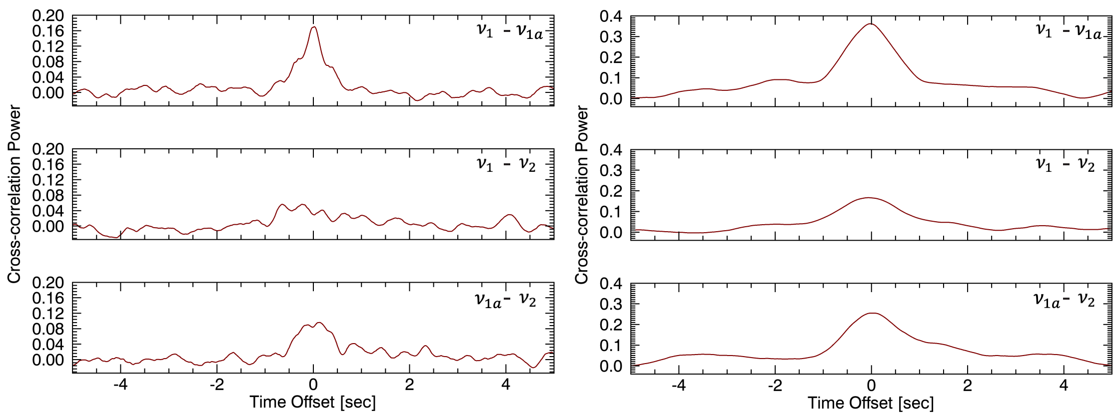

Figure 3.13 Left: CCOPS for the three chosen pairs of frequencies for a burst duration of 200 ms. Right: CCOPS for the same frequency-pairs for a burst duration of 1 s.

Source: [35].

'M'-shaped pattern are broadened to produce a pronounced hump centered at zero lag. Although this removes the direct delay signature of the type III bursts, because such a hump could instead be a result of in-phase variability at the two frequencies, the width and the shape of the hump may still provide evidence for drifting (type III) bursts if its width is substantially greater than the combined durations of the variations in the light curves, as discussed in Appendix B.

3.2.4.4 The Role of Noise. The final test is to model the technique with an additional level of noise. For this purpose, we use *Model* 2.3 again. To add a realistic level of noise to the light curves we need to understand the various factors that affect the sensitivity of a radio interferometer. At frequency ν, the flux density associated with a given antenna temperature[2] is given as:

$$S = \frac{2kT_a\nu^2}{c^2}d\Omega \tag{3.6}$$

where k is the Boltzmann constant, T_a is the antenna temperature due to a hot source filling the antenna primary beam (field of view), c is the speed of light, and $d\Omega$ is the solid angle subtended by the beam (see Section 1.3 for a detailed derivation). If a hot source of temperature T does not fill the beam, the antenna temperature is reduced ($T_a < T$) by the beam dilution factor (ratio of the angular area of the source to the beam area). The noise associated with a radio antenna is a combination of this antenna temperature due to the source and the noise generated internally by the receiving system, $T_{\rm sys}$. Crane & Napier [41] showed that the sensitivity for an array of such antennas is given by:

$$\Delta T = \left[\frac{T_a^2 + T_aT_{\rm sys} + {T_{\rm sys}}^2/2}{\Delta\nu\tau N(N-1)}\right]^{1/2} \tag{3.7}$$

[2]This is not the antenna's physical temperature but the temperature that a blackbody would have in order to provide the equivalent power received by the antenna.

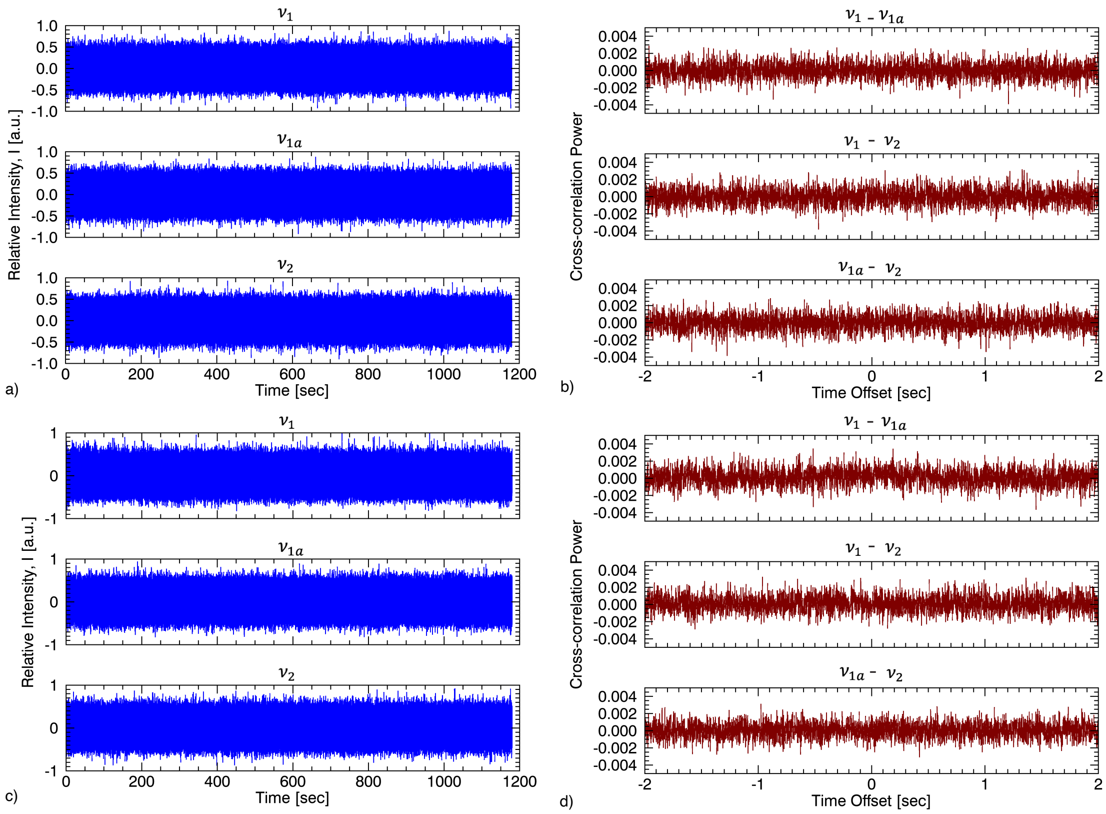

Figure 3.14 a) Flux density for a brightness temperature $T = 10^{12}$ K at frequencies ν_1, ν_{1a}, ν_2 for the high loop density case with 0.3 bursts/s. Random Gaussian noise with an rms of 0.09 sfu is added to each of the light curves. b) The CCOPS corresponding to the light curves in a). c) Same as (a) for a higher rate of 30 bursts/s. d) The CCOPS corresponding to the light curves in (c).

Source: [35].

where, $\Delta\nu$ is the channel width of the instrument and τ is the cadence, and $N(N-1)$ is the number of baselines. For a bright source such as the Sun, $T_{\rm a} >> T_{\rm sys}$. Simplifying Equation (3.7) and substituting in Equation (3.6), we have the noise associated with a source of flux density S as

$$\Delta S = \frac{S}{\sqrt{\Delta\nu\tau N(N-1)}}. \tag{3.8}$$

Therefore, for a source with flux density S, the sensitivity has a direct dependence on T_a and an inverse dependence on the frequency bandwidth, $\Delta\nu$, integration time τ and the number of baselines.

Anticipating a future analysis of P-band (245–450 MHz) solar observations we have in hand, taken with the Very Large Array (VLA) [143], we estimate a level of noise as follows. The calibration procedure for P-band data from the period of interest has not yet been finalized, so we adopt an average flux of 25 sfu at 245 MHz based on values reported in the NOAA catalogue for times of similar activity. Using numbers appropriate to our existing P-band observations, $\Delta\nu = 125$ kHz, $\tau = 0.01$ s and number of antennas in the subarray $N = 14$, Equation (3.8) gives an uncertainty of $\Delta S = 0.0524$ sfu.

An independent estimate of the uncertainty can be obtained from the data by taking the root mean square (RMS) intensity difference between two frequencies that are so closely spaced that any real differences in source flux density are likely to be negligible, although fluctuations due to source confusion [210] may still be present. Because of possible cross-talk between adjacent channels, we use channels separated by one intervening channel. Lacking calibrated P-band data, we use data near 1 GHz from the L-band, which are calibrated. The RMS difference is 3.5 times larger than the uncertainty given by Equation (3.8) using the values appropriate to that band. This suggests the presence of additional sources of random variations, perhaps akin

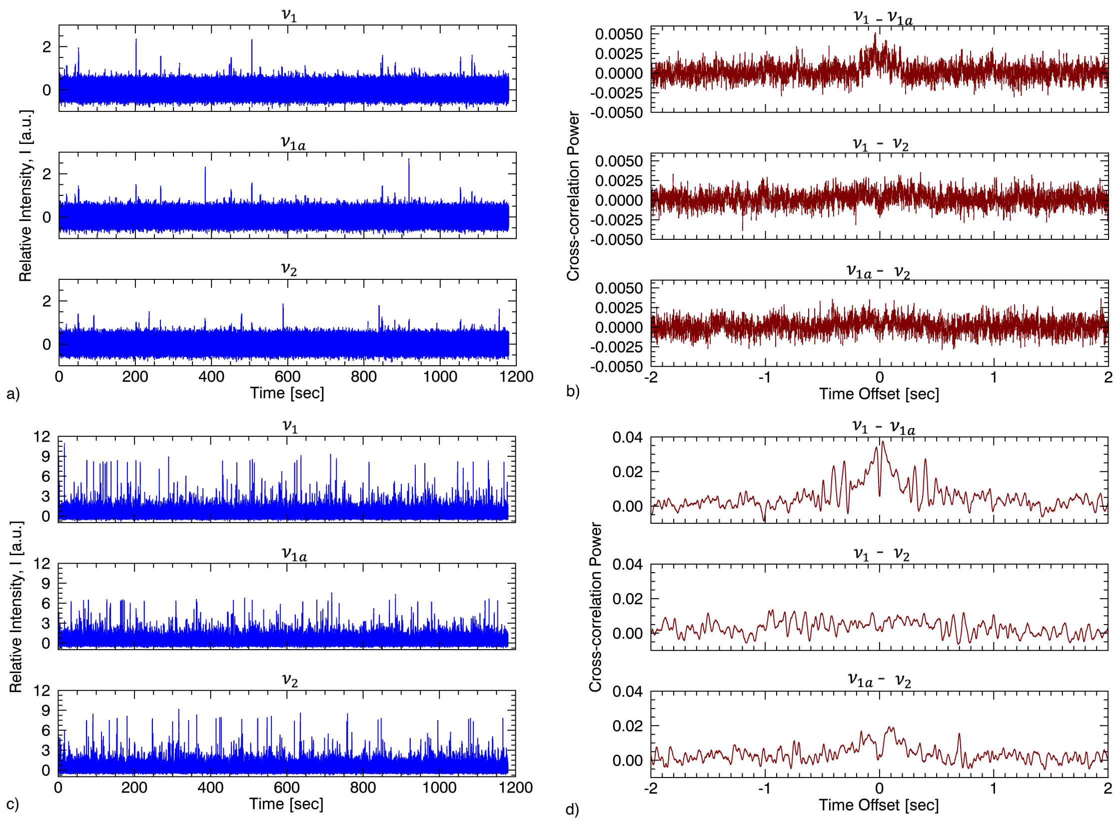

Figure 3.15 Same as Figure 3.14 for bursts with an order of magnitude higher brightness temperature, $T = 10^{13.3}$ K.

Source: [35].

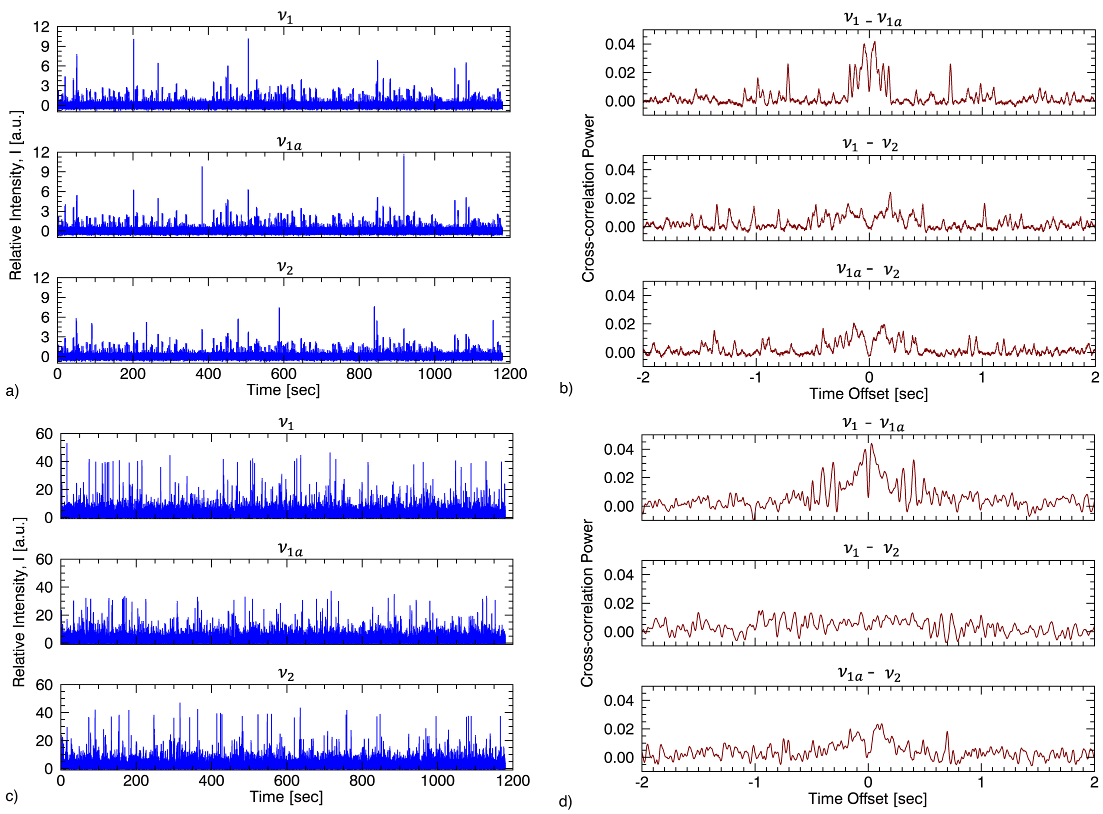

Figure 3.16 Same as Figure 3.14 for bursts with three orders of magnitude higher brightness temperature, $T = 10^{14}$ K.

Source: [35].

to those reported by Zirin et al. [210]. We assume that they are also present at about the same level in the P-band data, so we multiply the 245 MHz uncertainty above by the same factor of 3.5 to obtain $\Delta S = 0.186$ sfu, which we apply to our models.

All intensities from $Model$ 2.3 are first converted to a flux density using Equation (3.6) above, where the solid angle $d\Omega$ is calculated for each nanoflare at frequency ν with a volume element Δs and assuming a width of $\approx$ 200 km for the magnetic strand [98]. Since the brightness temperatures of these nanoflares are unknown, we repeat the calculation for three temperatures, viz. 10^{12}, $10^{13.3}$ and, 10^{14} K. Randomly generated Gaussian noise with an rms of 0.186 sfu is then added to the light curves of each frequency and the CCOPS computed.

Figures 3.14, 3.15 and 3.16 show flux densities computed at temperatures $T = 10^{12}, 10^{13.3}$ and 10^{14} K at all three frequencies for 0.3 bursts/s and 30 bursts/s in panels a and c, respectively, with the noise added. The corresponding CCOPS for each pair of frequencies are shown in panels b and d. Light curves in Figure 3.14 computed for temperature $T = 10^{12}$ K are completely dominated by noise and show no meaningful peaks in the CCOPS.

The rather specific value $T = 10^{13.3}$ K was chosen as an example where there are only minimal excursions above the noise in the light curves (Figure 3.15a), yet the CCOPS (panel b) shows a hint of the 'M'-shaped pattern. The flux densities of the higher burst frequency case in panel c have a substantial increase in the signal above the noise, and hence the CCOPS now look very similar to Figure 3.9 with a very slight decrease in the power.

Any further increase in the brightness temperature significantly increases the signal-to-noise ratio for both cases of burst frequencies and consequently resuscitates the CCOPS to their former shapes with a slight reduction in the cross-correlation amplitude that is caused by the noise. The light curves and corresponding CCOPS for such a case with $T = 10^{14}$ K are shown in Figure 3.16. Despite such an increase in the brightness of the bursts, the fraction of total flux density due to nanoflares is only 0.055.

3.3 Conclusion

We perform numerical modeling to simulate idealized emission from type III radio bursts that may be generated by particle acceleration from nanoflares. For the sake of simplification, our model makes the following assumptions: (i) our model loops are symmetric; (ii) all bursts produce electrons of the same velocity, which remains constant as the beams propagate along the loops; (iii) the burst emission is generated instantaneously as the beam is ejected from the nanoflare site; (iv) the emissivity for all bursts is taken to be the same at all loop positions; (v) the decay time of the Langmuir waves is independent of frequency.

Relaxing assumption (i), loop symmetry, would affect the time delay symmetry shown in Figure 3.5. Regarding assumption (ii), modeling of type IIIs by Reid & Kontar [153] shows that the velocity of the bursts eventually decreases as the beam moves away from the Sun, however the evolution of beam speeds in closed loops is unknown. Assumption (iii) ignores the fact that it may take time for the beam to develop a two-stream instability and hence produce Langmuir waves, but this should not affect our results unless nanoflares occur strongly preferentially at the apex of loops, since we have shown that emission on closed loops is expected to be dominated by loop-top emission from beams originating at any location. Assumption (iv) would alter the intensity curves of Figure 3.2, but the intensity dependence is so strong that only extreme violations of this assumption in favor of loop leg emission would make much difference. Assumption (v) should not be significant unless the decay time has a strong dependence on frequency, since only closely spaced frequencies contribute significantly to the CCOPS. Some aspects of assumption (v) were explored in our study by showing how different durations of bursts will affect the CCOPS.

Once the light curves are obtained from our model, the simulated light curves at chosen radio frequencies are then cross-correlated to identify time-lags between different pairs, using a novel application of the time-lag technique [183]. We find that the signature of the bursts depends very much on the rate and duration of nanoflares and on the fraction of loops that are involved. Individual peaks dominate the CCOPS when only a small subset of loops experience nanoflares that accelerate energetic particles. When many loops experience such nanoflares, the signature varies depending on whether the beam duration is short or long compared to the particle travel time associated with the two frequencies. Short durations produce a quasi-continuous 'M'-shaped pattern with a distinctive dip at zero lag. Long durations produce a broad hump centered at zero lag. These differences can be exploited to determine the likelihood of particle acceleration and the properties of the beam, and therefore better understand the acceleration mechanism.

In general, the signatures are stronger for pairs of frequencies that are closely spaced, indicating that high frequency resolution observations must be used. This is due to the extremely steep slope of the type III spectrum of an individual loop, which is related to the highly nonuniform density gradient along the loop. In order for the intensities to be reasonably strong, both frequencies must occur relatively high in the loop. Emission from the lower leg and transition region is comparatively negligible.

False peaks can appear in the CCOPS, especially if the burst rate is high. These are due to correlations between different nanoflares occurring in different loops. The value of the time lag of such peaks is not meaningful, but their mere existence would be indicative of radio bursts and therefore would be an important observational feature.

Whether type III bursts from nanoflares are detectable depends on the SNR. Our noise tests based on estimates of noise for VLA data reveal that for type IIIs with a low brightness temperature, the noise will completely wash out any emission and the CCOPS will show no correlation. Given a high enough brightness temperature for the events, the emission does rise above the noise level and although the power of the cross-correlation peaks in the CCOPS remains small, the change in the widths of the peaks in comparison to the CCOPS computed for a noise-dominated simulation itself is an indication of the presence of bursts. We note that for an instrument with higher sensitivity compared to VLA, the power of the peaks in the CCOPS will improve.

A possible criticism of the central idea of this study, that nanoflares may produce type III emission on closed loops, lies in the apparent fact that observations provide little evidence for type III emission on closed loops beyond relatively rare 'U' or 'J' bursts. However, our analysis of the expected emission from equilibrium loops reveals that such emission should be extremely strongly concentrated at the loop apex (Figure 3.2c). Remarkably, this predicts that the observational signature of type III bursts in closed loops is a bright, narrow-band feature with perhaps a faint high-frequency tail, which fits the description of the very commonly observed type I bursts. The narrow spread is expected if the burst occurs in a single loop or several adjacent loops with similar apex densities, and the emission frequency would directly provide the loop apex density. Thus, our model suggests a possible origin of type I bursts as a natural consequence of type III emission in a closed-loop geometry. We emphasize that the extreme variation in brightness is a consequence of the closed-loop geometry. In contrast, a type III burst on an open field line, or a very large closed loop with a lower density gradient, would show the classic type III, 'U', and 'J' burst characteristics. Del Zanna et al. [47] have suggested that both distinguishable type III bursts and noise storms can be produced together by interchange reconnection at the boundary between open and closed field lines. To our knowledge, we have offered the first explanation for why the noise storms have a narrow frequency spread.

We have begun to apply the knowledge gained from these simulations to actual observations. Results from ground-based radio observatories are currently under investigation. Work based on the the FIELDS instrument on Parker Solar Probe to look for signatures of type IIIs in the solar wind is discussed in the next chapter.

CHAPTER 4

SIGNATURES OF TYPE III RADIO BURSTS IN THE SOLAR WIND FROM SMALL-SCALE RECONNECTION EVENTS

4.1 Introduction

Type III bursts, as mentioned in Chapters 1 and 3 can be produced by interactions between energetic beams of electrons and the ambient plasma. Until now, we concerned ourselves with the type III emission from energetic particles that nanoflares may produce in the closed corona. However, in the context of the solar wind, these energetic beams can originate from several small-scale processes. For example, interchange reconnection from the nanoflares or turbulence reconnection in the lower corona can produce beams that escape along the open field. Similarly, reconnection at the streamer tips can also have the same effect. Furthermore, Borovsky [17] argued that the solar wind is suffused with flux tubes and that these flux tubes, although aligned with the Parker spiral, exhibit a spread of orientations which may result from misalignments in the field lines. Reconnection from the current sheets formed as the plasma in the solar wind reconfigures to achieve a low energy state may also be a source of such energetic beams. A more pertinent question, however, is whether these processes are efficient at accelerating particles?

The work presented in this chapter is an extension of the study reviewed in Chapter 3 to look at radio observations from the Parker Solar Probe spacecraft [66]. Chapter 3 presented modeling of type III emission from nanoflares in closed coronal flux tubes (MCL henceforth); the purpose of this study is to analyze radio emission in the solar wind (i.e., the open field) that may come from small-scale reconnection events. We discuss the *preliminary* results from our initial modeling and compare them with radio observations from the Parker Solar Probe. Details of the observations used for the analysis are given in Section 4.2. Section 4.3 describes the simple model we build to predict the signatures that would be visible in the data from the solar wind. The findings from the model are then compared with the data in Section 4.4. Finally, we summarize the results in Section 4.5 and discuss the next steps.

4.2 Data from the Parker Solar Probe

Parker Solar Probe (PSP) was launched in August 2018, and as of this writing, it has completed four Venus flybys (and seven solar encounters/perihelia) to assist its trajectory toward the Sun. The spacecraft moves closer to the Sun with each encounter and is planned to eventually make observations at a distance of $\sim 10R_\odot$ from the Sun. The mission's primary goal is to study the physics of the inner heliosphere using a combination of four instruments. For the purpose of this study, we use radio observations from the FIELDS instrument [9], which makes measurements of the electric and magnetic fields, waves, and plasma density in the solar wind. We concern ourselves with the Radio Frequency Spectrometer (RFS) [147], which consists of a dual-channel receiver that uses the four monopole antennas (V1-V4) and the search-coil magnetometer (SCM) to measure the electric and magnetic fields. The spectrometer observes at two radio frequency bands; the low-frequency receiver spans the frequency range between 10.5 kHz - 1.7 MHz, and the high-frequency receiver, between $1.3 - 19.2$ MHz.

Observations from encounters one to five (E01-E05) at both LFR and HFR frequency bands were analyzed for this study during the days when the spacecraft took high-rate observations. Figure 4.1 shows HFR spectrograms from E01-E05 (panels a-e) for ± 3 days from the perihelion for each orbit to show a comparison in the activity observed. While E01 and E03 showed little to no visible activity in the spectrograms, E02 shows extensive activity and a myriad of bright type III bursts. A detailed discussion of the statistics and polarization of the type III bursts observed during E01 and E02 can be found in Pulupa et al. [146]. Numerous intense type IIIs

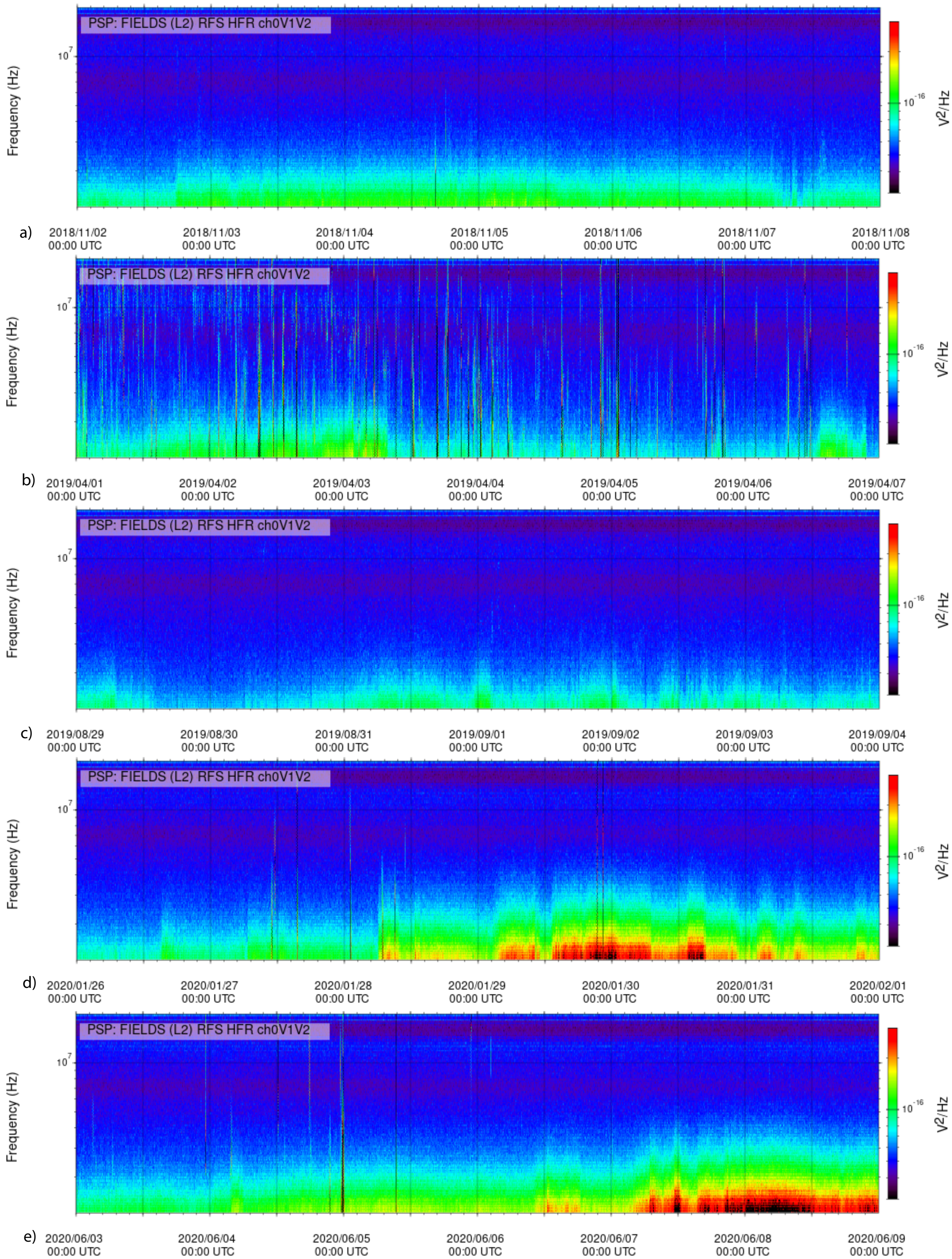

Figure 4.1 High-frequency (RFS-HFR) dynamic spectra for ±3 days from the perihelion for encounters E01-E05 (a-e) showing difference in activity observed during each encounter.

Source: [36]

are also present during E04 and E05, although they may be difficult to distinguish due to the bright emission dominating the low frequencies. We discuss selective time-periods from the different encounters in Section 4.4 and compare them with comparable models to verify that their respective cross-correlation power spectra (CCOPS) show similar signatures.

4.3 Preliminary Modeling

The model discussed in Chapter 3, MCL, simulates radio emission from nanoflares in the closed corona. However, the frequency drifts from type III bursts in the open field are unidirectional, meaning the beam moves outward only and produces type III emission, first at high frequencies and then at low frequencies with some time delay. Thus a separate model is needed to look for signatures of particle acceleration from small-scale reconnection in the solar wind. At this initial stage, we first analyze the bursts that are obvious in the spectrum. The model aims to simply verify and understand the patterns/signatures in the CCOPS based on the different properties exhibited by type III bursts in the open field. Therefore, for the time being, we restrict ourselves to a simple model. Findings from our initial tests of the CCOPS will aid the identification of real signatures of type IIIs in quiet periods.

We create a single type of magnetic flux tube that is rooted in the photosphere at one end and expanding into the interplanetary medium. A power-law density profile is chosen for the flux tube, such that it lies partway between the observed densities of a low-density coronal hole and a high-density streamer as shown in Figure 4.2a (solid black line) and is expressed by the following equation:

$$n = 8.57 \times 10^6 (r^{-3.1}) \quad [\mathrm{cm}^{-3}] \tag{4.1}$$

where r is the distance measured from the surface. The empirical density models created using polarized brightness measurements from white-light observations are

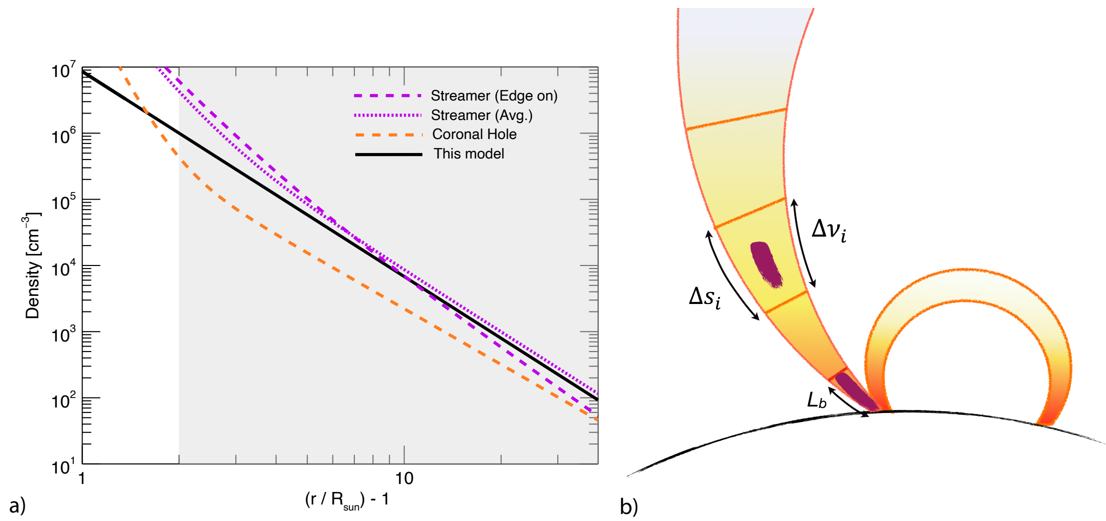

Figure 4.2 a) Density profile chosen for the flux tube model (solid black line) compared to the empirical densities of a coronal hole (orange dashed line) and helmet streamers in edge-on orientation (dashed purple line) and averaged (dotted purple line) [85]. b) Non-uniform $\Delta\nu_i$ bins corresponding to volume elements Δs_i in the open field compared with the beam length L_b.

Source: [36]

plotted for comparison. The coronal hole densities are shown by the orange dashed line. In contrast, the dotted and dashed purple lines represent the average densities and densities measured for edge-on orientation for helmet streamers, respectively [85]. Since the densities obtained from Equation (4.1) above do not agree well with the compared models at lower heights, we only consider density values for distances greater than 1 $R_\odot$ above the surface up to ≈ 40 $R_\odot$. This region is shown by the gray shaded area in Figure 4.2a. The plasma frequency, ν_p, is then determined as a function of distance r and interpolated to match the frequency grid sampled by LFR and HFR. Based on the chosen density model, only a subset of high frequencies ($1.27 - 9$ MHz) are included. Frequencies corresponding to LFR are sampled between $0.084 - 1.27$ MHz and combined with the former to make a unified grid. Given the non-uniform grid of RFS frequencies, the $\Delta\nu_i$ bins centered at frequency ν_i corresponding to volume Δs_i are also unequal along the modeled flux tube (see Figure 4.2b).

To simulate type III emission, some of the idealizations are adapted from MCL viz. the type III emission is generated instantaneously as the beam is expelled from the reconnection site and all electrons beams injected into the flux tube are assumed to have the same velocity. A detailed discussion of these assumptions is given in Chapter 3. Additionally, we assume that the flux tube expands between $1 - 40$ $R_\odot$, with an expansion factor proportional to the distance r and that the emissivity turns on, stays constant, then turns off, with the turnoff time being frequency dependent. Moreover, to mimic Langmuir wave decay, we implement a duration in the bursts that vary as a function of frequency. The empirical values of the duration T_d are obtained from a sample burst observed during encounter E02, that we fit to an exponential equation:

$$T_d = 1.153 \times 10^{10} (\nu^{-1.264}) \quad [\mathrm{s}] \tag{4.2}$$

As the flux tube expands radially, based on the initial duration of acceleration from the reconnection site (with a beam length L_b), the upward propagating beam either completely fills the volume elements ($\Delta s_i < L_b$, lower down in the flux tube) or partially fills them ($\Delta s_i > L_b$), as seen in Figure 4.2b. Similar to MCL, from the time the beam enters the volume element until the time the front of the beam exits, the intensity of the type III burst is proportional to the volume occupied by the beam within the volume element. From then on, based on the duration of the bursts at frequency ν_i, the intensity is proportional to the complete volume of the element. This is the time during which the emission persists due to Langmuir wave decay. A linear ramp up as the beam fills the volume and a ramp down as the Langmuir waves slowly decay is accounted for. Therefore, $I \propto \Delta s_i$ for volume segments lower down in the flux tube where $\Delta s_i < L_b$, and higher up where $\Delta s_i > L_b$, $I \propto L_b$ until the front of the beam exits the volume and $I \propto \Delta s_i$ for the remaining duration. The derivation of intensity dependence on the volume is shown in Appendix A; although, unlike MCL, the intensity in this model does not have a steep reliance on the density because of much smaller density gradients. In the next section, we will discuss some examples of features observed in the CCOPS computed for bright type IIIs as seen in the data in comparison with the CCOPS features from the model. This will help us build a better understanding of what shapes/patterns to look for during the analysis of the quiet periods.

Now, for a quantitative comparison between the data and the model, we require the intensity to be converted to flux density S as a function of frequency ν. Although there have been multiple studies that have performed sophisticated modeling to simulate type III bursts, to understand their observed properties better [see, for example, [149, 152, 153]]; all of these works invoke the energy density of the Langmuir waves to estimate the brightness temperature, T_b. Taking a more modest tack instead, we compute T_b for an isolated type III burst observed by the RFS, based on the measured flux density, and use these estimates as the basis to determine the flux densities in the modeled bursts. The power P of the observed burst can be converted to flux density using the following expression:

$$S_\nu = \frac{P - N}{Z_0(\Gamma L_{eff})^2} \quad [\mathrm{W\ m^{-2}\ Hz^{-1}}] \tag{4.3}$$

where $N = 2.2 \times 10^{-17}$ V^2 Hz^{-1} is the background noise that is subtracted from the measured power, $Z_0 = 377$ ohms is the impedance of free space, $\Gamma L_{eff} = 1.17$ m is the product of the capacitive gain factor and the antenna effective length [147].

Based on the radiative transfer equation, the expression for flux density S at frequency ν from a source is given as:

$$S_\nu = \frac{2kT_b\nu^2}{c^2}\, d\Omega \quad [\mathrm{W\ m^{-2}\ Hz^{-1}}] \tag{4.4}$$

where k is the Boltzmann constant and $d\Omega$ is the solid angle. It is reasonable to assume that a small-scale reconnection event on the Sun will have a size smaller than the beam-width of the instrument, and hence $d\Omega$ is the solid angle subtended by the source. Thus $d\Omega$ at each frequency bin $\Delta\nu_i$ is calculated based on the volume occupied by the electron beam and the width of the flux tube. Note that this approximation is more reliable for a flux tube observed at the limb; estimates for flux tubes on the disk will vary based on projection effects and line of sight integration. Finally, we calculate the flux density for an isolated burst observed during E02 from April 5, 2019, and obtain an estimate of the brightness temperature T_b using Equations (4.3), and 4.4 respectively. These estimates can then be employed to create a realistic flux density spectrum for the simulation. One limitation of using this approach when modeling multiple bursts is that any variations in the flux density as a function of frequency will always have the same intrinsic T_b profile with a frequency-independent multiplicative factor applied to match the observed flux density.

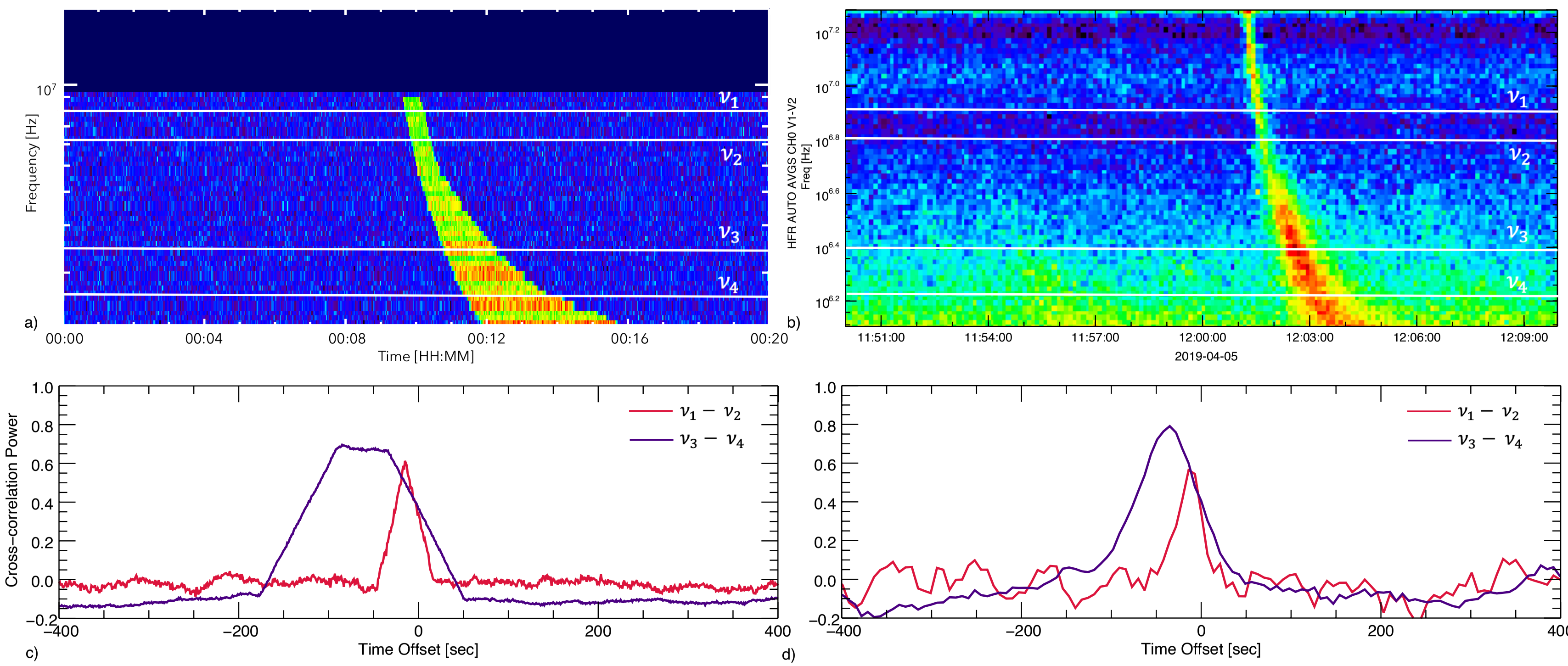

Figure 4.3 a) Simulated type III burst at the sample frequencies for HFR and LFR compared b) isolated type III burst from E02 used to create the modeled flux densities at HFR. The white solid lines show the two pairs of frequencies chosen to plot the CCOPS in each case (panels c and d).

Source: [36]

4.4 Results

With all the logistics for the model in place, we start by verifying the CCOPS signatures from the simulated emission for a single burst.

Single Burst Figure 4.3b shows the type III burst used to determine the T_b estimates produced by the HFR; panel a shows the modeled type III at frequencies sampled for HFR.

The corresponding CCOPS computed using the time-lag technique [183] are shown in panels c and d for the modeled and observed type III, respectively. The white solid lines overplotted on the dynamic spectra represent the pairs of frequencies for which the CCOPS are shown in panels c and d. As expected, the CCOPS predicted by the technique and the ones obtained from the observed burst show similar signatures. A broader peak for the frequency-pair $\nu_3 - \nu_4$ is expected due to the burst's increased duration. The plateau in the CCOPS for the pair $\nu_3 - \nu_4$ seen in panel c is just an effect of shorter ramp up and ramp down in the light curves than those in the data.

Paired Burst An interesting feature noticed in the observations from E02 is the presence of double bursts, i.e., two bursts occurring close together in time such that they show distinct spikes in the dynamic spectrum at higher frequencies but get blended together and appear as a single burst as their durations increase at lower frequencies. A comparison of the modeled bursts and the observations exhibiting such a feature and their corresponding CCOPS is shown in Figure 4.4.

Again, the CCOPS for frequency pair $\nu_3 - \nu_4$ in panels c and d are the same as seen in Figure 4.3. For the pair $\nu_1 - \nu_2$, we do see the main peak at the expected time-lag between the pair. The two additional peaks on the left and right are simply a manifestation of burst1 cross-correlating with burst2 peaking first at a negative offset and then at a positive offset. Their distance from the center of the main peak is defined by the time difference between the occurrence of the two bursts.

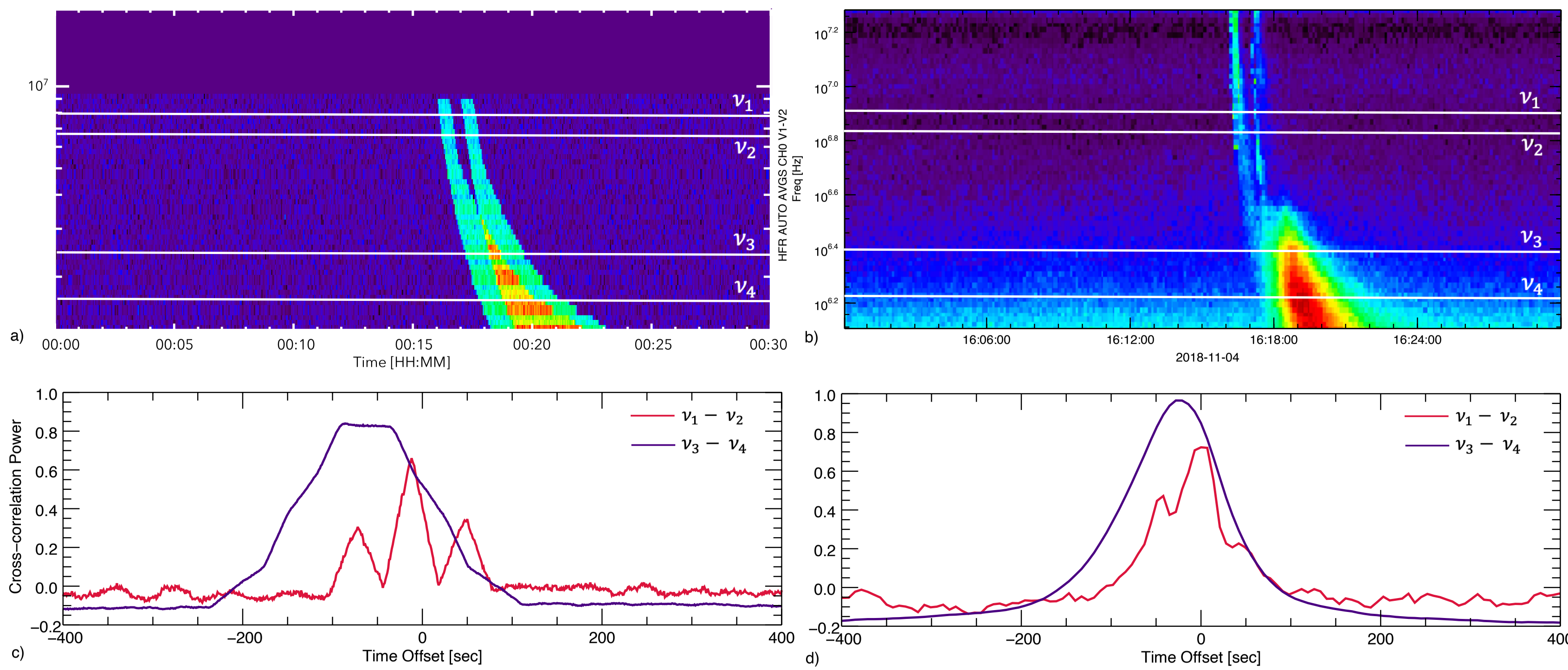

Figure 4.4 Same as Figure 4.3 for a pair of bursts observed during E01 that merge at low frequencies to look like a single burst.

Source: [36]

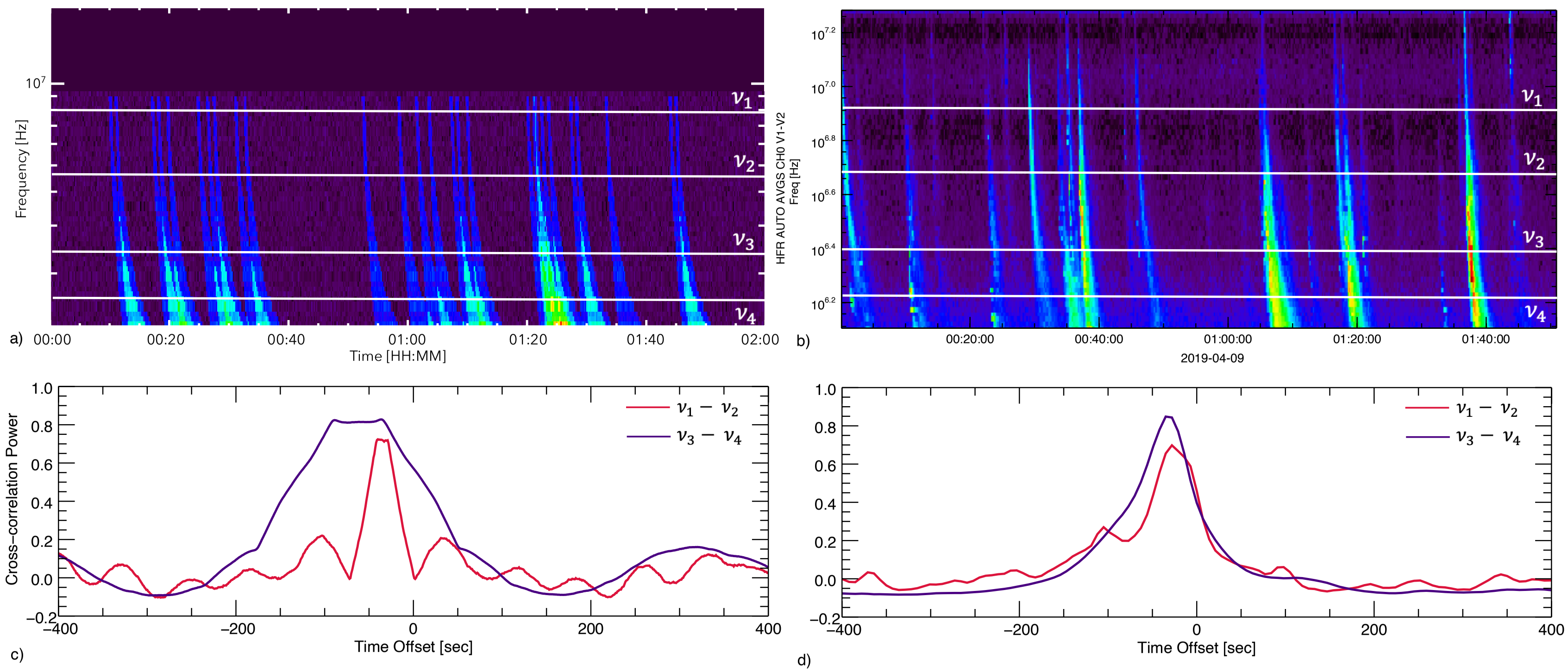

Figure 4.5 Same as Figure 4.3 for a type III storm observed during E02. The model tries to replicate the behaviour seen in the observations with a combination of paired bursts and single type IIIs to best predict the CCOPS.

Source: [36]

Type III storm We now look for patterns/signatures that may emerge in the CCOPS for a type III storm. The simulated emission, in this case, is based on the observations of the type III storm recorded during E02. Numerous type IIIs exhibiting the double-burst behavior discussed in the last example are observed during this time, along with some single bursts. Figure 4.5 shows the modeled and observed emission (panels a and b) along with the computed CCOPS. The model has been composed to include randomly generated bursts in time, but some have the double-burst behavior. The shapes of the CCOPS from the observations and the predicted CCOPS seen in panels c and d of Figure 4.5 again show similar trends. The additional tertiary and higher order peaks visible at very low power for the pair $\nu_1 - \nu_2$ can be explained by a more complex variant of the above example with multiple bursts cross-correlating with each other. The amplitude/power of these tertiary peaks will depend on the repetition frequency of such double/triple burst behavior.

4.4.1 Search for Type IIIs in Quiet Periods

Finally, we apply the findings from the previous examples to analyze data from a time where no activity is identified in the dynamic spectrum. This set of observations is chosen from E05. Figure 4.6a shows the HFR dynamic spectrum with six frequencies marked using solid black and white lines. The CCOPS between frequency pairs marked by the solid black lines are shown in the upper panel of the two plots in panel b. Although the signal is weaker here (likely due to high noise), compared to the previous examples, there is a nice succession in the CCOPS peaks as the separation between the frequency pairs increases. In contrast, the bottom panel showing the CCOPS between the pair $\nu_5 - \nu_6$ in the spectrum shows no correlation. This may be an indication of bursts present in the "haze" at lower frequencies. The emission from these bursts could so weak at higher frequencies that the noise completely dominates, resulting in the CCOPS with no correlation.

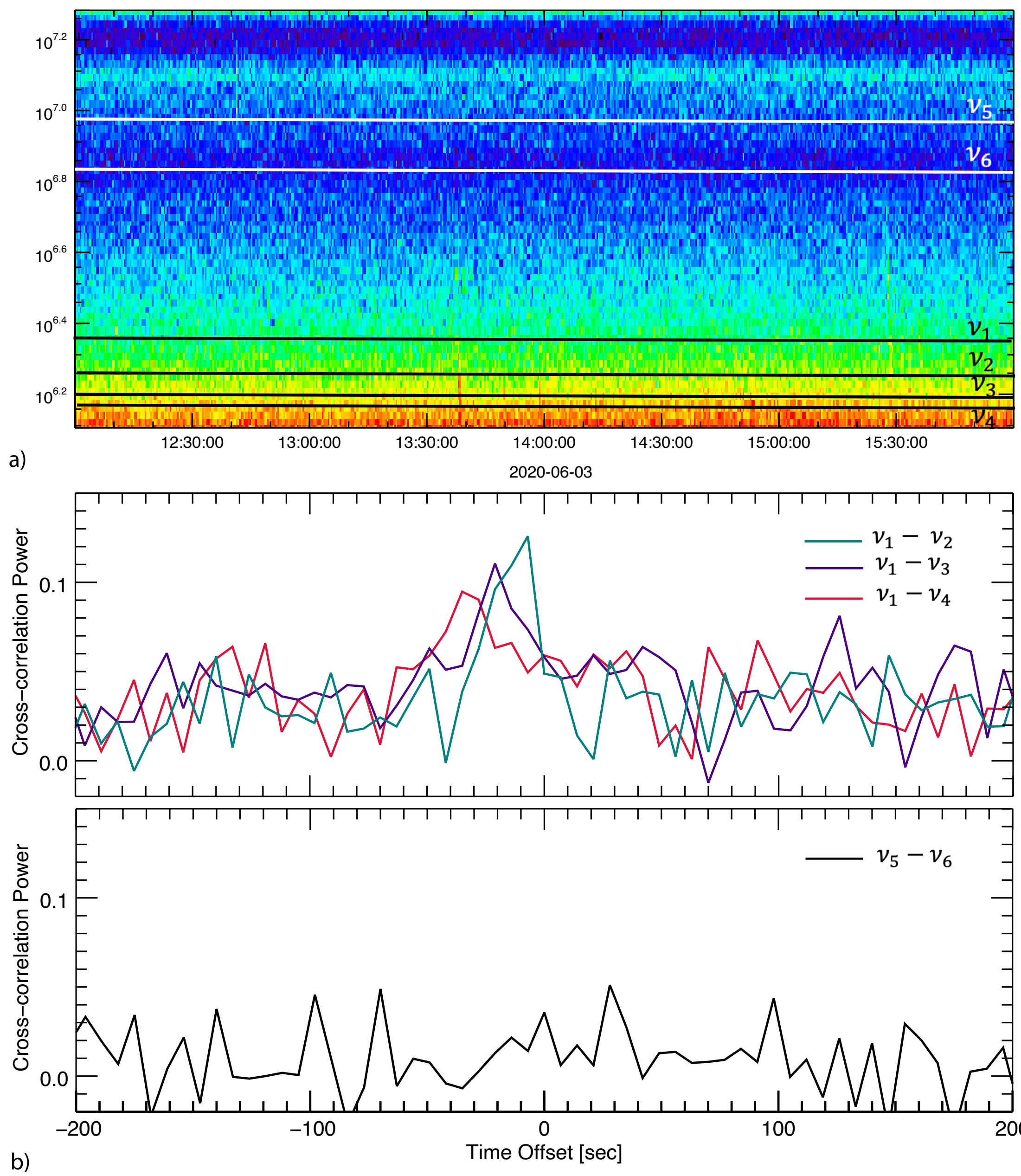

Figure 4.6 a) HFR dynamic spectrum from a quiet period during E05. b) CCOPS for four pairs of frequencies from the quiet time. Top panel shows three CCOPS for frequencies shown by solid black lines in the HFR dynamic spectrum exhibiting a successive increase in time-lag with an increase in frequency separation, and the bottom panel shows the CCOPS at higher frequencies marked by the solid white lines in the dynamic spectrum exhibiting no signs of cross-correlation. The successive delays at lower frequencies may be a plausible signature of type III emission embedded in the noise.

Source: [36]

4.5 Discussions

We look for evidence of energetic particles in the solar wind that could be produced by small-scale reconnection in the solar wind itself or reconnection in the lower corona, where particle beams escape on open field lines, for example, from interchange reconnection. It is claimed that there is a pervasive presence of current sheets in the solar wind [167, 17]. We expect reconnection to be common at these current sheets that separate the thin magnetic strands that make up the corona and solar wind, but whether it is efficient at accelerating particles is an open question.

To answer this question, we create a simple model that helps us identify the signatures of type III bursts in the solar wind that can be identified in the CCOPS created using the novel time-lag technique [183]. We then apply these findings to quiet-time data. Along with the idealized assumptions mentioned in Section 4.3, a limitation of this model is that we use a single density profile for all the flux tubes considered, resulting in all type IIIs having the same intensities as the beams escape along the open field. If beams propagate in tubes with different density profiles, the CCOPS will have peaks at multiple delays, just as is the case for loops in the magnetically closed corona. One important difference is that all the real peaks will be at negative delays. False peaks will occur equally at positive and negative delays. This opens the possibility of distinguishing between real and false peaks, which we will explore.

We present our preliminary analysis of radio observations recorded by the FIELDS instrument onboard the Parker Solar Probe during encounters E01-E05 that are compared with the features seen in the CCOPS created using our model. Since this is an ongoing investigation, most of the results presented here comprise the examples of bright type IIIs that are analyzed to learn what signatures can be used to confirm the presence of much weaker bursts in the quiet-times.

Interestingly, our analysis conducted during the “quiet” periods shows plausible signatures of type III bursts in the radio haze at lower frequencies sampled by the HFR. Although, the emission at higher frequencies appears to be dominated by noise. This could be an exciting catch, although we proceed further with caution. The obvious next step is to verify whether these signatures are real or produced by some artifact present in the data. We will divide the observed period into smaller parts and repeat the analysis. We also plan to look at multiple other quiet periods from the collected data to check what fraction of data returns positive outcomes.

Additionally, an effort to build a model that can replicate such emission is currently underway to corroborate the presence of such signatures in the CCOPS. If these signatures are seldom seen in the data, then getting a reliable measure of noise from the calibrated observations would be valuable. The estimated noise, added to the simulated emission, can be used to obtain a lower limit on the fraction of emission contribution from reconnection events required to show some signatures in the CCOPS.

CHAPTER 5

SUMMARY

This dissertation encompasses two sets of investigations: the first to understand the physical mechanisms responsible for radio emission in large-scale eruptive events; and the second to investigate fundamental processes such as particle acceleration and magnetic reconnection in small-scale impulsive events using radio emission that they may produce on the Sun and in the solar wind.

In Chapter 2 we present the first study which analyzes a complex radio event observed in association with a flare-CME from September 20, 2015. The flare-CME was recorded by OVRO-LWA during the first 24 hrs of commissioning observations taken during the expansion of the array in September 2015. This presented some limitations to the observations, such as the availability of a limited bandwidth (reduced to a little over 30% of the total), position offsets caused by a shift in the frequency channels, and unavailability of the polarization measurements. In addition to the radio observations from OVRO-LWA, data from LASCO-C2, EOVSA, WIND/WAVES, and RSTN were also utilized to place the radio emission in context with the emission seen at multiple wavelengths.

We find that the radio event was composed of multiple bursts, one of which exhibited outward motion which we classified as a type IVm burst. A comparison with LASCO observations of the WL-CME revealed that the outward motion was associated with the core of the CME, implying that particles trapped within the core emit radio emission as they are dragged outward with the CME. We performed a GCS reconstruction of the CME to constrain the density in the volume; however, our estimates were not low enough to rule plasma emission as the underlying mechanism for the type IVm. The smoothness of the emission in frequency and time and the source's lower height help us conclude that gyrosynchrotron may be the plausible mechanism. Spectral fitting techniques were then employed to fit gyrosynchrotron spectrum to the data and obtain the estimates of magnetic field strength, B that were found to be between 1-2 G and the power-law index δ exhibiting a range of 3.7-4.5. As the source expands with the outward moving CME, the field strength B decreases as would be expected. A comparison with the other studies that have attempted to estimate physical conditions in the plasma using similar techniques reveals that a wide range of B is observed, which may result from different conditions in the different observed events. Our estimates of δ lie well within the range of 3.5-5 reported by the other studies.

We also observed sporadic type III during the prephase and group type III bursts associated with the peak of the SXR flare. We believe the electrons may be excited during turbulent interactions between the flare and the remanant magnetic structure of a pre-existing CME. Despite the limitations, the observations from OVRO-LWA provided sufficient information for us to investigate a rarely-seen moving type IV burst and understand the physical conditions of the plasma during emission.

In the second study, we transition to investigating small-scale events. This work addresses the question of whether nanoflares accelerate energetic particles like full-sized flares. And if so, how efficiently? The goal demands a multifaceted approach that includes both modeling and analysis of radio observations from various high-resolution instruments. Chapter 3 presents the modeling effort that simulates radio emission in the form of type III bursts that may be produced by nanoflares. We expect that if present, type IIIs produced by the ubiquitous nanoflares will manifest as 'radio haze' in the dynamic spectra. Additionally, they will exhibit frequency drifts in both directions while propagating along closed loops. Utilizing the time-lag technique, our simple model examines the signatures of such type III bursts that can be identified in the CCOPS in the presence of numerous overlapping events.

We find that in the case of closed loops, the frequency spectrum of type III bursts is expected to be extremely steep such that significant emission is produced at a given frequency only for a rather narrow range of loop lengths. An important implication of this steep spectrum is that data from a wide bandwidth of frequencies need to be analyzed to understand the contribution of the type IIIs from different ranges of loop-lengths. We also find that the signature of bursts in the CCOPS diminishes as (1) the variety of participating loops within that range increases; (2) the occurrence rate of bursts increases; (3) the duration of bursts increases; and (4) the brightness of bursts decreases relative to noise. Nonetheless, we are able to identify an 'M'- shaped pattern that appears in the CCOPS as a result of nested peaks at time-lags from different loops and is best visible for closely separated frequencies. In addition, our model suggests a possible origin of type I bursts as a natural consequence of type III emission in a closed-loop geometry.

To look for similar signatures of type IIIs in the solar wind, we analyze radio observations from FIELDS/PSP, as discussed in Chapter 4. Observations from encounters E01-E05 are carefully examined, and a select few time-periods exhibiting different features are presented in our preliminary analysis. We build a simplistic model to replicate the features seen in the dynamic spectra during the five encounters and compare the computed CCOPS with those from the observations. Indeed, the patterns seen in the CCOPS are predicted well by our model and reveal different properties of the observed emission such as a presence of multiple collated bursts. We also show one example from encounter E05 where no activity can be identified in the spectrum by eye. The time-lag analysis of the time-period reveals plausible signatures of successive time-lags at lower frequencies which may come from type III bursts. Although, we proceed with caution to verify whether the observed signature is real or not.

5.1 Current Endeavors and Future Scope

This new era of advanced radio instruments capable of high-resolution imaging spectroscopy brings ample opportunities to investigate different physical mechanisms that conspire to produce radio emission on the Sun and in the inner heliosphere.

Although the acquired data from OVRO-LWA presented in Chapter 2 limited our investigation of the different bursts identified in the complex radio event, a second round of expansion of the OVRO-LWA instrument is now underway that will provide a 50% improvement in spatial resolution and include solar-dedicated observing modes specifically designed for solar science. This includes a solar-dedicated beam synthesized from its 256 core antennas to provide full spectral coverage of the total flux from the Sun at 1 ms time resolution, and a solar-dedicated pipeline-imaging mode that will correlate data from 48 more distant of its 352 antennas at a 100 ms cadence for high-resolution imaging spectroscopy in Stokes I and V. Slated for completion by 2021, this upgraded OVRO-LWA instrument will provide a powerful new tool to study meter-wavelength emission of both bursts and the quiet Sun during the coming solar cycle.

Based on the positive findings of the modeling effort from Chapter 3, the obvious next step is to look at high-resolution radio observations from ground-based radio interferometers. We are currently collecting data from VLA, LOFAR, and LWA to ensure coverage over a wide bandwidth and different periods. The idea is to look for the presence of patterns in CCOPS identified from the model or lack thereof at a wide band of radio frequencies. We have explored multiple scenarios in the model, but of course, we expect that any number of variations in the signatures identified can be present in the data. A positive outcome in any capacity will give us an idea about the efficiency of particle acceleration from nanoflares. It will be interesting to see if the activity identified by the technique shows any association with the presence/absence of active regions on the disk or the age of active regions. A negative outcome could be due to a high level of noise in the instruments that dominates the highly sensitive emission from type IIIs produced by mildly-energetic bursts. In this case, it would be useful to get a lower limit on the brightness of nanoflares that may produce type III emission above the noise level. Another explanation for a negative outcome is that nanoflares are not efficient at accelerating particles, in which case it will be a step forward in confirming the role of the guide field in the theory of particle acceleration. Eventually, we plan to hone the technique to create an automated process for detecting type III activity during quiet as well as active periods.

The work presented in Chapter 4 is ongoing, looking for signatures of type IIIs during quiet times. Only a fraction of the collected data has been analyzed so far. We plan to go through observations from all the PSP encounters and systematically analyze them using the time-lag technique. Some of the capabilities that we would particularly like to explore include: testing whether the CCOPS can shed light on the energy(velocity) of the particles from different bursts, i.e., whether two different bursts have different energies based on their measured frequency drifts, the range of these energies, etc. The automation of the technique mentioned above will also be used to build statistics from type III activity in the solar wind.

Appendix A

TYPE III INTENSITY VARIATION

Under the assumption that the intensity, I for a constant frequency bin $\Delta\nu$ along the loop is directly proportional to the volume Δs that the particles traverse, we have:

$$I \propto \Delta s = \frac{\Delta n}{dn/ds} \tag{A.1}$$

where Δn is the density bin corresponding to the frequency bin $\Delta\nu$.

The plasma frequency, $\nu \propto n^{1/2}$, which gives us:

$$\begin{aligned} \Delta\nu &= \frac{d\nu}{dn}\Delta n \\ &\propto \frac{1}{2}n^{-1/2}\Delta n \\ &\propto \frac{1}{2}\nu^{-1}\Delta n \end{aligned} \tag{A.2}$$

$$\Rightarrow \Delta n \propto 2\nu\Delta\nu \tag{A.3}$$

$$I \propto 2\nu \left(\frac{dn}{ds}\right)^{-1} \Delta\nu \tag{A.4}$$

Note that, as mentioned in Subsection 3.2.2, this relation is true for all frequencies ν_i for which their respective volume element is smaller than the beam length, i.e. $\Delta s_i < L_b$. For any element $\Delta s_i > L_b$, the intensity, I is directly proportional to the beam length, L_b. The intensity thus calculated is used to create the light curves for each frequency based on their position along the loop. To visualize the above relation better, let us look at it in terms of temperature, T along the loop. From Equation

(A.4) we have,

$$\begin{aligned} I &\propto \nu \left(\frac{dn}{ds}\right)^{-1} \\ &\propto n^{1/2} \left(\frac{dn}{ds}\right)^{-1} \end{aligned} \tag{A.5}$$

For a static loop with constant conduction flux F_c

$$\begin{aligned} F_c &\propto T^{5/2} \left(\frac{dT}{ds}\right) \\ &\propto T^{5/2} \frac{d}{ds} \left(\frac{P}{n}\right) \\ &\propto T^{5/2} \left(-\frac{1}{n^2}\right) \frac{dn}{ds} \end{aligned} \tag{A.6}$$

assuming constant pressure along the loop.

$$\Rightarrow \frac{dn}{ds} \propto T^{-5/2} n^2 \tag{A.7}$$

Substituting this back in Equation (A.5), we get

$$\begin{aligned} I &\propto T^{5/2}\, n^{-2}\, n^{1/2} \\ &\propto T^{5/2}\, T^{2}\, T^{-1/2} \end{aligned} \tag{A.8}$$

$$\Rightarrow I \propto T^4 \propto n^{-4} \propto \nu^{-8} \tag{A.9}$$

The above equations clearly exhibits the precipitous fall in intensity I as the density n increases downward along the loop and the T decreases.

Appendix B

FACTORS AFFECTING THE CCOP

The basis of the time-lag technique [183, 185] is to compute the cross-correlation between a pair of light curves for two different channels as a function of imposed temporal offset, l. For some studies, such as the cooling of nanoflare-heated loops, only the lag of maximum correlation is important. For the purpose of this study, we are interested in the complete spectrum of cross-correlation power. The Equation used to calculate the cross-correlation power, P for a negative lag is given as:

$$P(l < 0) = \frac{\sum_{k=0}^{N-|l|-1}(x_{k+|l|} - \bar{x})(y_k - \bar{y})}{\sqrt{\sum_{k=0}^{N-1}(x_k - \bar{x})^2 \sum_{k=0}^{N-1}(y_k - \bar{y})^2}} \tag{B.1}$$

For a positive lag,

$$P(l > 0) = \frac{\sum_{k=0}^{N-l-1}(x_k - \bar{x})(y_{k+l} - \bar{y})}{\sqrt{\sum_{k=0}^{N-1}(x_k - \bar{x})^2 \sum_{k=0}^{N-1}(y_k - \bar{y})^2}} \tag{B.2}$$

where x_k and y_k are the intensities in the chosen frequencies at time k, $\bar{x}$ and $\bar{y}$ are the means of the intensity light curves for x and y respectively, and N is the number of data points in the light curves.

Now, following from Equations (B.1) and (B.2) note that the product of deviations from the mean, i.e. $(x_i - \bar{x})(y_i - \bar{y})$ will be positive only when x_i and y_i both lie on the same side of their respective means. Therefore, if x_i and y_i are simultaneously greater or less than their respective means, the cross-correlation power $P(l)$ will be positive, and if one is greater while the other is less, the power will be negative. While summing over the product for all data points, the negative products will contribute in reducing the power of the cross-correlation. This effect is quite

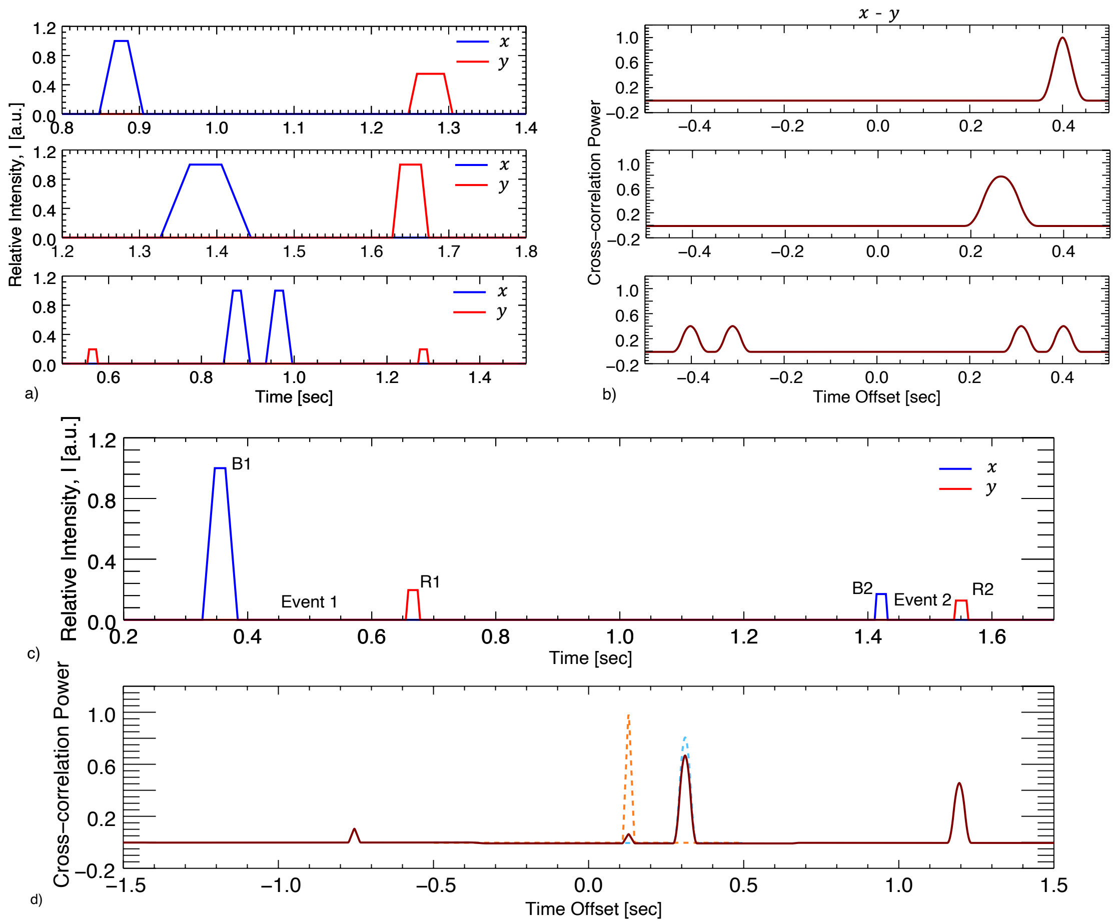

Figure B.1 a) Light curves for two frequencies x and y overlaid on one plot for three different scenarios; Top: The event has the same duration but differs in intensity for the two frequencies, Middle: the event has same intensities but different durations and, Bottom: Both intensities and durations differ, but now two peaks are present at each frequency as the particles move in both directions (same as Case C in Subsection 3.2.3). b) CCOPS corresponding to each scenario from a). c) Light curves for frequencies x and y overlaid on one plot showing two events, Event 1 and Event 2, on different loops (with electron beams moving downward only). d) CCOPS corresponding to then scenario from c). The overlaid dashed line shows individual CCOPS for Event 1 in the absence of Event 2 and vice versa.

Source: [35].

apparent from the Equations above. However, additional factors such as the duration and number of the bursts also affect the power of the cross-correlation.

Let us consider example light-curves for x and y as shown in Figure B.1a. Each panel in the plot represents a key difference between the light curves. In the top-most panel, the two light curves vary in intensity but the duration of the bursts is exactly the same. In the middle panel, the duration varies but intensities are the same, and in the bottom panel, along with the variation in intensity and duration, we introduce emission in two places. The last case is very similar to the one seen in Case C from Subsection 3.2.3 (particles moving in both directions). To compute the CCOP, imagine moving one of the light curves with respect to the other until their centers are perfectly aligned and then moving away in the opposite direction. As the peaks in the light-curves start overlapping, the power of the cross-correlation increases until it reaches a maximum when their centers are perfectly aligned and then reduces again.

Figure B.1b shows the CCOPS corresponding to each panel in B.1a. For the top panel, the maximum power of the cross-correlation is unity at the time-difference required to perfectly align the two light-curves. Their difference in intensity does not affect the CCOP. To see this, imagine that one of the peaks becomes enhanced. The deviation from the mean is then larger throughout the light curve. It is positive and substantially larger at the location of the peak, and it is negative and minimally larger outside the peak. The net effect is no change in the CCOP.

In the middle panel, the maximum power never reaches one. This is simply due to the different durations of bursts in the two light curves, even when they are centered one above the other. Also note that the width of the cross correlation curve is equal to the sum of the burst durations in the two frequencies. Finally, in the bottom panel, the maximum power for each time-lag has become much smaller. As one intensity peak in x is centered above one of the peaks on y, the misalignment in the other peaks of the light-curves further reduces the power in addition to the different durations.

Lastly, panel B.1c shows light curves for frequencies x and y for two events. Each event occurs in a different loop and the particles only move downward. The physically interesting correlations are those between peaks of the same event, i.e. $B1$ with $R1$, and $B2$ with $R2$. Correlations of one burst with another, i.e. $B1$ with $R2$ and $B2$ with $R1$, also exist but are what we term "false" peaks. The corresponding CCOPS (solid line) in panel d also have the dashed line overlaid showing individual CCOPS for Event 1 (cyan) in the absence of Event 2 and vice versa (orange). The CCOPS (solid line) show two important implications of the presence of multiple bursts in the light curves:

1. Contrary to the first example (top panel) in panel a), the high intensity from event 1 in x will shift the mean $\bar{x}$ such that the faint peak $B2$ in x will have a smaller positive deviation from the mean. Consequently, the CCOPS will now be affected by the difference in intensity between the two events. The CCOPS peak at $\sim$ 0.31 s with the highest power corresponds to a cross-correlation between $B1$ and $R1$. Note that its magnitude is lower than it would have been in the absence of Event 2. Also note that the power of cross-correlation between$B2$ and $R2$ at an offset of $\sim$ 0.22 s is far smaller than its unity value in the absence of Event 1.
2. The second brightest peak in the CCOP, at a time offset of $\sim$ 1.2 s, corresponds to a cross-correlation between $B1$ and $R2$, i.e. events from two different loops, and hence is a "false" peak. The second false peak at the offset of ~ -0.75 s from $R1$ and $B2$ also has a small power due to the reason mentioned in the previous point.

This tells us that the CCOP in the presence of multiple bursts will be affected by the dominant intensity peaks in the light curves as they skew the value of mean; and that the same dominant peaks are also responsible for a high CCOP at false time–lags. This effect is enhanced with an increase in the burst frequency.

REFERENCES

[1] H. Alfvén. On the solar corona. *Arkiv för matematik, astronomi och fysik*, 27 A(25):1–23, 1941.

[2] H. Alfvén. Magneto hydrodynamic waves, and the heating of the solar corona. *Monthly Notices of the Royal Astronomical Society*, 107:211, January 1947.

[3] C. W. Allen. Solar Radio-Noise of 200 Mc. /s. and its relation to Solar Observations. *Monthly Notices of the Royal Astronomical Society*, 107:386, January 1947.

[4] M. M. Anderson, G. Hallinan, M. W. Eastwood, R. M. Monroe, T. A. Callister, J. Dowell, B. Hicks, Y. Huang, N. E. Kassim, J. Kocz, T. J. W. Lazio, D. C. Price, F. K. Schinzel, and G. B. Taylor. New Limits on the Low-frequency Radio Transient Sky Using 31 hr of All-sky Data with the OVRO-LWA. *The Astrophysical Journal*, 886(2):123, December 2019.

[5] M. M. Anderson, G. Hallinan, M. W. Eastwood, R. M. Monroe, H. K. Vedantham, S. Bourke, L. J. Greenhill, J. Kocz, T. J. W. Lazio, D. C. Price, F. K. Schinzel, Y. Wang, and D. P. Woody. A Simultaneous Search for Prompt Radio Emission Associated with the Short GRB 170112A Using the All-sky Imaging Capability of the OVRO-LWA. *The Astrophysical Journal*, 864(1):22, September 2018.

[6] K. Arzner and A. O. Benz. Temporal Correlation of Hard X-Rays and Meter/Decimeter Radio Structures in Solar Flares. *Solar Physics*, 231(1-2):117–141, September 2005.

[7] M. J. Aschwanden. *Physics of the Solar Corona. An Introduction.* Chichester, UK: Springer-Verlag Berlin Heidelberg, 2004.

[8] H. M. Bain, S. Krucker, P. Saint-Hilaire, and C. L. Raftery. Radio Imaging of a Type IVM Radio Burst on the 14th of August 2010. *The Astrophysical Journal*, 782(1):43, February 2014.

[9] S. D. Bale, K. Goetz, P. R. Harvey, P. Turin, J. W. Bonnell, T. Dudok de Wit, R. E. Ergun, R. J. MacDowall, M. Pulupa, M. Andre, M. Bolton, J. L. Bougeret, T. A. Bowen, D. Burgess, C. A. Cattell, B. D. G. Chandran, C. C. Chaston, C. H. K. Chen, M. K. Choi, J. E. Connerney, S. Cranmer, M. Diaz-Aguado, W. Donakowski, J. F. Drake, W. M. Farrell, P. Fergeau, J. Fermin, J. Fischer, N. Fox, D. Glaser, M. Goldstein, D. Gordon, E. Hanson, S. E. Harris, L. M. Hayes, J. J. Hinze, J. V. Hollweg, T. S. Horbury, R. A. Howard, V. Hoxie, G. Jannet, M. Karlsson, J. C. Kasper, P. J. Kellogg, M. Kien, J. A. Klimchuk, V. V. Krasnoselskikh, S. Krucker, J. J. Lynch, M. Maksimovic, D. M. Malaspina, S. Marker, P. Martin, J. Martinez-Oliveros, J. McCauley, D. J. McComas, T. McDonald, N. Meyer-Vernet, M. Moncuquet, S. J. Monson, F. S. Mozer, S. D. Murphy, J. Odom, R. Oliverson, J. Olson, E. N. Parker, D. Pankow, T. Phan, E. Quataert, T. Quinn, S. W. Ruplin, C. Salem, D. Seitz, D. A. Sheppard, A. Siy, K. Stevens, D. Summers, A. Szabo, M. Timofeeva, A. Vaivads, M. Velli, A. Yehle, D. Werthimer, and J. R. Wygant. The FIELDS Instrument Suite for Solar Probe Plus. Measuring the Coronal Plasma and Magnetic Field, Plasma Waves and Turbulence, and Radio Signatures of Solar Transients. *Space Science Reviews*, 204(1-4):49–82, December 2016.

[10] W. T. Barnes, S. J. Bradshaw, and N. M. Viall. Understanding Heating in Active Region Cores through Machine Learning. I. Numerical Modeling and Predicted Observables. *The Astrophysical Journal*, 880(1):56, July 2019.

[11] T. S. Bastian, M. Pick, A. Kerdraon, D. Maia, and A. Vourlidas. The Coronal Mass Ejection of 1998 April 20: Direct Imaging at Radio Wavelengths. *The Astrophysical Journal Letters*, 558(1):L65–L69, September 2001.

[12] A. O. Benz. Electron trapping in the solar magnetic field and emission of decimetric continuum radio bursts. *The Astrophysical Journal*, 240:892–907, September 1980.

[13] A. O. Benz. Flare Observations. *Living Reviews in Solar Physics*, 5(1):1, December 2008.

[14] A. O. Benz, C. Monstein, M. Beverland, H. Meyer, and B. Stuber. High Spectral Resolution Observation of Decimetric Radio Spikes Emitted by Solar Flares - First Results of the Phoenix-3 Spectrometer. *Solar Physics*, 260(2):375–388, December 2009.

[15] P. Boerner, C. Edwards, J. Lemen, A. Rausch, C. Schrijver, R. Shine, L. Shing, R. Stern, T. Tarbell, A. Title, C. J. Wolfson, R. Soufli, E. Spiller, E. Gullikson, D. McKenzie, D. Windt, L. Golub, W. Podgorski, P. Testa, and M. Weber. Initial Calibration of the Atmospheric Imaging Assembly (AIA) on the Solar Dynamics Observatory (SDO). *Solar Physics*, 275(1-2):41–66, January 2012.

[16] A. Boischot. Caractères d'un type d'émission hertzienne associé à certaines éruptions chromosphériques. *Academie des Sciences Paris Comptes Rendus*, 244:1326–1329, January 1957.

[17] J. E. Borovsky. Flux tube texture of the solar wind: Strands of the magnetic carpet at 1 AU? *Journal of Geophysical Research (Space Physics)*, 113(A8):A08110, August 2008.

[18] J. L. Bougeret. High Resolution Space-Time Structure and Centre-Limb Distribution of Solar Type I Sources Observed at 169 MHz. *Astronomy & Astrophysics*, 24:53, April 1973.

[19] J. L. Bougeret, M. L. Kaiser, P. J. Kellogg, R. Manning, K. Goetz, S. J. Monson, N. Monge, L. Friel, C. A. Meetre, C. Perche, L. Sitruk, and S. Hoang. Waves: The Radio and Plasma Wave Investigation on the Wind Spacecraft. *Space Science Reviews*, 71(1-4):231–263, February 1995.

[20] S. J. Bradshaw and J. A. Klimchuk. What Dominates the Coronal Emission Spectrum During the Cycle of Impulsive Heating and Cooling? *The Astrophysical Journal Supplement Series*, 194(2):26, June 2011.

[21] S. J. Bradshaw, J. A. Klimchuk, and J. W. Reep. Diagnosing the Time-dependence of Active Region Core Heating from the Emission Measure. I. Low-frequency Nanoflares. *The Astrophysical Journal*, 758(1):53, October 2012.

[22] G. E. Brueckner, R. A. Howard, M. J. Koomen, C. M. Korendyke, D. J. Michels, J. D. Moses, D. G. Socker, K. P. Dere, P. L. Lamy, A. Llebaria, M. V. Bout, R. Schwenn, G. M. Simnett, D. K. Bedford, and C. J. Eyles. The Large Angle Spectroscopic Coronagraph (LASCO). *Solar Physics*, 162(1-2):357–402, December 1995.

[23] B. F. Burke and K. L. Franklin. Observations of a Variable Radio Source Associated with the Planet Jupiter. *Journal of Geophysical Research: Space Physics*, 60(2):213–217, June 1955.

[24] I. H. Cairns, V. V. Lobzin, A. Donea, S. J. Tingay, P. I. McCauley, D. Oberoi, R. T. Duffin, M. J. Reiner, N. Hurley-Walker, N. A. Kudryavtseva, D. B. Melrose, J. C. Harding, G. Bernardi, J. D. Bowman, R. J. Cappallo, B. E. Corey, A. Deshpande, D. Emrich, R. Goeke, B. J. Hazelton, M. Johnston-Hollitt, D. L. Kaplan, J. C. Kasper, E. Kratzenberg, C. J. Lonsdale, M. J. Lynch, S. R. McWhirter, D. A. Mitchell, M. F. Morales, E. Morgan, S. M. Ord, T. Prabu, A. Roshi, N. Udaya Shankar, K. S. Srivani, R. Subrahmanyan, R. B. Wayth, M. Waterson, R. L. Webster, A. R. Whitney, A. Williams, and C. L. Williams. Low Altitude Solar Magnetic Reconnection, Type III Solar Radio Bursts, and X-ray Emissions. *Scientific Reports*, 8:1676, January 2018.

[25] I. H. Cairns and R. D. Robinson. Herringbone bursts associated with type II solar radio emission. *Solar Physics*, 111(2):365–383, September 1987.

[26] H. V. Cane. Coronal and interplanetary Type 2 radio emission. In S. T. Wu, editor, *Physical Interpretation of Solar/Interplanetary and Cometary Intervals*, page 25. Alabama University, Huntsville: STIP Symposium, September 1987.

[27] H. V. Cane, R. G. Stone, J. Fainberg, R. T. Stewart, J. L. Steinberg, and S. Hoang. Radio evidence for shock acceleration of electrons in the solar corona. *Geophysical Research Letters*, 8(12):1285–1288, December 1981.

[28] P. J. Cargill. Active Region Emission Measure Distributions and Implications for Nanoflare Heating. *The Astrophysical Journal*, 784(1):49, March 2014.

[29] E. P. Carley, N. Vilmer, P. J. A. Simões, and B. Ó Fearraigh. Estimation of a coronal mass ejection magnetic field strength using radio observations of gyrosynchrotron radiation. *Astronomy & Astrophysics*, 608:A137, December 2017.

[30] H. Carmichael. *A Process for Flares*, volume 50, page 451. Washington, DC: NASA, STID, 1964.

[31] R. C. Carrington. Description of a Singular Appearance seen in the Sun on September 1, 1859. *Monthly Notices of the Royal Astronomical Society*, 20(1):13–15, 11 1859.

[32] B. Chen, T. S. Bastian, S. M. White, D. E. Gary, R. Perley, M. Rupen, and B. Carlson. Tracing Electron Beams in the Sun's Corona with Radio Dynamic Imaging Spectroscopy. *The Astrophysical Journal Letters*, 763(1):L21, January 2013.

[33] B. Chen, S. Yu, M. Battaglia, S. Farid, A. Savcheva, K. K. Reeves, S. Krucker, T. S. Bastian, F. Guo, and S. Tassev. Magnetic Reconnection Null Points as the Origin of Semirelativistic Electron Beams in a Solar Jet. *The Astrophysical Journal*, 866(1):62, October 2018.

[34] S. Chhabra, D. E. Gary, G. Hallinan, M. M. Anderson, B. Chen, L. J. Greenhill, and D. C. Price. Imaging Spectroscopy of CME-associated Solar Radio Bursts using OVRO-LWA. *The Astrophysical Journal*, 906(2):132, January 2021.

[35] S. Chhabra, J. A. Klimchuk, and D. E. Gary. Signatures of Type III Solar Radio Bursts from Nanoflares: Modeling. *Submitted to The Astrophysical Journal*, 2021.

[36] S. Chhabra, J. A. Klimchuk, D. E. Gary, and the PSP/FIELDS Team. Signatures of Type III Radio Bursts in the Solar Wind from Small-scale Reconnection Events. *In Preperation*, 2021.

[37] K. S. Cho, J. Lee, Y. J. Moon, M. Dryer, S. C. Bong, Y. H. Kim, and Y. D. Park. A study of CME and type II shock kinematics based on coronal density measurement. *Astronomy & Astrophysics*, 461(3):1121–1125, January 2007.

[38] E. W. Cliver, D.F. Webb, and R. A. Howard. On the origin of solar metric type II bursts. *Solar Physics*, 187(1):89–114, June 1999.

[39] A. E. Covington. Solar noise observations on 10.7 cms. *Proceedings of the IRE*, 36:454, April 1948.

[40] A. E. Covington. Some Characteristics of 10.7-centimetre Solar Noise, I. *Journal of the Royal Astronomical Society of Canada*, 45:15, February 1951.

[41] P. C. Crane and P. J. Napier. Sensitivity. In Richard A. Perley, Frederic R. Schwab, and Alan H. Bridle, editors, *Synthesis Imaging in Radio Astronomy*, volume 6 of *Astronomical Society of the Pacific Conference Series*, page 139. San Francisco, CA: Astronomical Society of the Pacific, January 1989.

[42] H. Cremades, V. Bothmer, and D. Tripathi. Properties of structured coronal mass ejections in solar cycle 23. *Advances in Space Research*, 38(3):461–465, January 2006.

[43] J. T. Dahlin, J. F. Drake, and M. Swisdak. Electron acceleration in three-dimensional magnetic reconnection with a guide field. *Physics of Plasmas*, 22(10):100704, October 2015.

[44] G. Daigne. Structure and Movement of Solar Noise Storms. *Nature*, 220(5167):567–568, November 1968.

[45] I. De Moortel and V. M. Nakariakov. Magnetohydrodynamic waves and coronal seismology: an overview of recent results. *Philosophical Transactions of the Royal Society of London Series A*, 370(1970):3193–3216, July 2012.

[46] B. De Pontieu, S. W. McIntosh, M. Carlsson, V. H. Hansteen, T. D. Tarbell, P. Boerner, J. Martinez-Sykora, C. J. Schrijver, and A. M. Title. The Origins of Hot Plasma in the Solar Corona. *Science*, 331(6013):55, January 2011.

[47] G. Del Zanna, G. Aulanier, K. L. Klein, and T. Török. A single picture for solar coronal outflows and radio noise storms. *Astronomy & Astrophysics*, 526:A137, February 2011.

[48] G. Del Zanna, D. Tripathi, H. Mason, S. Subramanian, and B. O'Dwyer. The evolution of the emission measure distribution in the core of an active region. *Astronomy & Astrophysics*, 573:A104, January 2015.

[49] K. P. Dere, G. E. Brueckner, R. A. Howard, M. J. Koomen, C. M. Korendyke, R. W. Kreplin, D. J. Michels, J. D. Moses, N. E. Moulton, D. G. Socker, O. C. St. Cyr, J. P. Delaboudinière, G. E. Artzner, J. Brunaud, A. H. Gabriel, J. F. Hochedez, F. Millier, X. Y. Song, J. P. Chauvineau, J. P. Marioge, J. M. Defise, C. Jamar, P. Rochus, R. C. Catura, J. R. Lemen, J. B. Gurman, W. Neupert, F. Clette, P. Cugnon, E. L. van Dessel, P. L. Lamy, A. Llebaria, R. Schwenn, and G. M. Simnett. EIT and LASCO Observations of the Initiation of a Coronal Mass Ejection. *Solar Physics*, 175(2):601–612, October 1997.

[50] V. Domingo, B. Fleck, and A. I. Poland. The SOHO Mission: an Overview. *Solar Physics*, 162(1-2):1–37, December 1995.

[51] J. F. Drake, M. Swisdak, H. Che, and M. A. Shay. Electron acceleration from contracting magnetic islands during reconnection. *Nature*, 443(7111):553–556, October 2006.

[52] G. A. Dulk. Radio emission from the sun and stars. *Annual Review of Astronomy and Astrophysics*, 23:169–224, January 1985.

[53] G. A. Dulk, D. E. Gary, and S. Suzuki. The position and polarization of Type V solar bursts. *Astronomy & Astrophysics*, 88(1-2):218–229, August 1980.

[54] G. A. Dulk, Y. Leblanc, T. S. Bastian, and J.-L. Bougeret. Acceleration of electrons at type II shock fronts and production of shock-accelerated type III bursts. *Journal of Geophysical Research: Space Physics*, 105(A12):27343–27352, December 2000.

[55] G. A. Dulk and K. A. Marsh. Simplified expressions for the gyrosynchrotron radiation from mildly relativistic, nonthermal and thermal electrons. *The Astrophysical Journal*, 259:350–358, August 1982.

[56] G. A. Dulk and S. Suzuki. The position and polarization of Type III solar bursts. *Astronomy & Astrophysics*, 88(1-2):203–217, August 1980.

[57] M. W. Eastwood, M. M. Anderson, R. M. Monroe, G. Hallinan, B. R. Barsdell, S. A. Bourke, M. A. Clark, S. W. Ellingson, J. Dowell, H. Garsden, L. J. Greenhill, J. M. Hartman, J. Kocz, T. J. W. Lazio, D. C. Price, F. K. Schinzel, G. B. Taylor, H. K. Vedantham, Y. Wang, and D. P. Woody. The Radio Sky at Meter Wavelengths: m-mode Analysis Imaging with the OVRO-LWA. *The Astronomical Journal*, 156(1):32, July 2018.

[58] W. Eastwood, M, M. M. Anderson, R. M. Monroe, G. Hallinan, M. Catha, J. Dowell, H. Garsden, L. J. Greenhill, B. C. Hicks, J. Kocz, D. C. Price, F. K. Schinzel, H. Vedantham, and Y. Wang. The 21 cm Power Spectrum from the Cosmic Dawn: First Results from the OVRO-LWA. *The Astronomical Journal*, 158(2):84, August 2019.

[59] B. Edlén. Die Deutung der Emissionslinien im Spektrum der Sonnenkorona. Mit 6 Abbildungen. *Zeitschrift für Astrophysik*, 22:30, January 1943.

[60] E. Ø. Elgarøy. *Solar noise storms.* International Series in Natural Philosophy, Oxford, UK: Pergamon Press, 1977.

[61] G. D. Fleishman and A. A. Kuznetsov. Fast Gyrosynchrotron Codes. *The Astrophysical Journal*, 721(2):1127–1141, October 2010.

[62] G. D. Fleishman and V. F. Melnikov. Optically Thick Gyrosynchrotron Emission from Anisotropic Electron Distributions. *The Astrophysical Journal*, 584(2):1071–1083, February 2003.

[63] J. M. Fontenla, E. H. Avrett, and R. Loeser. Energy Balance in the Solar Transition Region. I. Hydrostatic Thermal Models with Ambipolar Diffusion. *The Astrophysical Journal*, 355:700, June 1990.

[64] T. G. Forbes and L. W. Acton. Reconnection and Field Line Shrinkage in Solar Flares. *The Astrophysical Journal*, 459:330, March 1996.

[65] P. Foukal. Extension of the F10.7 Index to 1905 using Mt. Wilson Ca K Spectroheliograms. *Geophysical Research Letters*, 25(15):2909–2912, January 1998.

[66] N. J. Fox, M. C. Velli, S. D. Bale, R. Decker, A. Driesman, R. A. Howard, J. C. Kasper, J. Kinnison, M. Kusterer, D. Lario, M. K. Lockwood, D. J. McComas, N. E. Raouafi, and A. Szabo. The Solar Probe Plus Mission: Humanity's First Visit to Our Star. *Space Science Reviews*, 204(1-4):7–48, December 2016.

[67] A. H. Gabriel. A Magnetic Model of the Solar Transition Region. *Philosophical Transactions of the Royal Society of London Series A*, 281(1304):339–352, May 1976.

[68] D. E. Gary, B. Chen, B. R. Dennis, G. D. Fleishman, G. J. Hurford, S. Krucker, J. M. McTiernan, G.M. Nita, A.Y. Shih, S. M. White, and S. Yu. Microwave and Hard X-Ray Observations of the 2017 September 10 Solar Limb Flare. *The Astrophysical Journal*, 863(1):83, August 2018.

[69] D. E. Gary, G. A. Dulk, L. L. House, R. Illing, W. J. Wagner, and D. J. Mclean. The type IV burst of 1980 June 29, 0233 UT - Harmonic plasma emission? *Astronomy & Astrophysics*, 152:42–50, November 1985.

[70] D. E. Gary and G. J. Hurford. Coronal Temperature, Density, and Magnetic Field Maps of a Solar Active Region Using the Owens Valley Solar Array. *The Astrophysical Journal*, 420:903, January 1994.

[71] D. E. Gary, G. J. Hurford, G. M. Nita, S. M. White, J. McTiernan, and G. D. Fleishman. The Expanded Owens Valley Solar Array (EOVSA). In *American Astronomical Society Meeting Abstracts #224*, volume 224, page 123, June 2014.

[72] D. E. Gary and C. U. Keller. *Solar and Space Weather Radiophysics - Current Status and Future Developments*, volume 314. Dordrecht, Holland: Kluwer Academic Publishers, 2004.

[73] T. E. Gergely. Type-IV Bursts and Coronal Mass Ejections. *Solar Physics*, 104(1):175–178, March 1986.

[74] V. L Ginzburg. On solar radiation in the radio spectrum [in russian]. *Doklady Akademii Nauk, USSR*, 52:487, 1946.

[75] V. L. Ginzburg and V. V. Zhelezniakov. On the Possible Mechanisms of Sporadic Solar Radio Emission (Radiation in an Isotropic Plasma). *Soviet Astronomy*, 2:653, October 1958.

[76] A. A. Gnezdilov. Determination of Two-Dimensional Structure of the Noise Storm of May 20, 1966 from Data of Eclipse Observations at Four Stations. *Soviet Astronomy*, 14:59, August 1970.

[77] N. Gopalswamy. Coronal Mass Ejections and Type II Radio Bursts. *American Geophysical Union Geophysical Monograph Series*, 165:207, October 2006.

[78] N. Gopalswamy. Coronal Mass Ejections and Solar Radio Emissions, keywords = Solar radio emissions, Sun, coronal mass ejections, SOHO. In H. O. Rucker, W. S. Kurth, P. Louarn, and G. Fischer, editors, *Planetary, Solar and Heliospheric Radio Emissions (PRE VII)*, pages 325–342. Vienna, Austria: Austrian Academy of Sciences Press, January 2011.

[79] N. Gopalswamy and M. R. Kundu. Estimation of the Mass of a Coronal Mass Ejection from Radio Observations. *The Astrophysical Journal Letters*, 390:L37, May 1992.

[80] N. Gopalswamy, M. R. Kundu, Y. Hanaoka, S. Enome, J. R. Lemen, and M. Akioka. Yohkoh/SXT observations of a coronal mass ejection near the solar surface. *New Astronomy*, 1(3):207–213, November 1996.

[81] N. Gopalswamy and P. Mäkelä. Long-duration Low-frequency Type III Bursts and Solar Energetic Particle Events. *The Astrophysical Journal Letters*, 721(1):62–66, September 2010.

[82] N. Gopalswamy, N. Nitta, P. K. Manoharan, A. Raoult, and M. Pick. X-ray and radio manifestations of a solar eruptive event. *Astronomy & Astrophysics*, 347:684–695, July 1999.

[83] N. Gopalswamy, S. Yashiro, M. L. Kaiser, R. A. Howard, and J. L. Bougeret. Characteristics of coronal mass ejections associated with long-wavelength type II radio bursts. *Journal of Geophysical Research: Space Physics*, 106(A12):29219–29230, December 2001.

[84] W. Grotrian. Zur Frage der Deutung der Linien im Spektrum der Sonnenkorona. *Naturwissenschaften*, 27(13):214–214, March 1939.

[85] M. Guhathakurta, T. E. Holzer, and R. M. MacQueen. The Large-Scale Density Structure of the Solar Corona and the Heliospheric Current Sheet. *The Astrophysical Journal*, 458:817, February 1996.

[86] D. A. Guidice and J. P. Castelli. Spectral Distributions of Microwave Bursts. *Solar Physics*, 44(1):155–172, September 1975.

[87] D. A. Gurnett. The Earth as a radio source: Terrestrial kilometric radiation. *Journal of Geophysical Research: Space Physics*, 79(28):4227, October 1974.

[88] M. Hahn and D. W. Savin. Evidence for Wave Heating of the Quiet-Sun Corona. *The Astrophysical Journal*, 795(2):111, November 2014.

[89] I. G. Hannah, H. S. Hudson, G. J. Hurford, and R. P. Lin. Constraining the Hard X-ray Properties of the Quiet Sun with New RHESSI Observations. *The Astrophysical Journal*, 724(1):487–492, November 2010.

[90] I. G. Hannah, G. J. Hurford, H. S. Hudson, R. P. Lin, and K. van Bibber. First Limits on the 3-200 keV X-Ray Spectrum of the Quiet Sun Using RHESSI. *The Astrophysical Journal Letters*, 659(1):L77–L80, April 2007.

[91] T. Hirayama. Theoretical Model of Flares and Prominences. I: Evaporating Flare Model. *Solar Physics*, 34(2):323–338, February 1974.

[92] J. V. Hollweg. Alfvén waves in the solar atmosphere. *Solar Physics*, 56(2):305–333, February 1978.

[93] R. M. E. Illing and A. J. Hundhausen. Observation of a coronal transient from 1.2 to 6 solar radii. *Journal of Geophysical Research: Space Physics*, 90(A1):275–282, January 1985.

[94] S. Ishikawa and S. Krucker. Hot Plasma in a Quiescent Solar Active Region as Measured by RHESSI, XRT, and AIA. *The Astrophysical Journal*, 876(2):111, May 2019.

[95] S. R. Kane. Evidence for a Common Origin of the Electrons Responsible for the Impulsive X-Ray and Type III Radio Bursts. *Solar Physics*, 27(1):174–181, November 1972.

[96] J. A. Klimchuk. Cross-Sectional Properties of Coronal Loops. *Solar Physics*, 193:53–75, April 2000.

[97] J. A. Klimchuk. On Solving the Coronal Heating Problem. *Solar Physics*, 234(1):41–77, March 2006.

[98] J. A. Klimchuk. Key aspects of coronal heating. *Philosophical Transactions of the Royal Society of London Series A*, 373(2042):20140256–20140256, April 2015.

[99] J. A. Klimchuk, L. W. Acton, K. L. Harvey, H. S. Hudson, K. L. Kluge, D. G. Sime, K. T. Strong, and Ta. Watanabe. Coronal Eruptions Observed by YOHKOH. In Yutaka Uchida, Tetsuya Watanabe, Kazunari Shibata, and Hugh S. Hudson, editors, *X-ray solar physics from Yohkoh*, page 181. Tokyo, Japan: Universal Academy Press, January 1994.

[100] J. A. Klimchuk and Hinode Review Team. Achievements of Hinode in the first eleven years. *Publications of the Astronomical Society of Japan*, 71(5):47–50, 10 2019. R1.

[101] J. Kocz, L. J. Greenhill, B. R. Barsdell, D. Price, G. Bernardi, S. Bourke, M. A. Clark, J. Craig, M. Dexter, J. Dowell, T. Eftekhari, S. Ellingson, G. Hallinan, J. Hartman, A. Jameson, D. MacMahon, G. Taylor, F. Schinzel, and D. Werthimer. Digital Signal Processing Using Stream High Performance Computing: A 512-Input Broadband Correlator for Radio Astronomy. *Journal of Astronomical Instrumentation*, 4:1550003, June 2015.

[102] E. P. Kontar, X. Chen, N. Chrysaphi, N. L. S. Jeffrey, A. G. Emslie, V. Krupar, M. Maksimovic, M. Gordovskyy, and P. K. Browning. Anisotropic Radio-wave Scattering and the Interpretation of Solar Radio Emission Observations. *The Astrophysical Journal*, 884(2):122, October 2019.

[103] E. P. Kontar and H. A. S. Reid. Onsets and Spectra of Impulsive Solar Energetic Electron Events Observed Near the Earth. *The Astrophysical Journal Letters*, 695(2):140–144, April 2009.

[104] R. A. Kopp and G. W. Pneuman. Magnetic reconnection in the corona and the loop prominence phenomenon. *Solar Physics*, 50(1):85–98, October 1976.

[105] M. R. Kundu and R. G. Stone. Observations of solar radio bursts from meter to kilometer wavelengths. *Advances in Space Research*, 4(7):261–270, January 1984.

[106] J. E. Leake, L. K. S. Daldorff, and J. A. Klimchuk. The Onset of 3D Magnetic Reconnection and Heating in the Solar Corona. *The Astrophysical Journal*, 891(1):62, March 2020.

[107] Y. Leblanc, G. A. Dulk, A. Vourlidas, and J-L. Bougeret. Tracing shock waves from the corona to 1 AU: Type II radio emission and relationship with CMEs. *Journal of Geophysical Research: Space Physics*, 106(A11):25301–25312, November 2001.

[108] A. Lecacheux. The Nançay Decameter Array: A Useful Step Towards Giant, New Generation Radio Telescopes for Long Wavelength Radio Astronomy. *Washington DC American Geophysical Union Geophysical Monograph Series*, 119:321, January 2000.

[109] J. R. Lemen, A. M. Title, D. J. Akin, P. F. Boerner, C. Chou, J. F. Drake, D. W. Duncan, C. G. Edwards, F. M. Friedlaender, G. F. Heyman, N. E. Hurlburt, N. L. Katz, G. D. Kushner, M. Levay, R. W. Lindgren, D. P. Mathur, E. L. McFeaters, S. Mitchell, R. A. Rehse, C. J. Schrijver, L. A. Springer, R. A. Stern, T. D. Tarbell, J.-P. Wuelser, C. J. Wolfson, C. Yanari, J. A. Bookbinder, P. N. Cheimets, D. Caldwell, E. E. Deluca, R. Gates, L. Golub, S. Park, W. A. Podgorski, R. I. Bush, P. H. Scherrer, M. A. Gummin, P. Smith, G. Auker, P. Jerram, P. Pool, R. Soufli, D. L. Windt, S. Beardsley, M. Clapp, J. Lang, and N. Waltham. The Atmospheric Imaging Assembly (AIA) on the Solar Dynamics Observatory (SDO). *Solar Physics*, 275(1-2):17–40, January 2012.

[110] J. Lin and T. G. Forbes. Effects of reconnection on the coronal mass ejection process. *Journal of Geophysical Research: Space Physics*, 105(A2):2375–2392, Februray 2000.

[111] R. M. MacQueen, A. J. Hundhausen, and C. W. Conover. The propagation of coronal mass ejection transients. *Journal of Geophysical Research: Space Physics*, 91(A1):31–38, January 1986.

[112] D. Maia, M. Pick, A. Vourlidas, and R. Howard. Development of Coronal Mass Ejections: Radio Shock Signatures. *The Astrophysical Journal Letters*, 528(1):L49–L51, January 2000.

[113] D. J. F. Maia, R. Gama, C. Mercier, M. Pick, A. Kerdraon, and M. Karlický. The Radio-Coronal Mass Ejection Event on 2001 April 15. *The Astrophysical Journal*, 660(1):874–881, May 2007.

[114] C. H. Mandrini, D. Baker, P. Démoulin, G. D. Cristiani, L. van Driel-Gesztelyi, S. Vargas Domínguez, F. A. Nuevo, A. M. Vásquez, and M. Pick. Parallel Evolution of Quasi-separatrix Layers and Active Region Upflows. *The Astrophysical Journal*, 809(1):73, August 2015.

[115] C. H. Mandrini, P. Démoulin, and J. A. Klimchuk. Magnetic Field and Plasma Scaling Laws: Their Implications for Coronal Heating Models. *The Astrophysical Journal*, 530(2):999–1015, February 2000.

[116] G. Mann, F. Breitling, C. Vocks, H. Aurass, M. Steinmetz, K. G. Strassmeier, M. M. Bisi, R. A. Fallows, P. Gallagher, A. Kerdraon, A. Mackinnon, J. Magdalenic, H. Rucker, J. Anderson, A. Asgekar, I. M. Avruch, M. E. Bell, M. J. Bentum, G. Bernardi, P. Best, L. Bîrzan, A. Bonafede, J. W. Broderick, M. Brüggen, H. R. Butcher, B. Ciardi, A. Corstanje, F. de Gasperin, E. de Geus, A. Deller, S. Duscha, J. Eislöffel, D. Engels, H. Falcke, R. Fender, C. Ferrari, W. Frieswijk, M. A. Garrett, J. Grießmeier, A. W. Gunst, M. van Haarlem, T. E. Hassall, G. Heald, J. W. T. Hessels, M. Hoeft, J. Hörandel, A. Horneffer, E. Juette, A. Karastergiou, W. F. A. Klijn, V. I. Kondratiev, M. Kramer, M. Kuniyoshi, G. Kuper, P. Maat, S. Markoff, R. McFadden, D. McKay-Bukowski, J. P. McKean, D. D. Mulcahy, H. Munk, A. Nelles, M. J. Norden, E. Orru, H. Paas, M. Pandey-Pommier, V. N. Pandey, R. Pizzo, A. G. Polatidis, D. Rafferty, W. Reich, H. Röttgering, A. M. M. Scaife, D. J. Schwarz, M. Serylak, J. Sluman, O. Smirnov, B. W. Stappers, M. Tagger, Y. Tang, C. Tasse, S. ter Veen, S. Thoudam, M. C. Toribio, R. Vermeulen, R. J. van Weeren, M. W. Wise, O. Wucknitz, S. Yatawatta, P. Zarka, and J. A. Zensus. Tracking of an electron beam through the solar corona with LOFAR. *Astronomy & Astrophysics*, 611:A57, March 2018.

[117] P. C. H. Martens. Scaling Laws and Temperature Profiles for Solar and Stellar Coronal Loops with Non-uniform Heating. *The Astrophysical Journal*, 714(2):1290–1304, May 2010.

[118] P. I. McCauley. Radio Burst and Circular Polarization Studies of the Solar Corona at Low Frequencies. *arXiv e-prints*, page arXiv:1912.01747, Decemeber 2019.

[119] P. I. McCauley, I. H. Cairns, S. M. White, S. Mondal, E. Lenc, J. Morgan, and D. Oberoi. The Low-Frequency Solar Corona in Circular Polarization. *Solar Physics*, 294(8):106, August 2019.

[120] D. J. McLean. Radioheliograph observations of harmonic type III solar bursts. *Australian Journal of Physics*, 24:201, February 1971.

[121] D. J. McLean and N. R. Labrum. *Solar radiophysics : studies of emission from the sun at metre wavelengths*. Cambridge, New York : Cambridge University Press, 1985.

[122] J. P. McMullin, B. Waters, D. Schiebel, W. Young, and K. Golap. CASA Architecture and Applications. In R. A. Shaw, F. Hill, and D. J. Bell, editors, *Astronomical Data Analysis Software and Systems XVI*, volume 376 of *Astronomical Society of the Pacific Conference Series*, page 127, October 2007.

[123] D. B. Melrose. The Emission Mechanisms for Solar Radio Bursts. *Space Science Reviews*, 26(1):3–38, May 1980.

[124] D. B. Melrose. Wave Localization in Solar Type-Iii Events. *Solar Physics*, 119(2):385–398, September 1989.

[125] D. B. Melrose. Coherent emission. In N. Gopalswamy and D. F. Webb, editors, *Universal Heliophysical Processes*, volume 257, pages 305–315, March 2009.

[126] D. B. Melrose. Coherent emission mechanisms in astrophysical plasmas. *Reviews of Modern Plasma Physics*, 1(1):5, December 2017.

[127] D. A. Mitchell, L. J. Greenhill, R. B. Wayth, R. J. Sault, C. J. Lonsdale, R. J. Cappallo, M. F. Morales, and S. M. Ord. Real-Time Calibration of the Murchison Widefield Array. *IEEE Journal of Selected Topics in Signal Processing*, 2(5):707–717, November 2008.

[128] Y. Mok, Z. Mikić, R. Lionello, C. Downs, and J. A. Linker. A Three-dimensional Model of Active Region 7986: Comparison of Simulations with Observations. *The Astrophysical Journal*, 817(1):15, January 2016.

[129] S. Mondal, D. Oberoi, and A. Vourlidas. Estimation of the Physical Parameters of a CME at High Coronal Heights Using Low-frequency Radio Observations. *The Astrophysical Journal*, 893(1):28, April 2020.

[130] H. Morgan, S. R. Habbal, and R. Woo. The Depiction of Coronal Structure in White-Light Images. *Solar Physics*, 236(2):263–272, July 2006.

[131] D. E. Morosan, E. P. Carley, L. A. Hayes, S. A. Murray, P. Zucca, R. A. Fallows, J. McCauley, E. K. J. Kilpua, G. Mann, C. Vocks, and P. T. Gallagher. Multiple regions of shock-accelerated particles during a solar coronal mass ejection. *Nature Astronomy*, 3:452–461, February 2019.

[132] D. E. Morosan, E. K. J. Kilpua, E. P. Carley, and C. Monstein. Variable emission mechanism of a Type IV radio burst. *Astronomy & Astrophysics*, 623:A63, March 2019.

[133] S. M. Mulay, R. Sharma, G. Valori, A. M. Vásquez, G. Del Zanna, H. Mason, and D. Oberoi. Study of the spatial association between an active region jet and a nonthermal type III radio burst. *Astronomy & Astrophysics*, 632:A108, December 2019.

[134] G. J. Nelson and D. B. Melrose. *Type II bursts.*, pages 333–359. Cambridge and New York: Cambridge University Press, 1985.

[135] A. Nindos. Incoherent Solar Radio Emission. *Frontiers in Astronomy and Space Sciences*, 7:57, November 2020.

[136] A. Nindos. Incoherent Solar Radio Emission. *Frontiers in Astronomy and Space Sciences*, 7:57, 2020.

[137] A. R. Offringa, B. McKinley, N. Hurley-Walker, F. H. Briggs, R. B. Wayth, D. L. Kaplan, M. E. Bell, L. Feng, A. R. Neben, J. D. Hughes, J. Rhee, T. Murphy, N. D. R. Bhat, G. Bernardi, J. D. Bowman, R. J. Cappallo, B. E. Corey, A. A. Deshpande, D. Emrich, A. Ewall-Wice, B. M. Gaensler, R. Goeke, L. J. Greenhill, B. J. Hazelton, L. Hindson, M. Johnston-Hollitt, D. C. Jacobs, J. C. Kasper, E. Kratzenberg, E. Lenc, C. J. Lonsdale, M. J. Lynch, S. R. McWhirter, D. A. Mitchell, M. F. Morales, E. Morgan, N. Kudryavtseva, D. Oberoi, S. M. Ord, B. Pindor, P. Procopio, T. Prabu, J. Riding, D. A. Roshi, N. Udaya Shankar, K. S. Srivani, R. Subrahmanyan, S. J. Tingay, M. Waterson, R. L. Webster, A. R. Whitney, A. Williams, and C. L. Williams. WSCLEAN: an implementation of a fast, generic wide-field imager for radio astronomy. *Monthly Notices of the Royal Astronomical Society*, 444(1):606–619, October 2014.

[138] D. E. Osterbrock. The Heating of the Solar Chromosphere, Plages, and Corona by Magnetohydrodynamic Waves. *The Astrophysical Journal*, 134:347, September 1961.

[139] E. N. Parker. Dynamics of the Interplanetary Gas and Magnetic Fields. *The Astrophysical Journal*, 128:664, November 1958.

[140] E. N. Parker. Magnetic neutral sheets in evolving fields. I - General theory. *The Astrophysical Journal*, 264:635–647, January 1983.

[141] E. N. Parker. Nanoflares and the Solar X-Ray Corona. *The Astrophysical Journal*, 330:474, July 1988.

[142] R. Payne-Scott. Bursts of Solar Radiation at Metre Wavelengths. *Australian Journal of Scientific Research A Physical Sciences*, 2:214, June 1949.

[143] R. A. Perley, C. J. Chandler, B. J. Butler, and J. M. Wrobel. The Expanded Very Large Array: A New Telescope for New Science. *The Astrophysical Journal Letters*, 739(1):L1, September 2011.

[144] H. Peter and B. N. Dwivedi. Discovery of the Sun's million-degree hot corona. *Frontiers in Astronomy and Space Sciences*, 1:2, July 2014.

[145] T. Priest, E.and Forbes. *Magnetic Reconnection.* Cambridge, UK: Cambridge University Press, 2000.

[146] M. Pulupa, S. D. Bale, S. T. Badman, J. W. Bonnell, A. W. Case, T. D. de Wit, K. Goetz, P. R. Harvey, A. M. Hegedus, J. C. Kasper, K. E. Korreck, V. Krasnoselskikh, D. Larson, A. Lecacheux, R. Livi, R. J. MacDowall, M. Maksimovic, D. M. Malaspina, J. C. Martínez Oliveros, N. Meyer-Vernet, M. Moncuquet, M. Stevens, and P. Whittlesey. Statistics and Polarization of Type III Radio Bursts Observed in the Inner Heliosphere. *The Astrophysical Journal Supplement Series*, 246(2):49, February 2020.

[147] M. Pulupa, S. D. Bale, J. W. Bonnell, T. A. Bowen, N. Carruth, K. Goetz, D. Gordon, P. R. Harvey, M. Maksimovic, J. C. Martínez-Oliveros, M. Moncuquet, P. Saint-Hilaire, D. Seitz, and D. Sundkvist. The Solar Probe Plus Radio Frequency Spectrometer: Measurement requirements, analog design, and digital signal processing. *Journal of Geophysical Research (Space Physics)*, 122(3):2836–2854, March 2017.

[148] M. M. Rahman, I.H. Cairns, and P. I. McCauley. Spectropolarimetric Imaging of Metric Type III Solar Radio Bursts. *Solar Physics*, 295(3):51, March 2020.

[149] H. Ratcliffe, E. P. Kontar, and H. A. S. Reid. Large-scale simulations of solar type III radio bursts: flux density, drift rate, duration, and bandwidth. *Astronomy & Astrophysics*, 572:A111, December 2014.

[150] V. A. Razin. On the spectrum of nonthermal cosmic radio emission. *Izvestiya Vysshikh Uchebnykh Zavedenii Radiofizika*, 3:584, 1960.

[151] H. A. S. Reid. A review of recent type III imaging spectroscopy. *Frontiers in Astronomy and Space Sciences*, 7:56, September 2020.

[152] H. A. S. Reid and E. P. Kontar. Stopping frequency of type III solar radio bursts in expanding magnetic flux tubes. *Astronomy & Astrophysics*, 577:A124, May 2015.

[153] H. A. S. Reid and E. P. Kontar. Spatial Expansion and Speeds of Type III Electron Beam Sources in the Solar Corona. *The Astrophysical Journal*, 867(2):158, November 2018.

[154] H. A. S. Reid and H. Ratcliffe. A review of solar type III radio bursts. *Research in Astronomy and Astrophysics*, 14(7):773–804, July 2014.

[155] M. J. Reiner, M. Karlický, K. Jiřička, H. Aurass, G. Mann, and M. L. Kaiser. On the Solar Origin of Complex Type III-like Radio Bursts Observed at and below 1 MHz. *The Astrophysical Journal*, 530(2):1049–1060, February 2000.

[156] P. A. Robinson and I. H. Cairns. Theory of Type III And Type II Solar Radio Emissions. *Washington DC American Geophysical Union Geophysical Monograph Series*, 119:37, January 2000.

[157] R. D. Robinson. A study of type V solar radio bursts. I: Observations. *Solar Physics*, 55(2):459–472, December 1977.

[158] R. D. Robinson. A study of type V solar radio bursts. II. A theoretical model. *Solar Physics*, 56(2):405–416, February 1978.

[159] A. S. Rodger and N. Labrosse. Spectral gradient of the thermal millimetre continuum as a diagnostic for optical thickness in the solar atmosphere. *Astronomy & Astrophysics*, 617:L6, September 2018.

[160] P. Saint-Hilaire, G. J. Hurford, G. Keating, G. C. Bower, and C. Gutierrez-Kraybill. Allen Telescope Array Multi-frequency Observations of the Sun. *Solar Physics*, 277(2):431–445, April 2012.

[161] K. Sakurai. Solar flare emissions and geophysical disturbances. *Indian Journal of Radio and Space Physics*, 3:289–312, September 1974.

[162] S. J. Schonfeld and J. A. Klimchuk. Transition Region Contribution to AIA Observations in the Context of Coronal Heating. *The Astrophysical Journal*, 905(2):115, December 2020.

[163] S. J. Schonfeld, S. M. White, C. J. Henney, C. N. Arge, and R. T. J. McAteer. Coronal Sources of the Solar $F_{10.7}$ Radio Flux. *The Astrophysical Journal*, 808(1):29, July 2015.

[164] M. Schwarzschild. On Noise Arising from the Solar Granulation. *The Astrophysical Journal*, 107:1, January 1948.

[165] R. Sharma, D. Oberoi, and M. Arjunwadkar. Quantifying Weak Nonthermal Solar Radio Emission at Low Radio Frequencies. *The Astrophysical Journal*, 852(2):69, January 2018.

[166] I. N. Sharykin, E. P. Kontar, and A. A. Kuznetsov. LOFAR Observations of Fine Spectral Structure Dynamics in Type IIIb Radio Bursts. *Solar Physics*, 293(8):115, August 2018.

[167] G. L. Siscoe, Jr. Davis, L., Jr. Coleman, P. J., E. J. Smith, and D. E. Jones. Power spectra and discontinuities of the interplanetary magnetic field: Mariner 4. *Journal of Geophysical Research: Space Physics*, 73(1):61–82, January 1968.

[168] C. Slottje. *Atlas of fine structures of dynamic spectra of solar type IV-dm and some type II radio bursts*. PhD thesis, Rijksuniversiteit Utrecht (Netherlands), April 1982.

[169] J. L. Steinberg, S. Hoang, A. Lecacheux, M. G. Aubier, and G. A. Dulk. Type III radio bursts in the interplanetary medium - The role of propagation. *Astronomy & Astrophysics*, 140(1):39–48, November 1984.

[170] P. A. Sturrock. Model of the High-Energy Phase of Solar Flares. *Nature*, 211(5050):695–697, August 1966.

[171] J. F. Tang, D. J. Wu, and C. M. Tan. Electron Cyclotron Maser Emission in Coronal Arches and Solar Radio Type V Bursts. *The Astrophysical Journal*, 779(1):83, December 2013.

[172] K. F. Tapping, H. T. Cameron, and A. G. Willis. S-Component Sources at 21 cm Wavelength in the Rising Phase of Cycle 23. *Solar Physics*, 215(2):357–383, August 2003.

[173] G. Thejappa and R. J. MacDowall. Effects of Scattering on Radio Emission from the Quiet Sun at Low Frequencies. *The Astrophysical Journal*, 676(2):1338–1345, April 2008.

[174] A. F. R. Thernisien, R. A. Howard, and A. Vourlidas. Modeling of Flux Rope Coronal Mass Ejections. *The Astrophysical Journal*, 652(1):763–773, November 2006.

[175] S. J. Tingay, R. Goeke, J. D. Bowman, D. Emrich, S. M. Ord, D. A. Mitchell, M. F. Morales, T. Booler, B. Crosse, R. B. Wayth, C. J. Lonsdale, S. Tremblay, D. Pallot, T. Colegate, A. Wicenec, N. Kudryavtseva, W. Arcus, D. Barnes, G. Bernardi, F. Briggs, S. Burns, J. D. Bunton, R. J. Cappallo, B. E. Corey, A. Deshpande, L. Desouza, B. M. Gaensler, L. J. Greenhill, P. J. Hall, B. J. Hazelton, D. Herne, J. N. Hewitt, M. Johnston-Hollitt, D. L. Kaplan, J. C. Kasper, B. B. Kincaid, R. Koenig, E. Kratzenberg, M. J. Lynch, B. Mckinley, S. R. Mcwhirter, E. Morgan, D. Oberoi, J. Pathikulangara, T. Prabu, R. A. Remillard, A. E. E. Rogers, A. Roshi, J. E. Salah, R. J. Sault, N. Udaya-Shankar, F. Schlagenhaufer, K. S. Srivani, J. Stevens, R. Subrahmanyan, M. Waterson, R. L. Webster, A. R. Whitney, A. Williams, C. L. Williams, and J. S. B. Wyithe. The Murchison Widefield Array: The Square Kilometre Array Precursor at Low Radio Frequencies. *Publications of the Astronomical Society of Australia*, 30:e007, January 2013.

[176] R. Tousey. First Results from Skylab. In *Bulletin of the American Astronomical Society*, volume 5, page 419. Tucson, AZ: Bulletin of the American Astronomical Society, September 1973.

[177] D. Tripathi, J. A. Klimchuk, and H. E. Mason. Emission Measure Distribution and Heating of Two Active Region Cores. *The Astrophysical Journal*, 740(2):111, October 2011.

[178] S. D. Tun, D. E. Gary, and M. K. Georgoulis. Three-dimensional Structure of a Solar Active Region from Spatially and Spectrally Resolved Microwave Observations. *The Astrophysical Journal*, 728(1):1, February 2011.

[179] S. D. Tun and A. Vourlidas. Derivation of the Magnetic Field in a Coronal Mass Ejection Core via Multi-frequency Radio Imaging. *The Astrophysical Journal*, 766(2):130, April 2013.

[180] Y. Uchida. On the Exciters of Type II and Type III Solar Radio Bursts. , 12:376, January 1960.

[181] M. P. van Haarlem, M. W. Wise, A. W. Gunst, G. Heald, J. P. McKean, J. W. T. Hessels, A. G. de Bruyn, R. Nijboer, J. Swinbank, R. Fallows, M. Brentjens, A. Nelles, R. Beck, H. Falcke, R. Fender, J. Hörandel, L. V. E. Koopmans, G. Mann, G. Miley, H. Röttgering, B. W. Stappers, R. A. M. J. Wijers, S. Zaroubi, M. van den Akker, A. Alexov, J. Anderson, K. Anderson, A. van Ardenne, M. Arts, A. Asgekar, I. M. Avruch, F. Batejat, L. Bähren, M. E. Bell, M. R. Bell, I. van Bemmel, P. Bennema, M. J. Bentum, G. Bernardi, P. Best, L. Bîrzan, A. Bonafede, A. J. Boonstra, R. Braun, J. Bregman, F. Breitling, R. H. van de Brink, J. Broderick, P. C. Broekema, W. N. Brouw, M. Brüggen, H. R. Butcher, W. van Cappellen, B. Ciardi, T. Coenen, J. Conway, A. Coolen, A. Corstanje, S. Damstra, O. Davies, A. T. Deller, R. J. Dettmar, G. van Diepen, K. Dijkstra, P. Donker, A. Doorduin, J. Dromer, M. Drost, A. van Duin, J. Eislöffel, J. van Enst, C. Ferrari, W. Frieswijk, H. Gankema, M. A. Garrett, F. de Gasperin, M. Gerbers, E. de Geus, J. M. Grießmeier, T. Grit, P. Gruppen, J. P. Hamaker, T. Hassall, M. Hoeft, H. A. Holties, A. Horneffer, A. van der Horst, A. van Houwelingen, A. Huijgen, M. Iacobelli, H. Intema, N. Jackson, V. Jelic, A. de Jong, E. Juette, D. Kant, A. Karastergiou, A. Koers, H. Kollen, V. I. Kondratiev, E. Kooistra, Y. Koopman, A. Koster, M. Kuniyoshi, M. Kramer, G. Kuper, P. Lambropoulos, C. Law, J. van Leeuwen, J. Lemaitre, M. Loose, P. Maat, G. Macario, S. Markoff, J. Masters, R. A. McFadden, D. McKay-Bukowski, H. Meijering, H. Meulman, M. Mevius, E. Middelberg, R. Millenaar, J. C. A. Miller-Jones, R. N. Mohan, J. D. Mol, J. Morawietz, R. Morganti, D. D. Mulcahy, E. Mulder, H. Munk, L. Nieuwenhuis, R. van Nieuwpoort, J. E. Noordam, M. Norden, A. Noutsos, A. R. Offringa, H. Olofsson, A. Omar, E. Orrú, R. Overeem, H. Paas, M. Pandey-Pommier, V. N. Pandey, R. Pizzo, A. Polatidis, D. Rafferty, S. Rawlings, W. Reich, J. P. de Reijer, J. Reitsma, G. A. Renting, P. Riemers, E. Rol, J. W. Romein, J. Roosjen, M. Ruiter, A. Scaife, K. van der Schaaf, B. Scheers, P. Schellart, A. Schoenmakers, G. Schoonderbeek, M. Serylak, A. Shulevski, J. Sluman, O. Smirnov, C. Sobey, H. Spreeuw, M. Steinmetz, C. G. M. Sterks, H. J. Stiepel, K. Stuurwold, M. Tagger, Y. Tang, C. Tasse, I. Thomas, S. Thoudam, M. C. Toribio, B. van der Tol, O. Usov, M. van Veelen, A. J. van der Veen, S. ter Veen, J. P. W. Verbiest, R. Vermeulen, N. Vermaas, C. Vocks, C. Vogt, M. de Vos, E. van der Wal, R. van Weeren, H. Weggemans, P. Weltevrede, S. White, S. J. Wijnholds, T. Wilhelmsson, O. Wucknitz, S. Yatawatta, P. Zarka, A. Zensus, and J. van Zwieten. LOFAR: The LOw-Frequency ARray. *Astronomy & Astrophysics*, 556:A2, August 2013.

[182] V. Vasanth, Y. Chen, M. Lv, H. Ning, C. Li, S. Feng, Z. Wu, and G.i Du. Source Imaging of a Moving Type IV Solar Radio Burst and Its Role in Tracking Coronal Mass Ejection from the Inner to the Outer Corona. *The Astrophysical Journal*, 870(1):30, January 2019.

[183] N. M. Viall and J. A. Klimchuk. Evidence for Widespread Cooling in an Active Region Observed with the SDO Atmospheric Imaging Assembly. *The Astrophysical Journal*, 753(1):35, July 2012.

[184] N. M. Viall and J. A. Klimchuk. Modeling the Line-of-sight Integrated Emission in the Corona: Implications for Coronal Heating. *The Astrophysical Journal*, 771(2):115, July 2013.

[185] N. M. Viall and J. A. Klimchuk. A Survey of Nanoflare Properties in Active Regions Observed with the Solar Dynamics Observatory. *The Astrophysical Journal*, 842(2):108, June 2017.

[186] J. T. Vievering, Li. Glesener, P. S. Athiray, J. C. Buitrago-Casas, D. Musset, S.and Ryan, S. Ishikawa, J. Duncan, S. Christe, and S. Krucker. FOXSI-2 Solar Microflares II: Hard X-ray Imaging Spectroscopy and Flare Energetics. *arXiv e-prints*, page arXiv:2011.04753, November 2020.

[187] E. N. Vinyaikin. The integrated radio spectrum of Virgo A. *Astronomy Reports*, 60(8):744–752, August 2016.

[188] B. Vršnak, H. Aurass, J. Magdalenić, and N. Gopalswamy. Band-splitting of coronal and interplanetary type II bursts. I. Basic properties. *Astronomy & Astrophysics*, 377:321–329, October 2001.

[189] Y. Wang and J. Zhang. A Comparative Study between Eruptive X-Class Flares Associated with Coronal Mass Ejections and Confined X-Class Flares. *The Astrophysical Journal*, 665(2):1428–1438, August 2007.

[190] A. A. Weiss. The Type IV Solar Radio Burst at Metre Wavelengths. *Australian Journal of Physics*, 16:526, December 1963.

[191] Late A. A. Weiss and R. T. Stewart. Solar radio bursts of spectral type V. *Australian Journal of Physics*, 18:143, April 1965.

[192] D. G. Wentzel. Polarization of Fundamental Type-Iii Radio Bursts. *Solar Physics*, 90(1):139–159, January 1984.

[193] D. G. Wentzel, P. Zlobec, and M. Messerotti. A test for large-angle radio scattering in the solar corona. *Astronomy & Astrophysics*, 159(1-2):40–48, Aprill 1986.

[194] S. M. White. Solar radio bursts and space weather. *Asian J. Phys*, 16:189—207, 2007.

[195] S. M. White, A. O. Benz, S. Christe, F. Fárník, M. R. Kundu, G. Mann, Z. Ning, J. P. Raulin, A. V. R. Silva-Válio, P. Saint-Hilaire, N. Vilmer, and A. Warmuth. The Relationship Between Solar Radio and Hard X-ray Emission. *Space Science Reviews*, 159(1-4):225–261, September 2011.

[196] S. M. White, R. J. Thomas, J. W. Brosius, and M. R. Kundu. The Absolute Abundance of Iron in the Solar Corona. *The Astrophysical Journal Letters*, 534(2):L203–L206, May 2000.

[197] J. P. Wild. De-convolution of barely resolved radio sources mapped with aerial beams of elliptical cross section. *Australian Journal of Physics*, 23:113, February 1970.

[198] J. P. Wild and L. L. McCready. Observations of the Spectrum of High-Intensity Solar Radiation at Metre Wavelengths. I. The Apparatus and Spectral Types of Solar Burst Observed. *Australian Journal of Scientific Research A Physical Sciences*, 3:387, September 1950.

[199] J. P. Wild, K. V. Sheridan, and A. A. Neylan. An Investigation of the Speed of the Solar Disturbances responsible for Type III Radio Bursts. *Australian Journal of Physics*, 12:369, December 1959.

[200] J. P. Wild, K. V. Sheridan, and G. H. Trent. The transverse motions of the sources of solar radio bursts. In Ronald N. Bracewell, editor, *URSI Symp. 1: Paris Symposium on Radio Astronomy*, volume 9, page 176. Stanford, CA: Stanford University Press, January 1959.

[201] A. R. Winebarger, J. T. Schmelz, H. P. Warren, S. H. Saar, and V. L. Kashyap. Using a Differential Emission Measure and Density Measurements in an Active Region Core to Test a Steady Heating Model. *The Astrophysical Journal*, 740(1):2, October 2011.

[202] R. M. Winglee and G. A. Dulk. The Electron-Cyclotron Maser Instability as the Source of Solar Type V Continuum. *The Astrophysical Journal*, 310:432, November 1986.

[203] G. L. Withbroe and R. W. Noyes. Mass and energy flow in the solar chromosphere and corona. *Annual Review of Astronomy and Astrophysics*, 15:363–387, January 1977.

[204] C. S. Wu and L. C. Lee. A theory of the terrestrial kilometric radiation. *The Astrophysical Journal*, 230:621–626, Jschwarune 1979.

[205] S. Yashiro and N. Gopalswamy. Statistical relationship between solar flares and coronal mass ejections. In N. Gopalswamy and D. F. Webb, editors, *Universal Heliophysical Processes*, volume 257, pages 233–243. Universal Heliophysical Processes, Proceedings of the International Astronomical Union, IAU Symposium, March 2009.

[206] S. Yashiro, N. Gopalswamy, G. Michalek, O. C. St. Cyr, S. P. Plunkett, N. B. Rich, and R. A. Howard. A catalog of white light coronal mass ejections observed by the SOHO spacecraft. *Journal of Geophysical Research (Space Physics)*, 109(A7):A07105, July 2004.

[207] S. Yu, B. Chen, T. Bastian, and D. E. Gary. Imaging Spectroscopic Observations of Type I Noise Storms with Ultrahigh Temporal and Spectral Resolution. In *AGU Fall Meeting Abstracts*, volume 2019, pages SH23C–3336, December 2019.

[208] V. V. Zheleznyakov and V. V. Zaitsev. Contribution to the Theory of Type III Solar Radio Bursts. I. *Soviet Astronomy*, 14:47, August 1970.

[209] V. V. Zheleznyakov and V. V. Zaitsev. The Theory of Type III Solar Radio Bursts. II. *Soviet Astronomy*, 14:250, October 1970.

[210] H. Zirin, G. J. Hurford, and K. A. Marsh. The small-scale sources of quiet-Sun centimeter-wave radio emission. *The Astrophysical Journal*, 224:1043–1047, September 1978.

[211] P. Zucca, D. E. Morosan, A. P. Rouillard, R. Fallows, P. T. Gallagher, J. Magdalenic, K. L. Klein, G. Mann, C. Vocks, E. P. Carley, M. M. Bisi, E. P. Kontar, H. Rothkaehl, B. Dabrowski, A. Krankowski, J. Anderson, A. Asgekar, M. E. Bell, M. J. Bentum, P. Best, R. Blaauw, F. Breitling, J. W. Broderick, W. N. Brouw, M. Brüggen, H. R. Butcher, B. Ciardi, E. de Geus, A. Deller, S. Duscha, J. Eislöffel, M. A. Garrett, J. M. Grießmeier, A. W. Gunst, G. Heald, M. Hoeft, J. Hörandel, M. Iacobelli, E. Juette, A. Karastergiou, J. van Leeuwen, D. McKay-Bukowski, H. Mulder, H. Munk, A. Nelles, E. Orru, H. Paas, V. N. Pandey, R. Pekal, R. Pizzo, A. G. Polatidis, W. Reich, A. Rowlinson, D. J. Schwarz, A. Shulevski, J. Sluman, O. Smirnov, C. Sobey, M. Soida, S. Thoudam, M. C. Toribio, R. Vermeulen, R. J. van Weeren, O. Wucknitz, and P. Zarka. Shock location and CME 3D reconstruction of a solar type II radio burst with LOFAR. *Astronomy & Astrophysics*, 615:A89, July 2018.